Flushed Away: How low and high magnitude turbidity currents affect the bathymetry, morphology and, sedimentation in the Nass Delta submarine channel

By

Felix Parkinson

B.Sc., University of Victoria, 2022

A Thesis Submitted in Partial Fulfillment of the

Requirements for the Degree of

MASTER OF SCIENCE

in the Department of Geography

We acknowledge and respect the Lək̓ʷəŋən (Songhees and Esquimalt) Peoples on whose territory the university stands, and the Lək̓ʷəŋən and W̱SÁNEĆ Peoples whose historical relationships with the land continue to this day.

Flushed Away: How low and high magnitude turbidity currents affect

the bathymetry, morphology and, sedimentation in the Nass Channel

By

Felix Parkinson

B.Sc., University of Victoria, 2022

Supervisory Committee

Dr. Eva Kwoll, Co-Supervisor

Department of Geography

Cooper Stacey, Outside Member

Geological Survey of Canada, Natural Resources Canada

Dr. Gwyn Lintern, Outside Member

Geological Survey of Canada, Natural Resources Canada

Abstract

Turbidity currents, a type of sediment density flow, are one of the largest mechanisms of sediment transport in the ocean. They often incise submarine channels that can confine flows and allow them to runout long distances. However, these flow events are poorly understood as they are difficult to monitor directly, and therefore questions remain about how different magnitudes of flow move sediment while interacting with seafloor morphology. The aim of this study was to address some of these knowledge gaps by investigating sediment change in the Nass Delta submarine channel system, a region that had not previously been studied. Here, repeat bathymetric surveys from 2020, 2021, and 2023 were used to calculate bathymetric change to quantify erosion and deposition in the submarine channel system caused by turbidity currents. The results from the first bathymetric change interval (2020-2021) showed little net-change and instead sediment was 'shuffled' down system by turbidity currents. This was expressed as predominantly deposition at the head of the channel, an approximate balance of erosion and deposition throughout most of the length of the channel and minor deposition on the lobe. During the second interval (2021-2023), the channel was dominated by erosion, similar to 'flushing' flows observed in other channel systems, and the lobe complexes showed net deposition that was an order of magnitude higher than the previous interval. This was interpreted to represent three magnitudes of flows that were either dissipative with a short runout distance, in an auto-suspension state with balanced erosion and deposition, or in an ignition state. These flows resulted in substantial changes to in-channel morphology including aggradation up to 7 m/year and migration up to 70 m/year of crescentic bedforms, up-channel knickpoint migration up to 371 m/year, and the widening of channel bends by up to 45 m/year. Knickpoints were shown to influence the highest rates of erosion in both bathymetric survey intervals. However, only during the erosive, or 'flushing', interval were

knickpoints created or removed. The 'flushing' interval also caused a channel avulsion which reactivated a distributary channel that had been previously blocked. Here, the term 'thresholding flows' is proposed to describe turbidity currents that change the channel equilibrium state. Although there were no direct measurements of turbidity currents, observations of river discharge, tidal predictions and mass wasting in the canyon indicate that the most likely triggers were either convective settling and remobilization of sediment on the delta or slope failures at the delta lip or canyon. Two facies of turbidite deposits were identified in sediment cores: Facies 1 sand beds, which were interpreted as deposits from higher magnitude flows with the T_a, T_b, T_c, and T_d Bouma intervals and Facies 2 sand laminations, which were interpreted as deposits from smaller magnitude flows with T_d and T_e Bouma intervals. These deposits were dated by creating an age-depth model using excess ^{210}Pb activity, ^{137}Cs activity and ^{14}C ages. This gave a return interval of 25 years for Facies 1 and 10 years for Facies 2 in the mid-channel reaches and 85 years for Facies 1 and 15 to 40 years for Facies 2 in the distal basin meaning that high- and low-density turbidity currents travel up to 22 km from the Nass Delta. These results show that the Nass Delta submarine channel system experiences frequent turbidity current activity that is comparable to other delta submarine channel systems such as the Squamish Delta and Bute Inlet systems, both over short (~1 year) and long (100s years) timescales, and therefore presents both an excellent study site for investigating turbidity current dynamics and poses a considerable hazard to seafloor infrastructure.

Table of Contents

Supervisory Committee ii

Abstract iii

Table of Contents v

Table of Figures ix

Table of Tables xv

Acknowledgements xvii

Chapter 1: Introduction 1

Motivation 1

Objectives 4

Background 5

Turbidity current Stratigraphy 5

Turbidity current Induced Surficial Morphology 7

Turbidity Current Magnitudes and Flow Characteristics 11

Initiation Mechanisms 12

Turbidity current Monitoring in British Columbia 13

Chapter 2: From low magnitude flows to thresholding flush events: Insights from turbidity flow sedimentation in the Nass Delta submarine channel system 15

Introduction 15

Aims 19

Study Site 19
Methods 22
Bathymetric Data Processing 22
Bathymetric Change 22
Volumetric Difference Mapping 23
Criteria for Seabed Feature Mapping 24
Morphological Analysis 25
Sediment Cores 26
Nass River Hydrometric Data and Sediment Rating Curve and Nass Bay Tidal Predictions 32
Results 33
Submarine Channel System Morphology 33
Difference Mapping and Volumetric Change 41
Sedimentary Lithofacies 56
Dating and Age Control 62
Turbidite Bed Return Intervals 65
Sediment Rating Curve 66
Discussion 67
Magnitudes of channel mobility 67
In Channel Mobility 68
Bedform Fields 72

Lobe building flows 73

Channel Reactivation 74

Flushing Flows as Thresholding Events 75

Sources of sediment and turbidity current triggers 76

Frequency of Turbidity Current Magnitudes 80

Geohazard Implications 82

Conclusion 84

Chapter 3: Conclusion 86

Objective 1: Determine how geomorphologically active the seabed is between bathymetry survey intervals and analyse specific seabed morphologies and subbottom structure to infer turbidity current characteristics. 86

Objective 2: Evaluate potential initiation mechanisms for turbidity currents on the Nass Delta. 88

Objective 3 & 4: Identify and describe turbidity current deposits in the stratigraphic record to establish distinct facies groupings. Develop a sedimentation rate model to develop to date turbidite deposits and determine reoccurrence rates. 88

Objective 5: Characterize the extent of the seafloor geohazard potential from turbidity currents at the Nass Delta 89

What makes the Nass Delta Submarine Channel System Unique 90

Future Studies 91

References 93

Appendices 103

Appendix A 103

Bathymetric Change Thresholding 103

Bathymetric Change Volumetric Budget segregation 106

Appendix B 106

^{210}Pb, ^{226}Ra and ^{137}Cs Results 106

^{14}C Samples and Unmodeled Dates 122

Appendix C 123

Turbidite Density Estimation 123

Appendix D 123

Limitations of bathymetric change detection 123

Table of Figures

Figure 1: The Nass Delta is located in Nass Bay at the mouth of the Nass River near the town of Gingolx with a submarine channel that extends into Portland Inlet. 21

Figure 2: Location of cores collected and logged for sedimentological analysis and radiometric dating. Red triangles denote piston cores, and the orange circle a gravity core. 29

Figure 3: I. Overview map of the submarine channel system with blue polygons denoting the extent of bedform fields, the brown polygon the extent of the lobes and the grey dashed line the extent of the canyon that was not surveyed using high resolution MBES bathymetry. II. and III. Bathymetric difference map outputs showing calculations of deposition (blue) and erosion (red). Between 2020 and 2021 (II) a level of detection threshold of 0.49 m was used, and between 2021 and 2023 (III) a level of detection threshold of 0.55 m was used. Insets of the regions denoted as a) to d) are shown in Figure 4 and Figure 5, and f) to k) in Figure 8, Figure 9 and Figure 10. 34

Figure 4: Planview morphology of the channel reaches with the position of knickpoints (KP), that are mapped at their inflection point, denoted in blue lines. Black lines denote the extent of profiles in Figure 5 and Figure 6. The reaches are shown as follows: a) The northern and southern tributary canyon, the canyon transition zone and the first channel bend; b) and c) the midchannel reaches including the straight reach and the bend dominated reach and the channel fork; d) The northern and southern distributary channels. 36

Figure 5: Profile view of northern canyon and upper channel (Figure 4). Crescentic bedforms are the dominant in-channel bedform with some knickpoints that eventually give way to just knickpoints (shown as knickpoint (KP) zones, which represents one or more inflection points). Crescentic bedforms in the upper canyon (inset profile) had the sharpest inflection points and most clearly defined shape in the 2023 survey. 37

Figure 6: Representative bathymetric profiles from bedform fields at different reaches of the channel. B-B', C-C', and D-D' were from the channel bends reach, E-E' was from the southern distributary channel (Figure 4) 38
Figure 7: Morphology of the lobes shown in MBES bathymetry. Inset maps show slope maps where sediment wave bedforms are present on both lobe complexes and that crescentic scours were observed on the southern lobe. 40
Figure 8: Bathymetric difference maps (Figure 3) of the canyons and upper reaches of the channel between 2020 and 2021 (f) and 2021 and 2023 (g) where deposition is shown in (blue) and erosion in (red), and the position of knickpoint inflection points (IP) which are observed to migrate up-channel between bathymetric survey intervals. The regions showing bathymetric change have similar extents but where between 2020 and 2021 there was erosion and deposition visible whereas between 2021 and 2023 there was predominantly erosion beyond the canyons. 42
Figure 9: Bathymetric difference map of the mid-channel reaches and channel fork between 2020 and 2021 (j) and 2021 and 2023 (k) where deposition is shown in (blue) and erosion in (red), and the position of knickpoints. Between 2021 and 2023 the magnitude of erosion is overall much higher within the channel and more overspill deposition is visible in the bedform fields. 44
Figure 10: Bathymetric difference map of the lobe between 2020 and 2021 (j) and 2021 and 2023 (k) where deposition is shown in (blue) and erosion in (red), and the position of knickpoints. The upper inset shows the formation of rills in the northern lobe complex in 2023 (overlaying Hillshade at 315 azimuth). The lower inset shows the dominant headless channels in the southern lobe (only active between 2021 and 2023) where certain scours appear to migrate up-channel indicating they may be knickpoints. 46
Figure 11: Calculated volumes of bathymetric change for the submarine channel system between 2020 and 2021 (top) and 2021 and 2023 (bottom) scaled to a yearly rate. The bars represent the

sum of all pixel cells multiplied by the channel resolution in each sub-region of the submarine channel system, with the red bars representing the negative pixel cells (erosion), the blue bars the positive pixel cells (deposition) and the green bars the net difference. 47
Figure 12: Calculated volumes of bathymetric change from different channel components between 2020 and 2021 (top) and 2021 and 2023 (bottom) scaled to a yearly rate. The bars represent the sum of all pixel cells multiplied by the channel resolution in each sub-region of the submarine channel system, with the red bars representing the negative pixel cells (erosion), the blue bars the positive pixel cells (deposition) and the green bars the net difference. 49
Figure 13: Volumetric change in each knickpoint zone (KPZ) between 2020 and 2021 (top) and 2021 and 2023 (bottom) scaled to a yearly rate. The bars represent the sum of all pixel cells multiplied by the channel resolution in each sub-region of the submarine channel system with the red bars representing the negative pixel cells (erosion) and the blue bars the positive pixel cells (deposition). KPZ 4 shows no volumetric change between 2021 and 2023 as the knickpoints here had disappeared and the resulting change could not be attributed to knickpoint movement. 52
Figure 14: Newly created knickpoints a) to e) between 2021 and 2023 with their mapped knickpoint inflection point (IP) in planview (top) and two-dimensional profiles (bottom) where red represents erosion and blue deposition. In a) to c) the new knickpoints were created in channel bends, whereas d) and c) occurred up- and down-channel (respectively) from where the ridge at the channel fork was located. In a) knickpoint inflection points in the 2023 bathymetric survey were observed to either appear or migrate to the position of previously mapped knickpoint inflection points in 2020 or 2021. In b) to e) the new knickpoints had a low relief of between 2 m to 4 m.....54
Figure 15: Graphic logs for the sediment cores showing dominant unit types. 61
Figure 16: MCMC age-depth model of modelled calibrated ^{14}C dates (plotted as R_date) in Core 13 with predicted 74-year BP ^{210}Pb depth and the 1964 AD ^{137}Cs depth. 65

Figure 17: Daily discharge for the Nass River (left Y-axis) and the tributary Ansedagan Creek (right Y-axis) throughout the during of the study period. Both discharge curves show similar timing in their discharge peaks, although not necessarily the same magnitude of change. Notably, Ansedagan Creek shows two discharge peaks higher than observed during the rest of the study period in 2021 where no discharge data is available for the Nass River. 78

Figure 18: Daily discharge measurements of the Nass River during the 2022 freshet (Water Office: Government of Canada 2023a), and a spring-neap tidal cycle during this period (Department of Fisheries and Oceans Canada tidal prediction station 09422 Gingolx, BC (https://tides.gc.ca/en/stations/09422)). Discharge peaks on June 8, 2022, during neap tide, which is then followed by a spring tide. 79

Figure 19: Location of the polygons where no change was expected beyond the background sedimentation. Bathymetric change was performed here, and the mean, median and standard deviation of the results were calculated (Table 9). 103

Figure 20: Example histograms of bathymetric change differencing results from the polygons where there was no expected change. These errors are approximately normally distributed and are clustered near zero (although they both skew positive). Each of the shown histograms had the highest median calculated change which was assumed to represent most of the error in the bathymetry and were thus used as the LOD threshold value. 105

Figure 21: Polygons of the mapped submarine channel system features used for volumetric budget segregation in the GCD change detection software (Bailey et al. 2022). 106

Figure 22: Plot of the measured ^{210}Pb activities in Core 13 with event-free core depth. Background ^{210}Pb activity was not reached. 108

Figure 23: Plot of the natural logarithm of the excess ^{210}Pb with the event-free core depth of Core 13 for the inclusive model. Background activity of 0.80 DPM/g was estimated using the average of the measured ^{226}Ra activities (Table 11). 109

Figure 24: Plot of the natural logarithm of the excess ^{210}Pb with the event-free core depth of Core 13 for the exclusive model where samples from the top 10 cm of the core are excluded. Background activity of 0.80 DPM/g was estimated using the average of the measured ^{226}Ra activities (Table 11). 109

Figure 25: Measured ^{137}Cs activity plotted with corrected event-free core depth in Core 13. ^{137}Cs peak identified at 61 cm. 112

Figure 26: Plot of the measured ^{210}Pb activities in Core 6 with the corrected event-free core depth. Background ^{210}Pb activity was interpreted to be reached between the 90 cm and 121.5 cm measurements. 114

Figure 27: Plot of the natural logarithm of the excess ^{210}Pb with corrected event-free core depth of Core 6. Background of 0.98 DPM/g was calculated from the average of ^{210}Pb activities between 121.5 cm to 230 cm corrected event-free core depth where the curve was shown to flatten (Table 14). 115

Figure 28: Plot of the natural logarithm of the excess ^{210}Pb with corrected event-free core depth of Core 6. Background of 0.81 DPM/g was calculated from the average of ^{226}Ra activities. 115

Figure 29: Measured ^{137}Cs activity plotted with corrected event-free core depth in Core 6. ^{137}Cs peak identified at 71 cm. 117

Figure 30: Plot of the measured ^{210}Pb activities in Core 39 with event-free core depth. Background ^{210}Pb activity was not reached. 119

Figure 31: Plot of the natural logarithm of the excess ^{210}Pb with core depth of Core 39. An event-free depth was not able to be established for this core. Background of 0.69 DPM/g was calculated from the average of ^{226}Ra activities (Table 14). 120

Figure 32: Measured ^{137}Cs activity plotted with core depth in Core 39. ^{137}Cs peak identified at 193 cm..... 121

Table of Tables

Table 1: Summary of Bouma sequence divisions (Bouma 1962). 6

Table 2: Sediment Cores collected during 2021 CCGS Vector Cruise, including type, location and length of core. Map location of Portland Inlet cores are shown in Figure 2. 27

Table 3: Volumes of surficial change calculated for the submarine channel system converted to yearly change. Volumes were converted to mass using a mean turbidite density of 2150 kg m^3. 43

Table 4: Knickpoint migration rates between the 2020-2021 bathymetric surveys and the 2021-2023 bathymetric surveys. Knickpoints denoted with an Arabic numeral were observed in 2020 and 2021, and those denoted with a Roman numeral were only observed in 2023. 55

Table 5: Sedimentary lithofacies determined from core logging and interpretation 58

Table 6: Sedimentation rates calculated from excess ^{210}Pb models. The sedimentation rate was used to calculate what core depth corresponds to 1964 AD (the expected peak of ^{137}Cs) which was presented with the core depth of the measured ^{137}Cs peak. 62

Table 7: Event-free-depths and modelled ^{14}C ages in Core 13 along with sampled material type. ..64

Table 8: Turbidite deposit return intervals based on radiometric dating and broken down by facies type. 66

Table 9: Mean, median and Standard Deviation of the vertical bathymetric change within the test polygons where no bathymetric change would be expected beyond the background hemi-pelagic sedimentation. The highest value for each survey interval (median of distal polygon for 2020-2021 and median of proximal for 2021-2023) was chosen as the error threshold for bathymetric differencing. All these values were higher than the expected sedimentation rates of 3.31 cm/year, 1.67 cm/year and 1.13 cm/year in the proximal, mid and distal parts of the channel (Table 6). 104

Table 10: Measured ^{210}Pb activities, the excess ^{210}Pb, and the natural logarithm of the excess ^{210}Pb calculations for Core 13 shown against core depths and event-free depths. 107

Table 11: Measured ^{226}Ra activities with core depth in Core 13. The average ^{226}Ra = 0.80 DPM/g. . 109

Table 12: Measured ^{137}Cs activities and error at the sampled core depth in Core 13. 111

Table 13: Measured ^{210}Pb activities, the excess ^{210}Pb, and the natural logarithm of the excess ^{210}Pb calculations for Core 6 shown against core depths and event-free depths. NA denotes where the natural logarithm of the excess ^{210}Pb has no real number solution. 112

Table 14: Measured ^{226}Ra activities with core depth. The average ^{226}Ra = 0.81 DPM/g in Core 6. ... 116

Table 15: Measured ^{137}Cs activities and error at the sampled core depth in Core 6. 116

Table 16: Measured ^{210}Pb activities, the excess ^{210}Pb, and the natural logarithm of the excess ^{210}Pb calculations for Core 13 shown against core depths. 117

Table 17: Measured ^{226}Ra activities with core depth in Core 39. The average ^{226}Ra = 0.72 DPM/g. . 120

Table 18: Measured ^{137}Cs activities and error at the sampled core depth in Core 39. 120

Table 19: Samples collected for ^{14}C dating in Core 13 with the material type, the pre-treatment, the analysis lab, and the unmodeled ^{14}C date. 122

Acknowledgements

I owe a deep gratitude to my supervisors Cooper and Eva for their guidance, support and shared passion throughout the duration of this project. Cooper - throughout this project your passion for marine sedimentology showed and was highly infectious! I enjoyed our many science discussions which I always left feeling a renewed excitement for this project, and I appreciate your willingness to give your time and mentorship throughout the last two years. Eva – you dove into a subject outside of your realm of expertise and were still able to provide insightful scientific contributions which provided an excellent outside perspective to bring fresh ideas to this project and was immensely helpful in improving this direction and writing of this manuscript. I would also like to thank my committee members Phil Hill and Gwyn Lintern for bringing their extensive background in marine sedimentology that was able to broaden the scope of this project and help develop the key insights that emerged in this study.

I would also like to thank the Geological Survey of Canada for the Research Affiliate Program funding. Moreover, I would like to thank everyone at PGC for the many lab room discussions, hallway chats, and fun lunchroom conversations. The passion that everyone here has for their work was truly inspiring. I am especially thankful to Randy Enkin for the guidance and support through the core splitting and physical properties measurement and helping me with the carbon date modelling, Zhen Li and Tark Hamilton for their guidance in laboratory methods and lively discussion about my core interpretations, and Navinder Hundal and Llewellyn Ward for their help X-Ray imagine cores. I would like to thank Geordie Wilson from the Canadian Hydrographic Service for providing me the multibeam bathymetry uncertainty layers. I would also like to thank Wyatt Maddox, Jeff Crompton, and the science crew of CCGS Tully October 2023 cruise for allowing me to help with their fieldwork.

I would like to thank the Faculty and Students at the University of Victoria Department of Geography for creating a fun and supportive environment to be part of, especially those members of the cohort who became part of the regular rock-climbing crew. I would also like to thank all the roommates who I have gotten to share The Teahouse with for the support, the sense of community, the shared meals, the backyard concerts, and making living in a shared house feel easy. I would also like to thank the members of Diploids, Heron Hereon, the PGC Band, and everyone else who I have played music with in the last two years for allowing me a creative outlet outside of science. Finally, I would like to thank my family for all their support throughout this project, with a special shoutout to Uncle Graham with whom I was able to have in depth conversations about my research with thanks to his background in geophysics.

Chapter 1: Introduction

Motivation

Turbidity currents are a phenomenon of fundamental interest to researchers as they are both a powerful mechanism for sediment transport and pose hazards to communities and infrastructure. Turbidity currents are a type of subaqueous sediment density flow, which is an umbrella term that covers a range of density-driven sediment flow processes including grain flows, liquified/fluidized flows, debris flows and turbidity currents, which are each grouped by the flow state, flow rheology and sediment support mechanism of the entrained sediment particles (Shanmugam 1997, Talling *et al.* 2012). Volumetrically, turbidity currents (along with rivers) make up one of the two most dominant mechanisms of sediment transport on earth meaning they are a significant erosional and depositional force (Milliman and Syvitski 1992, Bornhold *et al.* 1994, Fine *et al.* 2005, Canals *et al.* 2006, Talling *et al.* 2007, 2012, Peakall and Sumner 2015). Through these flows, sediment can be transmitted from the continents all the way to the deep ocean and are the dominant source of sand to deep sea basins (Piper and Normark 1983, 2001, Curray *et al.* 2002, Talling *et al.* 2013, 2022, Baker, Talling, *et al.* 2024). Turbidity currents also pose a geohazard risk, where flows have destroyed underwater infrastructure such as submarine power cables, fiber optic cables, or pipelines (Paull *et al.* 2002, Fine *et al.* 2005, Hsu *et al.* 2008, Gavey *et al.* 2017, Talling *et al.* 2022). Despite this risk, few of these flow events have been monitored until recently (Talling et al. 2022). Furthermore, deposits from turbidity currents are an important sink of organic carbon on geological timescales and may also be an important source of burial of microplastics (Hage et al. 2020, 2022, Pohl et al. 2020, Baker, Hage, et al. 2024). Therefore, quantifying sediment transport from turbidity

currents is an important component of understanding sedimentary processes and lithological cycles, and the geohazard risk they pose.

Turbidity currents can be challenging to study directly as the presence of water obscures direct observation, and their destructive nature presents challenges to instrumentation. As a result, historically, much of our understanding of deepwater turbidity currents comes from studying the deposits of these flows (Bouma 1962, 1964, Lowe 1982, Weimer and Link 1991, Shanmugam 1997, Talling et al. 2012) or by simulating flows using laboratory experiments or mathematical modelling (Middleton 1966, Mulder et al. 1998, Kneller and Buckee 2000, Kostic and Parker 2006, Dorrell et al. 2018, Pohl et al. 2019). One method of studying turbidity current flows is looking at lithified deposits in the rock record, either in outcrops that have been uplifted into a terrestrial setting, or in drill cores from either marine or terrestrial locations (Lowe 1982, Shanmugam 1997, Talling et al. 2012). These flow events can also be studied pre-lithification by collecting bathymetric or sub-bottom sonar survey data to understand the lateral and vertical extent, and through collecting sediment cores to understand the localized structure of the flow deposit (Mulder et al. 1997, Picot et al. 2016, Symons et al. 2017). This work is difficult and costly to conduct in deepwater environments, however, and both methods also only describe the depositional conditions of these flows, and not how they evolve during their transport phase. Laboratory and mathematical modelling have been used to fill that gap to understand how the flows evolve and can be developed to try and simulate real-world flow events which are then compared to observations about the deposition of those events (Bowen et al. 1984, Mulder et al. 1997, 1998, Kostic and Parker 2006, De Leeuw et al. 2018, Pohl et al. 2019, Wilkin et al. 2023). Information on turbidity current events has also been obtained through in situ study with flow monitoring instruments or sediment traps, or from destructive flows that damage underwater infrastructure (Prior et al. 1987, Fine et al. 2005, Hsu et al. 2008, Lintern et al. 2016, Talling et al. 2022).

The ultimate goal of studying turbidity currents is developing a full understanding of these flows from the initiation through to the final depositional phase, and how the environments that host frequent flows respond and evolve through time. This is challenging as there is an inherent unpredictability in the initiation of these flow events that makes direct observation difficult, and is pronounced in deep-water environments where turbidity currents may have return times on time scales of 1000s of years or greater or may only been initiated with other large events such as an earthquake (Fine et al. 2005, Hsu et al. 2008, Goldfinger et al. 2012, Talling et al. 2013). Although laboratory modelling can simulate flow conditions, there are issues that stem from recreating natural conditions at the laboratory scale (Middleton 1966, Mulder et al. 1998, Kneller and Buckee 2000, De Leeuw et al. 2016). Lithological and sedimentological stratigraphy is useful for developing geohistorical records of turbidity current flow events within a system but are costly to perform in the deep ocean. Likewise, deploying and recovering in situ monitoring equipment is logistically difficult in these locations. Moreover, in situ monitoring instruments have been damaged by turbidity currents during monitoring studies (Prior et al. 1987, Lintern et al. 2016, Talling et al. 2022), highlighting the destructive potential of these flows. Although all these methods are valuable for contributing to a more complete understanding of turbidity current environments, they are challenging to implement all within a study site, especially in deep-water settings.

To circumvent the challenges posed by studying turbidity current settings in the deep ocean, certain deltas in more shallow water settings have been shown to provide valuable sites for understanding the mechanisms and characteristics of these events. These sites are more accessible which allows them to be studied using sedimentological, geomorphological and in situ study methods. Studies at these sites have led to great advances in our understanding of how turbidity currents alter the morphology of these systems (Hughes Clarke 2016, Hage et al. 2018, Heijnen et al. 2020, Zulkifli et al. 2024), have helped develop insight on how turbidity currents are

initiated (Clare et al. 2016, Lintern et al. 2016, Hizzett et al. 2018, Bailey et al. 2021, 2023, Hill and Lintern 2021), have allowed for the quantification of sediment budgets and stratigraphic reconstructions of submarine channel systems (Stacey et al. 2019, Vendettuoli et al. 2019, Heijnen et al. 2022, Pope, Cartigny, et al. 2022), and have provided estimates of organic carbon fluxes from transport by turbidity currents (Hage et al. 2020, 2022). However, further work is needed to fully understand the character and distribution of flow events, how these systems evolve morphologically, how they build and maintain stratigraphy, and what site characteristics causes this to differ between systems (Talling et al. 2015, Gales et al. 2019, Hodgson et al. 2022). Herein, this study hopes to address the gaps in knowledge by studying the Nass delta and channel in Portland Inlet, a submarine channel system which has not been documented previously. Therefore, the goal of this project is to assess turbidity current activity at the Nass delta to determine the frequency and magnitude of these flow events and describe how these shape the resulting seabed morphology.

Objectives

In this study, the following objectives will be addressed:

1. Determine how geomorphologically active the seabed is between bathymetry survey intervals and analyse specific seabed morphologies and sub-bottom structure to infer turbidity current characteristics.
2. Evaluate potential initiation mechanisms for turbidity currents on the Nass Delta.
3. Identify and describe turbidity current deposits in the stratigraphic record to examine depositional characteristics.
4. Develop a sedimentation rate model to date turbidite deposits and determine reoccurrence rates.

5. Characterize the extent of the seafloor geohazard potential from turbidity currents at the Nass Delta.

Background

Turbidity current Stratigraphy

Turbidity currents have been described in the rock record as they leave discernable deposits (Bouma 1962, Stauffer 1967, Lowe 1982, Labaume *et al.* 1987, Talling 2001, Talling *et al.* 2012). Identifying these deposits (called turbidites) within sedimentary strata is useful for researchers reconstructing paleo-geological environments and past turbidity current flow events (Adams 1990, Goldfinger *et al.* 2003, 2012). Furthermore, locating and describing turbidites and other density flow deposits is frequently of interest to oil-exploration geologists as deposits can act as traps to host hydrocarbon reservoirs (Weimer and Link 1991, Mcgee *et al.* 1994, Kneller 1995, Stow *et al.* 2000, Talling 2001). Within the literature, other types of sediment density flow deposits can be misdescribed as turbidites (Shanmugam 1997). This issue is further complicated as sediment density flows can begin with one flow regime and then transition to another during its flow phase, whereas the resulting deposit only holds information about the flow conditions during the depositional phase of the flow (Shanmugam 1997, Talling et al. 2012).

Turbidites were first described in the rock record by Kuenen and Migliorini (1950) who concluded that graded bedding in deep sea deposits were produced by turbidity currents. A model for describing these deposits was proposed by Bouma (1962), who developed the “Bouma Sequence” for low density flows. The sequence is grouped into five divisions labeled A-E that allows depositional flow conditions to be deduced by the distinct characteristics of deposits (see Table 1 for a general summary). Depending on the characteristics of the flow or erosion, not all sequences

may be present or retained in the deposit. This work was expanded on by Lowe (1982) to differentiate between low density and high-density turbidity currents with the “Lowe Sequence”. Overtime, the description of sediment density flows in the rock record has expanded to deposits beyond just turbidites. A culmination of a body of literature has allowed for more detailed understanding of flow conditions based on observed deposits to better classify the sediment density flows (Walker 1976, Shanmugam 1997, Talling 2001, Talling et al. 2012). However, there will always be gaps in the stratigraphic record, and given how active many of these systems are it is still an open question of what the preservation potential of flow deposits are, and if it will be retained or eroded before lithification (Vendettuoli et al. 2019).

Table 1: Summary of Bouma sequence divisions (Bouma 1962).

Division	Flow Condition	Deposit Characteristics
Bouma T_a	When flow energy that is initially high enough to keep coarse grained material in suspension drops below this critical energy level	Massive to normally graded fine- to course-sand; Pebbles, rip-up clasts, and/or dish structures may be present
Bouma T_b	Upper flow regime where energy is high enough to move sand grains by traction	Planar-laminated, fine- to medium-grained sand; sole markings may be present
Bouma T_c	Lower flow regime where energy is high enough to move sand grains by saltation	Ripple-laminated, fine-grained sand; convolute laminations or flame structures may be present

Bouma T_d	Suspension settling under low current	Parallel-laminated, silt
Bouma T_e	Suspension settling under no current	Massive, ungraded mud

More recent studies on turbidity current flows include studying sedimentary stratigraphy before lithification. The advantage of using sediment stratigraphy is that there is a lower likelihood that the strata has been eroded or altered and therefore retains clearer structure of the depositional phase of the turbidity current and is more likely to express the units of the Bouma sequence with distinct boundaries. In the context of fjords in British Columbia several distinct facies are common in relation to turbidity current channel systems. For example Stacey et al., (2019) identified five unique facies in the Squamish Delta, including three Bouma sequence associated turbidity current facies that exhibit variations of the Bouma Ta, Tb and Te divisions, a debris flow unit, and a background hemi-pelagic sedimentation accumulation frequently present between turbidity current deposits. Similar facies units have been identified in Bute Inlet (Pope, Cartigny, et al. 2022). The identification of these units in sediment cores has allowed for turbidity current event histories to be established and to develop flow event reoccurrence intervals (Stacey 2014, Stacey et al. 2019).

Turbidity current Induced Surficial Morphology

Due to the dynamic and energetic nature of turbidity currents, they create several characteristic seabed morphologies by their ability to erode, deposit, and move sediment. Turbidity currents can occur in unconfined slope faces, but many regions that host frequent flow events commonly result in the incision of a submarine canyon or channel (Talling et al. 2013). Channel formation has been

replicated using laboratory models which gives insight into how repeated flow events create and maintain submarine channels through both incision and levee building processes (De Leeuw et al. 2016). A turbidity current on an unconfined slope will result in differential erosional and depositional patterns where turbulence under the flow axis has the potential to erode the seabed, where as the outside of the flow is energetically weaker and deposits sediment at the margins creating levees subparallel to the flow direction (De Leeuw et al. 2016, 2018). This pattern will have a semi-confining effect on flows, which concentrates their erosive energy between the levees which leads to the development of a channel (De Leeuw et al. 2016). Gradually, the incision will be deep enough to contain most of the energy and sediment concentration of the flows and propagate their energy forward (De Leeuw et al. 2016, 2018).

As they develop, submarine channels that stretch beyond delta fronts and reach environments with lower gradients may curve and change direction. In certain channel systems with a low average slope, submarine channels have been shown to develop bends that look similar to meandering bends in terrestrial fluvial systems (Peakall et al. 2000, Conway et al. 2012). Turbidity current flows that pass through channel bends can erode the outer bends and deposit on the inner bend creating a point-bar (Ruffell et al. 2024, Zulkifli et al. 2024). Due to the centrifugal force acting outward as the turbidity current enters the channel bend, the secondary flow develops an asymmetric helical cell that is tilted resulting in superelevation of the flow on outer bank, which has been shown to be more pronounced in submarine channels as opposed to river systems due to the density differences between the turbidity current and ambient seawater (Dorrell et al. 2013, Wells and Dorrell 2021). There is some debate about whether it is a different mechanism that controls bends in submarine channels as laboratory models and field studies suggest that secondary flow within the turbidity currents may be often river-reversed where the basal component of helicoidal flow is oriented towards the outer bank as opposed to river-like where it is

oriented towards the inner bank (Peakall et al. 2000, Parsons et al. 2010, Azpiroz-Zabala, Cartigny, Sumner, et al. 2017, Azpiroz-Zabala et al. 2024, Zulkifli et al. 2024). Large flows can also overtop the levees and deposit outside of the channel via flow stripping (Piper and Normark 1983, Peakall et al. 2000, Huang et al. 2012, Stacey et al. 2019). These flows can form out-of-channel morphologies such as sediment wave bedforms when the overspill has sufficient energy (Huang et al. 2012, Symons et al. 2016, Stacey et al. 2019).

In channel morphologies characterized by localized changes of bathymetry are commonly found in well developed submarine channels. One of these morphologies are cyclic steps, a crescentic bedform that crosses the channel in an arc shape that faces convex up-channel and is approximately perpendicular at the channel axis (Hughes Clarke 2016, Covault et al. 2017, Hage et al. 2018, Slootman and Cartigny 2020). Cyclic steps are associated with changes in flow regimes during turbidity currents (Cartigny et al. 2011, 2014, Slootman and Cartigny 2020). When the turbidity current flow travelling down the channel passes over a drop in bathymetry it plunges downward (Slootman and Cartigny 2020). Then when the slope angle shallows, this causes the flow to change from a supercritical regime to a subcritical regime (Hage et al. 2018, Slootman and Cartigny 2020). This can be expressed mathematically by a change in the Froude Number (Fr) which is a ratio between the inertial and gravitational forces of the flow. Supercritical flow occurs when $Fr > 1$ and subcritical flow occurs when $Fr < 1$ (Postma and Cartigny 2014, Slootman and Cartigny 2020). When a flow transitions from supercritical to subcritical a hydraulic jump may occur within the flow, which creates circular turbulence at the interface of the flow regime change (Postma and Cartigny 2014, Slootman and Cartigny 2020). This turbulence generates an alternating pattern of erosion and deposition causing it to migrate up-channel (Hughes Clarke 2016, Slootman and Cartigny 2020). Although the initiation of cyclic steps is not fully understood, the current hypothesis is that the hydraulic jump can begin on a localized slope change, which then creates a

feedback to self maintain its step structure, with drops of approximately 1 m to 5 m (Covault et al. 2017, Hage et al. 2018, Slootman and Cartigny 2020).

Other common in-channel morphological features are termed channel knickpoints. Although they have also been connected to hydraulic jumps in turbidity current systems, they are characterized separately by a steeper drop in bathymetry, sharper crests and greater variation in morphology (Paull et al. 2011, Guiastrennec-Faugas et al. 2020, Heijnen et al. 2020, Chen et al. 2021). Submarine channel knickpoints are also notable because in channels with high turbidity current activity they are known to migrate up-channel rapidly at rates of up to 600 m/year (Guiastrennec-Faugas et al. 2020, Heijnen et al. 2020). The up-channel migration erodes sediment on the up-channel side and often deposits it on the down-channel side (Guiastrennec-Faugas et al. 2020, Heijnen et al. 2020, 2020). As a result, knickpoints are a mechanism of in-channel sediment transport and are hypothesized to contribute to creating and maintaining the shape of the channel (Guiastrennec-Faugas et al. 2020, Heijnen et al. 2020, 2022).

When flows reach the end of the incised channel, they experience a loss-of-confinement and flow expansion, and deposition eventually dominates creating a fan-shaped depositional lobe (Bowen et al. 1984, Garcia and Parker 1989, Hodgson et al. 2022). The interface has frequently been described as the channel-lobe transition zone and is often associated with a decrease in slope and features such as supercritical bedforms and seafloor scours (Normark et al. 1979, Macdonald et al. 2011, Hofstra et al. 2015, Hodgson et al. 2022). The decrease in slope has been suggested to create a hydraulic jump (Garcia and Parker 1989, Kostic and Parker 2006, Hodgson et al. 2022, Wilkin et al. 2023), which may explain the scours and bedforms observed in these regions. Flow relaxation has also been suggested as a mechanism to explain the scouring without a hydraulic jump, where loss of confinement leads to the flow spreading out, which decreases the depth of the velocity maximum leading to an increase in basal shear stress (Pohl et al. 2019).

Turbidity Current Magnitudes and Flow Characteristics

Direct monitoring of turbidity currents shows that flows will behave differently depending on their magnitude. Several models have been advanced to describe how different magnitudes of flow will interact with the seafloor as it travels. Smaller flows often dissipate quickly with short run-out distances (Hughes Clarke 2016, Stacey et al. 2019, Heijnen et al. 2022) as they deposit too fast to maintain a higher density than the ambient seawater (Parker 1982, Heerema et al. 2020). Larger flows may travel in a flow state termed autosuspension where either the flow does not interact with the sediment on the seafloor due to turbulence in the flow suppressing deposition (termed sediment bypass) or will erode and deposit on the seafloor at approximately equal rates (Bagnold 1962, Parker 1982, Heerema et al. 2020, Wells and Dorrell 2021). Other flows appear to self-ignite as they continuously erode the seafloor, which increases the density of the flow creating a positive feedback loop to continue to travel further until a point where it changes flow state (Parker 1982, Parker et al. 1986, Heerema et al. 2020). Further studies have given insight into the structure of turbidity currents which shows that large magnitude turbidity currents often have a thin dense basal layer that travels at or near the head of the flow, and then a less dense tail that travels at a slower velocity behind the head (Xu et al. 2014, Hughes Clarke 2016, Azpiroz-Zabala, Cartigny, Talling, et al. 2017, Paull et al. 2018, Heerema et al. 2020, Simmons et al. 2020, Hill and Lintern 2022, Pope, Cartigny, et al. 2022, Talling et al. 2022). These studies have advanced further models for flow states that can allow for both ignitive and auto-suspension behaviour including flow stretching of the dense frontal component to accommodate ignitive erosion (Pope, Cartigny, et al. 2022) and the travelling wave model where the frontal component is fed by erosion, but maintains its density by shedding sediment into the tail component (Heerema et al. 2020, Hill and Lintern 2022, Baker, Talling, et al. 2024)

The magnitudes of turbidity currents also affect the sediment transport rates and morphological change within submarine channels. Several studies have proposed a bimodal pattern of turbidity current flow magnitudes where smaller dissipative flows occur frequently in the upper reaches of submarine channels and canyons and then larger magnitude ignitive flows occur less frequently but travel greater distances from the initiation source (Stacey et al. 2019, Heijnen et al. 2022, Talling et al. 2022). A recent study in Bute Inlet, British Columbia has advanced a model for how different magnitudes of turbidity currents cause knickpoint migration resulting in redistribution of sediment within a submarine channel called the 'shuffle-and-flush' model (Heijnen et al. 2022). Initially, small turbidity currents deposit sediment in the upper reaches of the submarine channel (from dissipative flows), then successive medium sized flows 'shuffle' the deposited sediment down-channel in series as knickpoints are activated and migrate up-channel, then a large ignitive flow will 'flush' the channel by eroding the emplaced sediment and deposit it on the terminal lobe (Heijnen et al. 2022). This model favours a type of sediment bypass where knickpoint migration will ultimately result in balanced erosion and deposition over time during the 'shuffling' phase without auto-suspension of a single flow (Heijnen et al. 2022). However, it is unclear how these knickpoints are formed or if they can be removed in these different flow conditions (Heijnen et al. 2022).

Initiation Mechanisms

In situ and laboratory studies of turbidity currents in fjord deltas have provided insight into how these flows are initiated. Proposed triggers include, submarine slope failures (which may be triggered by an external source such as seismic shaking, storm wave action etc.), elevated river discharge, river sourced sediment plumes, and remobilization of deltaic sediments from tidal flow or wave action (Talling 2014, Clare et al. 2016, Hizzett et al. 2018, Bailey et al. 2021, 2023, Talling et al. 2023). Originally, turbidity currents connected to river plumes were predicted to only occur

during hyperpycnal conditions (Mulder and Syvitski 1995), but monitoring studies have shown that hypopycnal rivers plumes still can trigger turbidity currents via convective settling processes (Parsons et al. 2001, Hizzett et al. 2018, Hage et al. 2019, Hill and Lintern 2021). A further connection can be drawn between dilute river plumes that deposit sediment on the delta that are resuspended and concentrated during strong tidal currents (often associated with spring tides) and can reach a high enough density gradient with the ambient water to trigger turbidity currents (Parsons *et al.* 2001, Hage *et al.* 2019, Hill and Lintern 2021). Monitoring of turbidity currents where the trigger mechanism can be identified shows that different flows at a given site can result from different trigger types, that different combinations of variables may generate flows (e.g., higher discharge and lower tides, delta slope failures lagged after discharge peaks etc.), and that there is not a strong relationship between the different triggers and observed magnitude of the flows (Clare *et al.* 2016, Hizzett *et al.* 2018, Hage *et al.* 2019, Bailey *et al.* 2023). Further work is needed to better understand how these initiation mechanisms interact and vary between different river fed delta systems.

Turbidity current Monitoring in British Columbia

Shallow water delta-front monitoring sites have proven to be useful for studying turbidity current flows and their resulting morphology and deposits. Several deltas on the west coast of British Columbia host frequent turbidity currents and studying these sites have led to great advances in our understanding of these systems (Conway *et al.* 2012, Gales *et al.* 2019). Geographically, they are generally more accessible, often host frequent turbidity current flows, and their comparatively shallow depths make the logistics of studying the seabed and deploying in situ monitoring equipment more feasible (Hughes Clarke 2016). Based on all these factors, several of these shallow water delta locations – most notably the Squamish Delta and Bute Inlet – have been the

host of some of the most detailed studies on turbidity current systems to date (Hughes Clarke 2016, Stacey *et al.* 2019, Heijnen *et al.* 2022). Studies on these systems generally comprise of a combination of spatial analysis of morphological change conducted from repeat collection of bathymetry surveys, sediment stratigraphy analysis (pre-lithification) through targeted sediment coring, study of sub-surface structure through collected sub-bottom acoustic lines, and direct monitoring using in situ instruments (e.g., (Zeng *et al.* 1991, Hughes Clarke 2016, Hage *et al.* 2018, Stacey *et al.* 2019, Vendettuoli *et al.* 2019, Heijnen *et al.* 2022).

Chapter 2: From low magnitude flows to thresholding flush events: Insights from turbidity flow sedimentation in the Nass Delta submarine channel system

Authors: Parkinson, Felix; Stacey, Cooper; Kwoll, Eva; Hill, Phil, Lintern, Gwyn

Targeted Journal: Earth Surface Processes and Landforms

Introduction

Turbidity currents are one of the most powerful mechanisms of sediment transport in the marine environment. These sediment density flows often incise into the seabed, carving out submarine channels that act as conduits to move sediment from the continents to the deep ocean (Talling *et al.* 2022). As a result, they are an important component of oceanic sediment fluxes, and contribute to the burial of carbon and microplastics (Hage *et al.* 2020, 2022, Pohl *et al.* 2020, Pope, Heijnen, *et al.* 2022, Baker, Hage, *et al.* 2024). However, they also pose a significant geohazard risk to underwater infrastructure such as submarine cables and pipelines (Piper and Savoye 1993, Fine *et al.* 2005, Hsu *et al.* 2008, Mosher *et al.* 2010, Talling *et al.* 2013, Gavey *et al.* 2017).

Previously, our understanding of turbidity currents came from describing their deposits in the rock record, numerical modelling, and flume tank experiments (Bouma 1962, Lowe 1982, Mulder *et al.* 1998, Kneller and Buckee 2000, Talling *et al.* 2012). However, advances in marine surveying technologies in recent years have improved our understanding of turbidity current systems by allowing for direct monitoring of the frequency and flow structure of turbidity currents using Acoustic Doppler Current Profilers (ADCPs), repeat bathymetric surveying to analyse surficial

change on the seabed in response to turbidity currents , and precision coring of seafloor sediments to stratigraphically characterize turbidity structure and reconstruct the frequency of flows (Hughes Clarke 2016, Symons *et al.* 2017, Stacey *et al.* 2019, Heijnen *et al.* 2022). Certain delta-submarine systems experience frequent turbidity currents which has allowed for high detailed studies of turbidity current systems using the methods described above, including in other regions of the coast of British Columbia, Canada such as the Squamish Delta (e.g., (Hughes Clarke 2016, Hage *et al.* 2018, 2019, Stacey *et al.* 2019, Vendettuoli *et al.* 2019)), the Fraser Delta (e.g., (Lintern *et al.* 2016, Hill and Lintern 2022, 2022)), and Bute Inlet (e.g., (Heijnen *et al.* 2020, 2022, Chen *et al.* 2021, Pope, Cartigny, *et al.* 2022, Bailey *et al.* 2023)). Other deeper water canyon environments have been studied using similar methods, e.g., the Monterey Canyon (Paull *et al.* 2002, 2011, 2018, Xu *et al.* 2013, 2014, Maier *et al.* 2019, Heerema *et al.* 2020, Wang *et al.* 2020), the Var Canyon (Khripounoff *et al.* 2009, 2012, Heerema *et al.* 2022), and the Congo Canyon (Azpiroz-Zabala, Cartigny, Talling, *et al.* 2017, Simmons *et al.* 2020, Pope, Heijnen, *et al.* 2022, Talling *et al.* 2022, Ruffell *et al.* 2024).

An advance that has come from studying these delta-submarine channel systems has been to develop a clearer understanding of the frequency of different magnitudes of turbidity current flows that occur in these systems, and how the different magnitudes of flow modify the seafloor. The Squamish delta and Bute Inlet systems have been shown to experience frequent small magnitude turbidity currents that dissipate in the upper reaches of the submarine channels, and then less frequent but larger magnitude flows that travel to more distal settings of the channel system and leave bigger deposits that contribute to lobe building (Hughes Clarke 2016, Stacey *et al.* 2019, Heijnen *et al.* 2022, Pope, Cartigny, *et al.* 2022). Several models have been proposed to explain how turbidity currents travel different distances based on their flow states by classifying them as either in a dissipation state, where the deposition of sediment decreases the flow density in a

negative feedback loop (Parker 1982, Sequeiros *et al.* 2009, Heerema *et al.* 2020); in autosuspension, where the turbidity current is in a state of equilibrium and either does not interact with the channel (sediment bypass) or erodes and deposits at approximately the same rate as it travels (Bagnold 1962, Pantin 1979, Stevenson *et al.* 2015, Heerema *et al.* 2020); or an ignition flow state, where the turbidity current predominantly erodes sediment as it travels, that increases the density of the flow creating a positive feedback loop (Parker 1982, Parker *et al.* 1986, Sequeiros *et al.* 2009, Heerema *et al.* 2020). With more recent in-situ flow monitoring studies, these models have been expanded to include the traveling wave model and the flow stretching model that can account for turbidity currents that exhibit both auto-suspension and ignition flow behaviour (Heerema *et al.* 2020, Hill and Lintern 2022, Pope, Cartigny, *et al.* 2022, Baker, Talling, *et al.* 2024). A conceptual model that has been advanced to characterize how different flow magnitudes of turbidity currents transport sediment within submarine canyons are 'filling' and 'flushing' flows (Piper and Savoye 1993, Paull *et al.* 2005, Canals *et al.* 2006, de Stigter *et al.* 2007, Piper and Normark 2009, Masson *et al.* 2011, Allin *et al.* 2016, Azpiroz-Zabala, Cartigny, Talling, *et al.* 2017, Heijnen *et al.* 2022, Ruffell *et al.* 2024). Small frequent dissipative turbidity currents deposit sediment in the upper parts of the canyon, then infrequent large magnitude turbidity currents will erode this built up sediment and 'flush' it down the canyon (Piper and Normark 2009, Masson *et al.* 2011, Allin *et al.* 2016, Heijnen *et al.* 2022). This model has been further expanded to the 'shuffle-and-flush' model for submarine channels based on observations in Bute Inlet, which proposes a 'shuffle' phase where the sediment deposited by 'filling' flows is remobilized by larger mid-sized turbidity currents and 'shuffled' incrementally down the length of the channel and creating localized zones of deposition and erosion based on in-channel morphology (Heijnen *et al.* 2022). Then these localized deposits along the length of the channel are eroded and transported to the lobe during the 'flushing' phase (Heijnen *et al.* 2022). However, further studies are needed to

assess how broadly applicable this model is, and how it interacts with the different turbidity current flow states.

Knowledge gaps exist on how these different turbidity current magnitudes and flow states interact with and affect in-channel bedforms (Heerema *et al.* 2020). Crescentic bedforms, small sediment waves which have been interpreted as cyclic steps that develop in supercritical flow conditions and migrate upslope, are often found on delta slopes and in the proximal reaches of submarine canyon and channels (Hughes Clarke 2016, Hage *et al.* 2018, Chen *et al.* 2021). Another notable morphological feature in submarine channels are knickpoints, which are sharp changes in channel gradient that migrate up-channel in response to passing turbidity current flows (Guiastrennec-Faugas *et al.* 2020, Heijnen *et al.* 2020, Chen *et al.* 2021). These knickpoints have been observed to affect the transport of sediment down-channel, in both 'shuffling' flows which erode sediment as the knickpoints migrate up-channel and deposit it down-channel (Guiastrennec-Faugas *et al.* 2020, Heijnen *et al.* 2020, 2022), and 'flushing' flows where they are primarily erosive in the channel and transport the sediment to the terminal lobe (Ruffell *et al.* 2024). How knickpoints are created or disappear is poorly understood as there are few observations. Flume experiments have demonstrated that knickpoints can be generated by turbidity currents passing over an erodible bed (Toniolo and Cantelli 2007). In Bute Inlet, new knickpoint were observed to appear in knickpoint zones, and were attributed to a larger knickpoint breaking up and creating smaller knickpoints in the process (Heijnen *et al.* 2020). In the Congo Canyon a knickpoint was observed to develop up-channel from the location of a landslide on the canyon wall that dammed the channel floor, where the blockage had caused sediment infill (Pope, Heijnen, *et al.* 2022). In the Capbreton Canyon, three knickpoints were observed to form at a channel bend that had previously been partially blocked by point bar deposition creating a constriction (Guiastrennec-Faugas *et al.* 2021). It is

unclear if there is a unifying mechanism for the creation of knickpoints, and if that requires a certain threshold magnitude and/or state of turbidity current flow to induce their formation.

Aims

To help address some of these gaps a new submarine channel system is examined by looking at bathymetric change and turbidity current deposits in the stratigraphic record. The objectives of this study are to:

- Describe the morphology of an active delta-fed submarine channel system that has not previously been studied.
- Quantify surficial change between intervals of bathymetric surveying to characterize what magnitudes of turbidity current flows occur in this submarine channel system and test the 'shuffle-and-flush' model in a new setting.
- Characterize how bedforms inside and outside the channel respond to turbidity currents.
- Reconstruct the frequency return intervals of turbidity currents that are retained in the stratigraphic record.
- Assess the geohazard potential created by turbidity currents in the study region.

Study Site

The Nass Delta is located in Nass Bay and Iceberg Bay near the community of Gingolx in British Columbia, Canada (Figure 1). The delta was formed by the Nass River, which flows for 400 km from the Skeena Mountains with a drainage area of approximately 25,000 km^2 (Fissel *et al.* 2017). Average discharge in the Nass River has been measured to be 780 $m^3 s^{-1}$ which typically increases to 2200 $m^3 s^{-1}$ during the spring freshet, and has episodically high discharge of up to 6000 $m^3 s^{-1}$ in the fall months (Fissel *et al.* 2017). The freshet has also been shown to elevate concentrations of

hypopycnal sediment transport delivered from the Nass River, with a sediment plume that travels up to 40 km from Nass Bay (Fissel *et al.* 2017). The dominant bedrock unit of the Nass Watershed is the Bowser Group, which is comprised of an assemblage of Mesozoic Era sedimentary rocks (Nelson 2008). Between 1668 and 1714 the Tseax volcanic cone erupted within a tributary drainage basin of the Nass River (Higgins 2009). Low viscosity lava flows reached the Nass Valley and modified the position of the river (Higgins 2009, Le Moigne *et al.* 2022).

Nass Bay connects to Portland Inlet and the adjacent Portland Canal and Observatory Inlet, which are marine fjords that formed during the Pleistocene Glaciations (Blaise *et al.* 1990). The width of the fjord varies from 4 km to 5 km in the study area (Figure 1). The bedrock geology surrounding the northern region of Portland Inlet and Nass Bay are an un-named sequence of intrusive granodioritic plutons from the Cenozoic Era, whereas the southern region is dominated by the Central Gneiss Complex of Paleozoic to Cenozoic metamorphic rocks (MacIntyre *et al.* 1994). Oceanographic studies of Portland Inlet have shown that there are tidal heights of up to 7 m (Pickard 1961) with tidal currents up to 1 m s^{-1} in Nass Bay that create complex patterns of circulation resulting in spatial variability in the distribution of bottom shear stress (Fissel *et al.* 2017). A hydrographic mapping cruise first surveyed Portland Inlet with high resolution multibeam echosounder (MBES) data in 2020 where a submarine channel was observed to extend from the Nass Delta into Portland Inlet, which is the channel system described in this study.

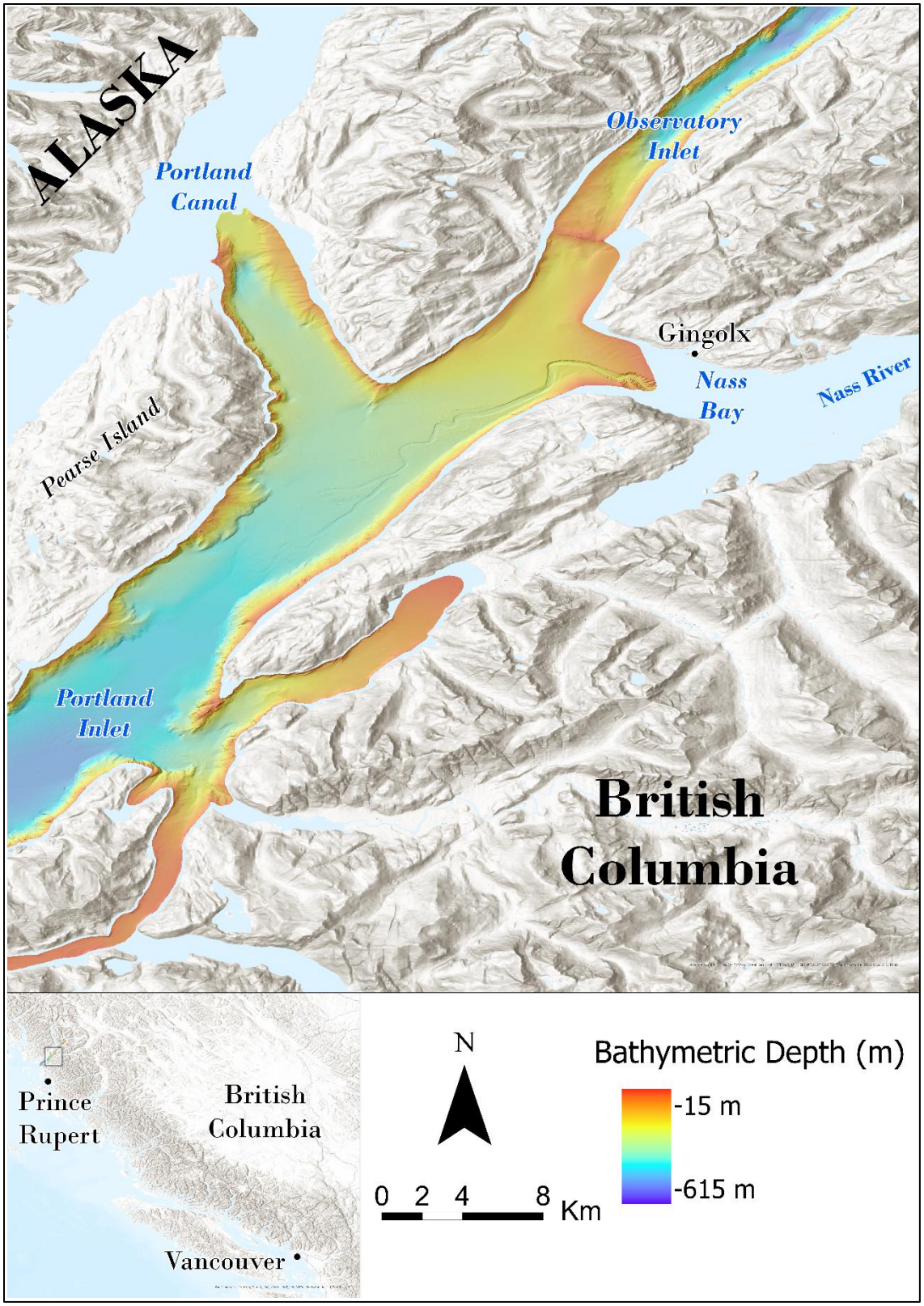

Figure 1: The Nass Delta is located in Nass Bay at the mouth of the Nass River near the town of Gingolx with a submarine channel that extends into Portland Inlet.

Methods

Bathymetric Data Processing

Multibeam Echosounder (MBES) data was collected in September 2020, October 2021 and August 2023 on the CCGS Vector by the Canadian Hydrographic Service (CHS) using a Kongsberg EM710 multibeam echosounder. CHS processed the MBES data using CARIS HIPS and SIPS software to extract gridded bathymetric depths. MBES backscatter data, a measure of the ratio of acoustical energy that returns to the MBES sensor versus energy absorbed by the substrate (Hughes Clarke 1994), was extracted by Natural Resources Canada (NRCan) as individual decibel values in floating point GeoTIFF images and converted to gridded format using the QPS Fledermaus suit FMGT module (Robert Kung – personal communication). The MBES bathymetry rasters were then used to calculate values for Slope (in degrees) and Hillshade (at a NW 315° azimuth) using the ESRI ArcGIS Spatial Analyst toolbox.

Bathymetric Change

Bathymetric change between MBES surveys was calculated by taking the difference between bathymetry rasters, where, for two surveys adjacent in time, the raster values of the older survey is subtracted from the raster values of the more recent survey to create a Digital Elevation Model of difference (DoD). This was performed using the Geomorphic Change Detection (GCD) software (Bailey *et al.* 2022), which was also used to apply a fixed minimum level of detection (LoD) threshold to account for error within the MBES bathymetry (Wheaton et al., 2010). The LoD threshold limit was determined by performing change detection from three rectangle shaped polygons with areas ranging from 4.5×10^5 m^2 to 8.8×10^5 m^2 within the survey area where little bathymetric change was expected (Appendix A; Figure). The squares were all located on the

northern side of the Portland Inlet fjord, representing a proximal location adjacent to the Nass Bay Portland Inlet confluence, a mid-system location near the northern distributary channel-lobe transition zone, and one distal that was adjacent to the terminus of the lobe (Appendix A; Figure). The median of the bathymetric difference was computed and was inferred to represent an estimate of the significant error of the two differenced bathymetry surveys, as the errors are approximately distributed around zero (Appendix A; Figure) (Talling *et al.* 2022, Ruffell *et al.* 2024). To err on the conservative side, the highest median value of the three polygons (0.49 m for 2020 to 2021 and 0.55 m for 2021 to 2023) was chosen to be the LoD blanking threshold (Appendix A; Table 9). These thresholds were much higher than what is expected from the background hemipelagic sedimentation rate (see age control section).

Volumetric Difference Mapping

The bathymetric change values with the threshold applied were used to calculate volumetric change in the study area and estimate relative proportions of seabed raising and lowering within and surrounding the channel using the GCD software. Volume calculations were performed on the bathymetric difference maps to quantify the net-change of sediment in the study area using the simple integration of the vertical distance estimated by the DoD multiplied by the cell resolution for each cell (Wheaton *et al.* 2010). Estimations of volumetric error were calculated by a propagation of error (Brasington *et al.* 2003, Wheaton *et al.* 2010):

$$\delta U_{DoD} = \sqrt{((\delta Z_{new})^2 + (\delta Z_{old})^2)} \quad (1)$$

where δU_{DoD} is the propagated error for the DoD, δZ_{new} is the error of the new bathymetric survey, and δZ_{old} is the error of the old bathymetric survey. When using a fixed LoD, both δZ_{new} and δZ_{old} will be equal to the LoD threshold (Wheaton *et al.* 2010). This was then used to calculate the error for the volume of each cell using:

$$\delta V_i = (CR_i)^2 * \delta U_{DoD} \quad (2)$$

where δV_i is the volumetric error for a given raster cell I, CR_i is the cell resolution of raster cell I, and δU_{DoD} is the propagated error (1) (Wheaton *et al.* 2010).

Specific volumetric calculations were also performed on subregions of the area to quantify the partitioning of sediment in different components of the submarine channel system. This included mapping change within the submarine channel, both over the whole length of the channel, at separate reaches, and targeting individual morphological features within the channel such as bedforms and knickpoints. Moreover, the lobe complexes beyond the terminus of the channel were mapped to compare against changes quantified in the channel. Volumetric change from flows that spilled over the bank along the channel were also mapped, including channel terraces and levees, and channel adjacent bedform fields.

Criteria for Seabed Feature Mapping

Seabed features were mapped as polygons or lines using MBES data and derivative products. Hillshaded bathymetry (in map view and two-dimensional profiles) and slope were used to delineate the boundaries of seabed features, where change in bathymetry is the clearest metric of their extent. MBES backscatter was also used when grainsize differences may indicate boundaries of morphological features. This was used for mapping the submarine channel, terraces, knickpoint inflection points, bedform fields, and the lobe complex. Bathymetry differencing maps were used to map features where seabed lowering or raising occurred, but clear boundaries of features were not identifiable in the bathymetry or derivates. This included the submarine channel lobes, or the extents of channel knickpoints. The mapped polygons representing these features were used for segregating specific regions for localized volumetric change analysis.

Morphological Analysis

Morphological features of the submarine channel system were mapped to describe the characteristics and response to turbidity currents. Knickpoint were mapped at the dominant inflection point of gradient change in each of the bathymetry surveys. Knickpoints were differentiated from crescentic bedforms by using these criteria: generally, a larger change in depth (≥2 m, anything below 5 m is considered a weak knickpoint), a gradient of at least 5 degrees, and a sharp inflection point with no obvious stoss side or wavelength (Paull *et al.* 2011, Guiastrennec-Faugas *et al.* 2020, Heijnen *et al.* 2020, Chen *et al.* 2021). The extent of knickpoint zones were estimated using the existing bathymetric difference maps to delineate the boundaries based on spatial patterns of knickpoint erosion and deposition that have been reported in previous studies (Guiastrennec-Faugas *et al.* 2020, Heijnen *et al.* 2020, Chen *et al.* 2021). Bedform fields outside of the channel were examined by extracting longitudinal transects from each surface. These transects were then used to measure the waveheight, wavelength, and geometry of the bedforms.

Often, knickpoints could be tracked to migrate up-channel between bathymetric surveys when assuming they have similar migration rates to knickpoints observed in other submarine channel systems (Guiastrennec-Faugas *et al.* 2020, Heijnen *et al.* 2020, Ruffell *et al.* 2024, Zulkifli *et al.* 2024). For the purpose of this study, knickpoints were assumed to only migrate up-channel, based on the results of previous studies (Guiastrennec-Faugas *et al.* 2020, Heijnen *et al.* 2020, Chen *et al.* 2021). Therefore, any knickpoints not identified in more recent bathymetric surveys are considered to have disappeared, and any knickpoints that appear without a previously identified knickpoint inflection point down-channel are considered to be newly created. To track the migration rates of knickpoints, the distance between knickpoint inflection points that were identifiable between surveys was measured. This was done by measuring from three points along each of the knickpoint

inflection points, one on the channel left, one in the channel center, and one on the channel right, and taking the mean of the three distances to get an average rate of migration between surveys. The yearly migration rate, KP_{YMR} was then calculated using:

$$KP_{YMR} = KP_{SMR} * (\frac{\Delta t_Y}{\Delta t}) \quad (3)$$

where KP_{SMR} was the migration rate (m/year) between bathymetric surveys, Δt was the time in days between bathymetric surveys, and Δt_Y was 365 days/year.

Sediment Cores

Sediment cores were collected in 2021 (Table 1) on the CCGS Vector, at various locations adjacent to the submarine channel and within the Portland Inlet basin. Core 39 and Core 6 were collected over the submarine channel levee on the northern side at the first channel bend and in a bedform field at the mid-reach bends respectively. Core 13 was collected in the distal fjord basin past the lobe complexes. Cores were acquired using a piston coring system with a paired trigger core (that was also used by itself as a gravity core) using 7 cm diameter core liner. The sediment cores were split and logged at the Pacific Geoscience Center sediment lab. Cores were logged for gamma density, p-wave velocity, and low-resolution magnetic susceptibility using a GeoTek LTD. Multi Sensor Core Logger (MSCL) instrument. X-radiographs were acquired to facilitate analysis of internal structure.

Table 2: Sediment Cores collected during 2021 CCGS Vector Cruise, including type, location and length of core. Map location of Portland Inlet cores are shown in Figure 2.

Core ID	Type	Location	Core Depth (cm)	Water Depth (m)
Core 39	Gravity	Proximal Bend	196	189
Core 6	Piston	Mid-Reach Bends	380	280
Core 13	Piston	Distal Ponded Basin	877	431

Core Interpretation and Facies Development

Sedimentological descriptions of cores were based on visual analysis and pinch tests with verification by microscope using sediment samples washed through a 63 µm sieve. Elevated values of magnetic susceptibility, gamma density, and p-wave velocity were used to infer grainsize increases when these changes were not visible to the naked eye. Regions of bioturbation, where visible, were noted based on the presence of mottled sand or other burrow structures visible in the core, in structure visible in the x-ray photography, or in intervals of high noise in MSCL measurement curves. The location of organic and shell material was also noted when discovered.

Turbidite event beds were delineated based on changes in grainsize and structure. Deposits were classified as beds if they were greater than or equal to 1 cm core depth and designated as laminations if smaller. Beds or laminations were described as discontinuous if they were not fully observed across the core thickness but could be discerned at least halfway. If this threshold was not met, then that feature was designated a mottle. Internal laminations were described using x-ray photography when not visible to the naked eye. The upper mud cap interval (Bouma sequence T_e (Bouma 1962)) were differentiated from hemipelagic sedimentation using gamma density and

magnetic susceptibility measurements. Average gamma density measurements were extracted for turbidite event beds and averaged to calculate a mean turbidite density.

Sedimentation Accumulation Rate Model

Radiometric dating was performed to characterize how sedimentation changes throughout Portland Inlet and to calculate return intervals of turbidite event beds. Three cores were selected for radiometric dating at proximal (Core 39), mid-reach (Core 6), and distal (Core 13) positions in relation to the Nass Delta (Figure 2). The proximal and mid-reach cores are adjacent to meander bends in the submarine channel, whereas the distal core is in a distal ponded basin. Sedimentation accumulation rates in the selected cores were modelled using ^{210}Pb, ^{137}Cs, and ^{14}C radioisotopes as geochronometers. The ^{210}Pb and ^{137}Cs methodologies measure bulk radioisotope activities in sampled intervals of hemipelagic sediment and are used to develop an average sediment accumulation rate in the core, whereas the ^{14}C methodology is conducted on samples of shell or organic material and returns an absolute date.

Event-Free Depths

The core depth intervals with visible turbidity current event beds are considered anomalous excursions from this rate as they are inferred to have rapid deposition that is approximately instantaneous on the timescales considered in the model. Their deposit thicknesses are removed to create an event-free depth. A corrected core depth was also created to account for estimated losses and gains of core depth (void space, gas cracks and any extruded material during core collection). The corrected event-free depth is used for the calculation of the sediment accumulation rate.

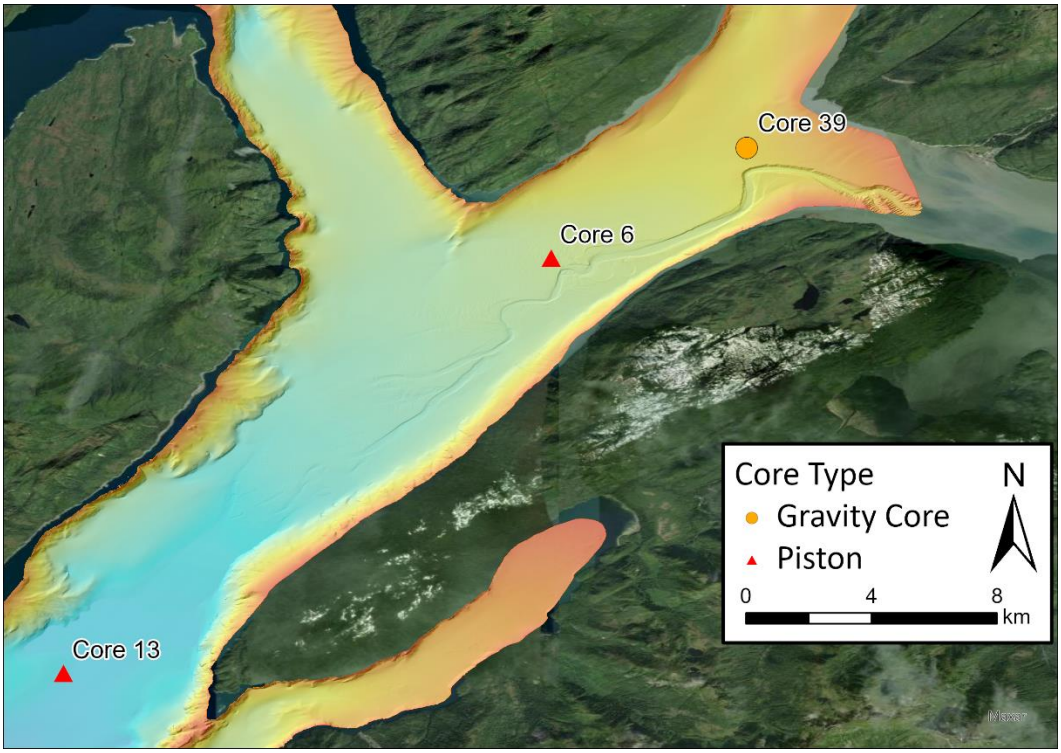

Figure 2: Location of cores collected and logged for sedimentological analysis and radiometric dating. Red triangles denote piston cores, and the orange circle a gravity core.

^{210}Pb Sedimentation Model

The sediment cores were sub-sampled by removing a 2 cm interval of sediment and trimming the sediment in contact with the liner, giving each sample an approximate volume of 8 cm^3 of wet sediment. The samples were collected throughout the upper core depths with tighter sample spacing near the top of the core, and wider spacing at lower core depths. Care was taken while sampling the core to avoid intervals with sandy layers that indicate bioturbation and/or instantaneous sedimentation from turbidite event deposits. ^{210}Pb activity was measured in the hemipelagic sediment where there are two sources for the ^{210}Pb isotopes, the background radioactive decay from the parent ^{226}Ra isotope (as part of the ^{238}U decay series), and the excess ^{210}Pb activity that originated from atmospheric interactions (Robbins 1978). Radioisotope analysis was conducted by Flett Research Ltd. Laboratories using Alpha spectrometry to measure ^{210}Pb activities (Appendix B; Table 10, Table 13, Table 16). Measurements of ^{226}Ra activity were performed

on select samples to develop a background ^{226}Ra activity rate which can be used as a proxy for background ^{210}Pb activity (Appendix B; Table 11, Table 14, Table 17).

The sedimentation models were developed using the slope of the declining excess ^{210}Pb activity curve. First, the background activity was determined by either calculating the average of ^{210}Pb activity values after the slope had flattened, or, if this depth was not reached, by using the average ^{226}Ra background rate. The background activity was then subtracted from the measured ^{210}Pb activity in each sample to calculate the excess ^{210}Pb activities (Appendix B; Table 10, Table 13, Table 16) (Robbins 1978). Then a linear regression was computed with the natural logarithm of this difference and core depth (using the event-free depth when possible) (Appendix B; Figure 23, Figure 24, Figure 27, Figure 28, and Figure 31) (Robbins, 1978). Finally, the decay constant of ^{210}Pb was divided by the slope of the regression line to calculate the velocity of the sediment accumulation rate (Robbins, 1978).

The linear regression was performed on all samples above where ^{210}Pb reached background rates (as indicated by the activity curve flatlining) to give the inclusive sedimentation rate. In cores where the top intervals were observed to have the highest noise due to mixing, these samples were removed from the linear regression to calculate the exclusive sedimentation rate. This sedimentation rate is inferred to be constant throughout the core depth up to approximately 150 years prior to analysis (or 74 years BP) in the absence of mixing. At depths below 74 years BP, the model was considered to be no longer reliable due to the short half-life of ^{210}Pb.

Measurements of ^{137}Cs activity were used as an independent geochronometer to verify the accuracy of the sediment accumulation rate developed by the ^{210}Pb methodology. ^{137}Cs activity measurements were performed on select samples to identify the 1964 ^{137}Cs peak caused by the cessation of nuclear weapons testing which removed the atmospheric source (Ritchie and McHenry

1990). The identification of this peak gave an approximate absolute date within the sediments to compare with the sediment accumulation rate calculated using the ^{210}Pb methodology.

^{14}C Dating

^{14}C dating was performed on Core 13 as an additional geochronometer. Seven samples were collected from the core, which comprised of either shell material ($CaCO_3$) or woody material (conifer needles, small branches, wood fragments, bark fragments etc.). The ^{14}C samples were analysed using Accelerated Mass Spectrometry by the Keck Carbon Cycle Mass Spectrometer (KCCAMS) laboratory at University of California, Irving and at the Beta Analytics Ltd. Radiocarbon Dating laboratory. The raw ^{14}C ages were then calibrated using the Intcal20 curve for terrestrially derived samples (woody material and other organic carbon material) and the Marine20 curve for the carbonate samples (shells and shell fragments) using a $\Delta R = 139.41 \pm 101.42$ to account for the marine reservoir effect based on the Schmuck *et al.* (2021) Northwest Coast Synthesis of North America weighted mean ΔR value. The modelled ^{14}C dates were computed using a Markov Chain Monte Carlo (MCMC) model in the software package OxCal (v4.4.4) where the posterior probability densities were calculated based on the highest statistical likelihood (Bronk Ramsey 2008). A Poisson process (P_Sequence) depositional model was used, where deposition is assumed to be random but proportional to depth (Bronk Ramsey 2008).

Age-Depth Model and Event-Bed Dating

The ^{210}Pb sediment accumulation rates were projected on to the event-free core depth to create an age-depth model for each of the sediment cores. Relying on the assumption that there was not sufficient mixing, the age-depth model was used to assign an approximate age to specific event beds up to approximately 150 years prior to analysis (or 74 years BP). In the distal core, the MCMC modelled ^{14}C dates were combined with the 74 year BP ^{210}Pb date and the 1964 ^{137}Cs date to

generate an age-depth model based on a highest probability density (HPD) range (Bronk Ramsey 2008). Turbidite bed depths were plotted along the HPD range envelopes to calculate an approximate age of each event. The dates of these beds were used to calculate the mean return intervals of event beds.

Nass River Hydrometric Data and Sediment Rating Curve and Nass Bay Tidal Predictions

To test for turbidity current initiation mechanisms, river discharge, climate data and tidal data were gathered from nearby monitoring stations. Sediment flux from the Nass River to the delta was estimated by deriving a sediment rating curve. This value was calculated using Syvitski *et al.* (2000)'s method for estimating sediment concentration, C_s and suspended load, Q_s:

$$C_s = aQ^b \quad (4)$$

$$Q_s = aQ^{b+1} \quad (5)$$

where Q is the mean annual river discharge (m^3), and a and b are empirical parameters which were calculated as:

$$\log(a) = -0.16 - 1.46\log(Q) - 0.00032R + 0.054T \quad (6)$$

$$b = 0.90 - 0.026T + 0.00020R \quad (7)$$

where R is the basin relief (m), and T is the mean annual temperature. Mean annual discharge was calculated from daily discharge data for the Nass River which was obtained from the Environment and Climate Change Canada maintained hydrometric station *Nass River Above Shumal Creek* located near the community of Aiyansh, BC approximately 70 km from the Nass Delta for the period of June 1929 to December 2023 (Water Office: Government of Canada, 2023). Basin relief was

calculated from the highest elevation in the Nass River watershed to the elevation of the hydrometric station (Water Office: Government of Canada, 2023). The mean annual temperature was calculated from climate normals between 1981 and 2010 which were extracted from the Environment and Climate Change Canada Historical Climate Data web site (https://climate.weather.gc.ca/index_e.html) on 2024-11-01 from the *Nass Camp* weather station, which is located 4.4 km from the hydrometric station. Tidal data for Nass Bay was acquired from the Department of Fisheries and Oceans Canada tidal prediction station 09422 Gingolx, BC (https://tides.gc.ca/en/stations/09422) on 2024-10-25. This station was used as there were no tidal monitoring buoys within 120 km of the study site. Hourly predictions of tidal height were extracted for the spring freshet periods of 2020 to 2023.

Results

Submarine Channel System Morphology

The Nass Submarine Channel System was broken down into four distinct morphological regions: (i) the upper channel reaches, which comprised the tributary canyons on the delta front, the canyon-channel transition zone, and the upper channel bend; (ii) the mid-channel reaches, which included the straight reach and the bend dominated reach with bedform fields; (iii) the lower-channel reaches, which comprised the channel fork and the northern and southern distributary channels; and (iv) the lobe complexes and distal ponded basin. In total, the channel was measured to a length of 18 km at the most continuous connection, and 22 km to the length of the most distal activity due to turbidity currents observed in this study.

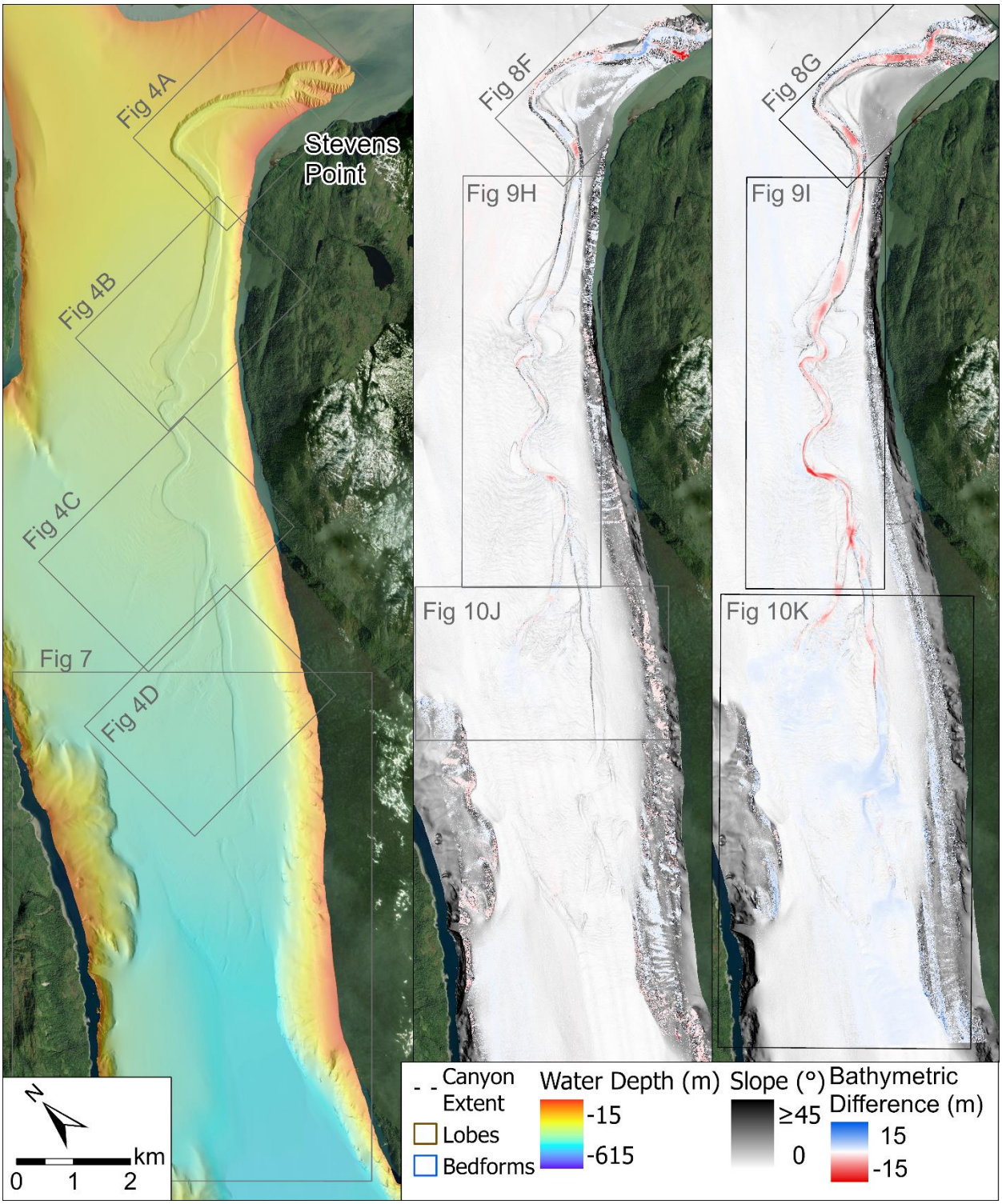

Figure 3: I. Overview map of the submarine channel system with blue polygons denoting the extent of bedform fields, the brown polygon the extent of the lobes and the grey dashed line the extent of the canyon that was not surveyed using high resolution MBES bathymetry. II. and III. Bathymetric difference map outputs showing calculations of deposition (blue) and erosion (red). Between 2020 and 2021 (II) a level of detection threshold of 0.49 m was used, and between 2021 and 2023

(III) a level of detection threshold of 0.55 m was used. Insets of the regions denoted as a) to d) are shown in Figure 4 and Figure 5, and f) to k) in Figure 8, Figure 9 and Figure 10.

Upper Channel Reaches

At the Nass Delta two tributary submarine canyons are incised into the delta front. Here, the delta front was surveyed for MBES high resolution bathymetry up to approximately 30 m water depth, where the canyons were incised to a depth of ~140 m. The larger north canyon was measured to have an area ~1.7 km^2 and extended for ~2 km from the approximate center of the delta front, whereas the smaller southern canyon had a measured area of ~0.3 km^2 and extended for ~ 1km from the southern edge of the delta, approximately 400 m from Stevens Point. Just beyond Stevens Point was the canyon-channel transition zone where the canyons converged into a single channel and extended perpendicular to the delta front for 3.5 km where it curved to the south-west at the confluence of Nass Bay and Portland Inlet. The channel wall relief decreased from 100 m to 30 m along this reach.

In the northern canyon and the upper reaches of the submarine channel, bedform morphologies were common on the channel bed. Trains of crescentic bedforms were the dominant bedform, with typical wave heights of 1 m to 3 m and wavelengths of 50 m near the delta lip and 150 m at the distal end of the canyon, with a downslope asymmetric shape (Figure 4, Figure 6). Three small poorly developed knickpoints were also observed here, but they were often hard to distinguish from crescentic bedforms in this reach. The southern tributary canyon also had crescentic bedforms, up to 2 m in wave height and 20 m in wavelength that were primarily downslope asymmetric. A distinct transition was observed at 4 km from the delta-lip, where crescentic bedforms were less common with smaller wave heights <1 m and inconsistent wavelengths, and knickpoints became the dominant in channel morphology (Figure 4, Figure 5). This corresponded with a slope break transition from 1.8 ° to 0.8 °. At the end of this reach was the largest knickpoint zone (KP 4 and KP 5), which had a relief of 16 m (Figure 5).

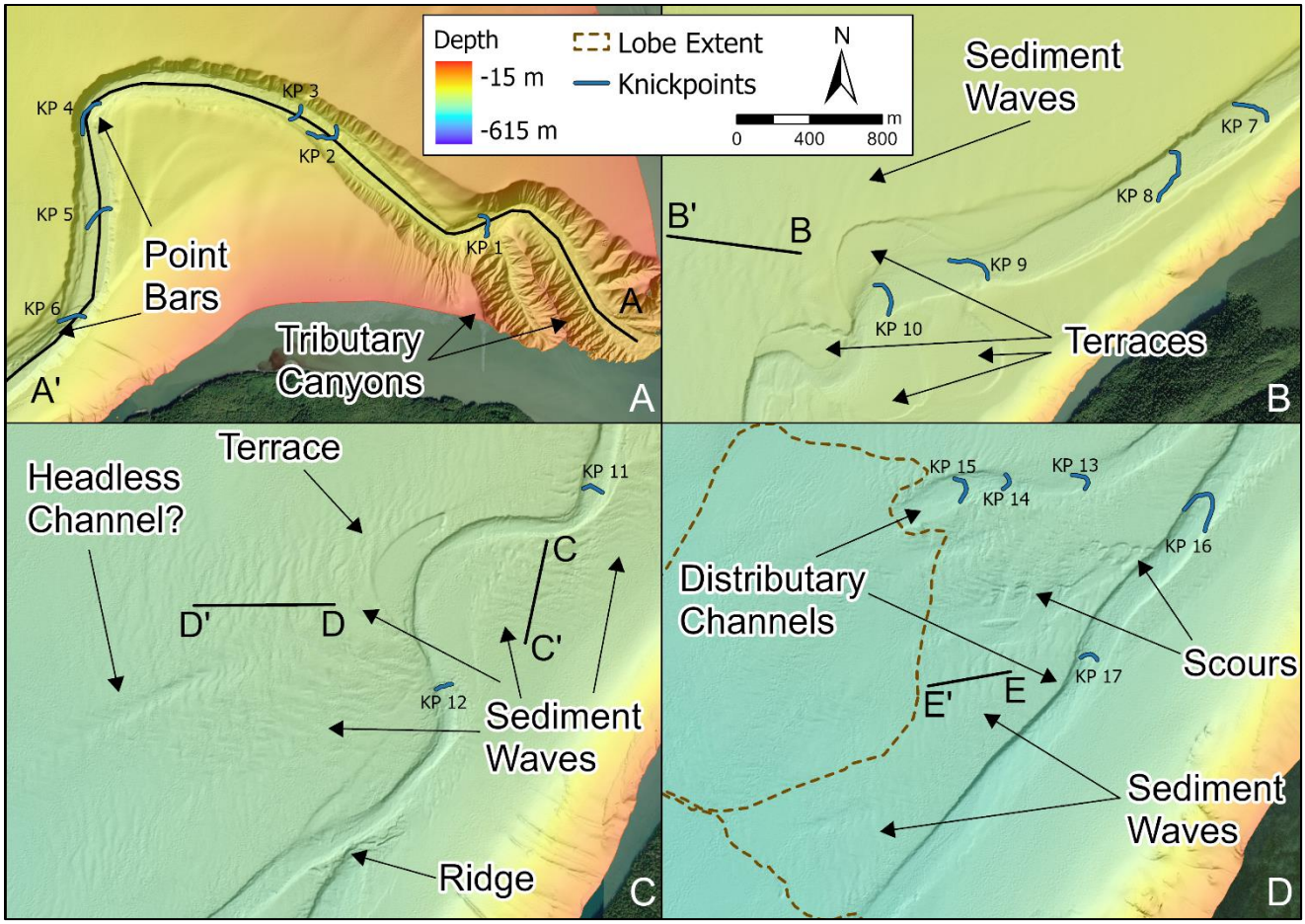

Figure 4: Planview morphology of the channel reaches with the position of knickpoints (KP), that are mapped at their inflection point, denoted in blue lines. Black lines denote the extent of profiles in Figure 5 and Figure 6. The reaches are shown as follows: a) The northern and southern tributary canyon, the canyon transition zone and the first channel bend; b) and c) the midchannel reaches including the straight reach and the bend dominated reach and the channel fork; d) The northern and southern distributary channels.

Mid-Channel Reaches

The following reach of the channel had an average gradient of ~0.5 ° which remained approximately constant for the rest of the channel length. This was shallower than the seafloor gradient in the fjord which was measured to have an average of 0.8 °. The first component of this reach was straight for ~2.3 km. Along this distance, the channel wall relief decreased from 30 m to 15 m. Two poorly developed knickpoints were observed in the channel (KP 7 and KP 8), and a bedform field of sand waves with crest heights of 1 m and wavelengths of 50 m were observed on the levee and fjord

floor up to 700 m from the northern side of the channel, with an upslope asymmetric shape (Cartigny *et al.* 2011).

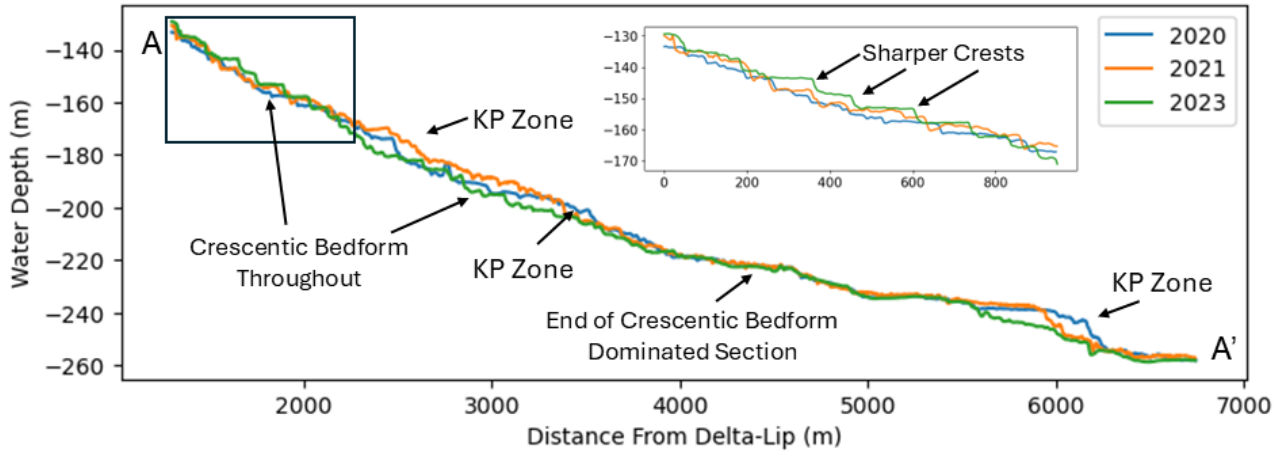

Figure 5: Profile view of northern canyon and upper channel (Figure 4). Crescentic bedforms are the dominant in-channel bedform with some knickpoints that eventually give way to just knickpoints (shown as knickpoint (KP) zones, which represents one or more inflection points). Crescentic bedforms in the upper canyon (inset profile) had the sharpest inflection points and most clearly defined shape in the 2023 survey.

Following this the channel comprised a series of six tight bends, with an in channel curvilinear length of ~4.7 km over 3.5 km of the fjord floor basin length giving a sinuosity coefficient of ~1.3. At the transition between the straight reach and the channel bends was a knickpoint zone (KP 9 and KP 10), and two other knickpoint zones were observed within the channel bends (KP 11 and KP 12). Through this reach, the channel wall relief ranged from 7 m to 15 m. Bedform fields were observed on the seafloor in the fjord adjacent to the bends up to ~1.6 km from the channel levee on the north side of the channel and up to 1 km from the south side of the channel where they are constrained by the fjord sidewall (Figure 3, Figure 4). The crests of these bedforms have a general trend of orientation perpendicular to channel meander bends, often extending radially around a channel as it curves (Figure 3, Figure 4). In the more proximal region of this reach the bedforms had wave heights of 2 m with wavelengths between 75 m to 150 m. At the more distal bends, the wave heights were similar, but wavelength decreased to typically 50 m to 100 m. The profile shape of the sediment waves was predominantly upslope asymmetric (Cartigny *et al.* 2011). Here on the

northern side of the channel a 900 m long and 80 m wide linear scour is observed with crescentic bedforms within that may be a headless channel, located 1 km from the channel bend apex (Figure 4).

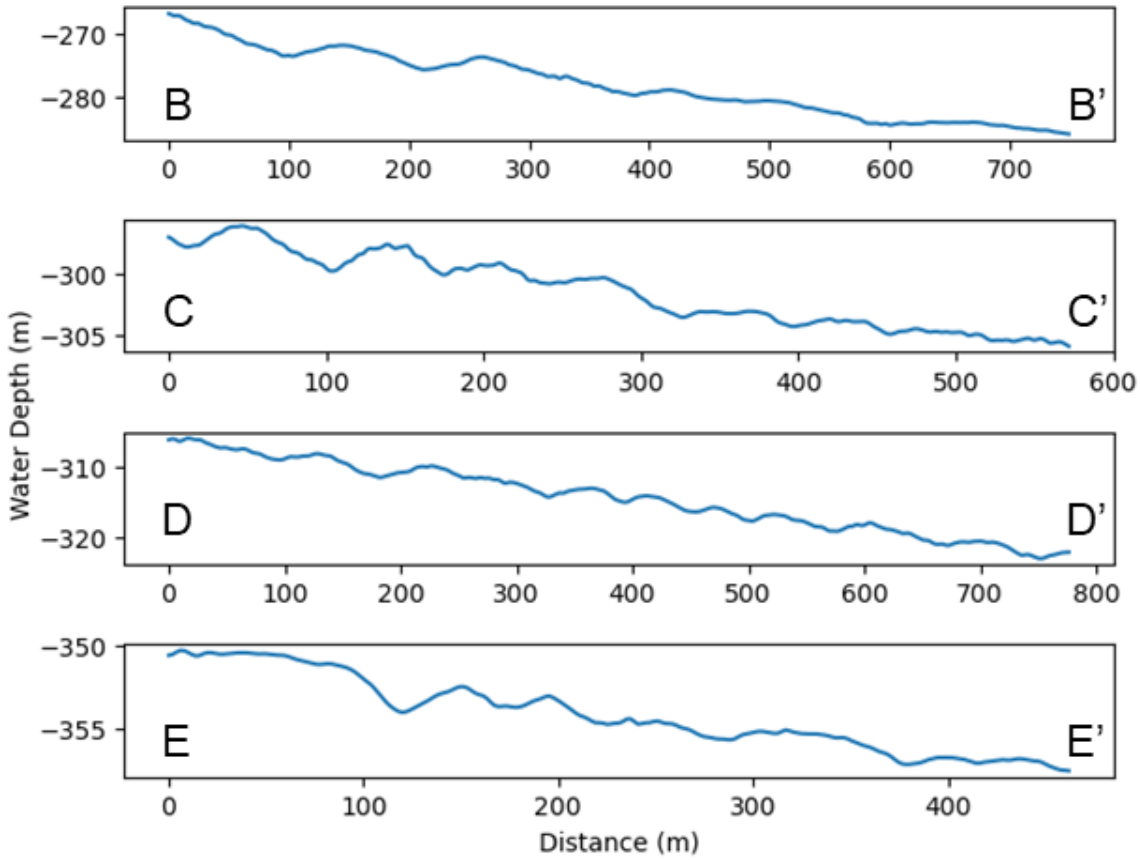

Figure 6: Representative bathymetric profiles from bedform fields at different reaches of the channel. B-B', C-C', and D-D' were from the channel bends reach, E-E' was from the southern distributary channel (Figure 4)

Channel Fork and Distributary Channels

In the next reach, the submarine channel forks forming two distributary channels, indicating a previous channel avulsion event. In the 2020 and 2021 bathymetric surveys, the southern channel had a ridge that was perpendicular across the channel at the channel fork that rose 5 m above the channel thalweg (Figure 4). In the 2023 bathymetric survey, this ridge had disappeared. The northern distributary channel had two knickpoint zones (KP 13, KP 14, and KP 15), and the southern

distributary channel had two knickpoint zones (KP 16 and KP 17) and had crescentic bedforms within 600 m down-channel of the ridge. In these reaches, channel bank relief varied from 4 m to 10 m. Sediment waves were present on both sides of the northern distributary channel and on the northern side of the southern distributary channel which abutted the lobe complexes, with typical crest heights of 0.5 m, wavelengths of 25 m to 50 m, and upslope asymmetry. Moreover, in the region between the distributary channels were eight crescentic shaped scours with scarp lengths between 45 m to 150 m and heights between 3 m to 7 m (Figure 4).

Lobe Complexes and Distal Ponded Basin

At the terminus of the northern distributary channel a fan shaped lobe was mapped with an area of 2.9 km^2. Sediment waves were the dominant bedform observed with wave heights of 0.5 m and wavelengths of 25 m, and an upslope asymmetry. The southern distributary channel has an extensive lobe complex at with a total area of 7.3 km^2. Here, the morphology was complex, which included sediment waves with wave heights of up to 1 m, typical wavelengths of 25 m and an upslope asymmetry, eight headless distributary channels, and numerous crescentic shaped scours between 2.5 m to 4 m that were located either inside the headless channels (that may be knickpoints) or unattached to any channel. Beyond the lobe complexes, a ponded basin was observed, where the average gradient decreased to 0.01 °. The ponded basin continued down the length of the fjord, with minor bathymetric variations that were interpreted to be due to current scouring and sediment from small streams draining into the fjord.

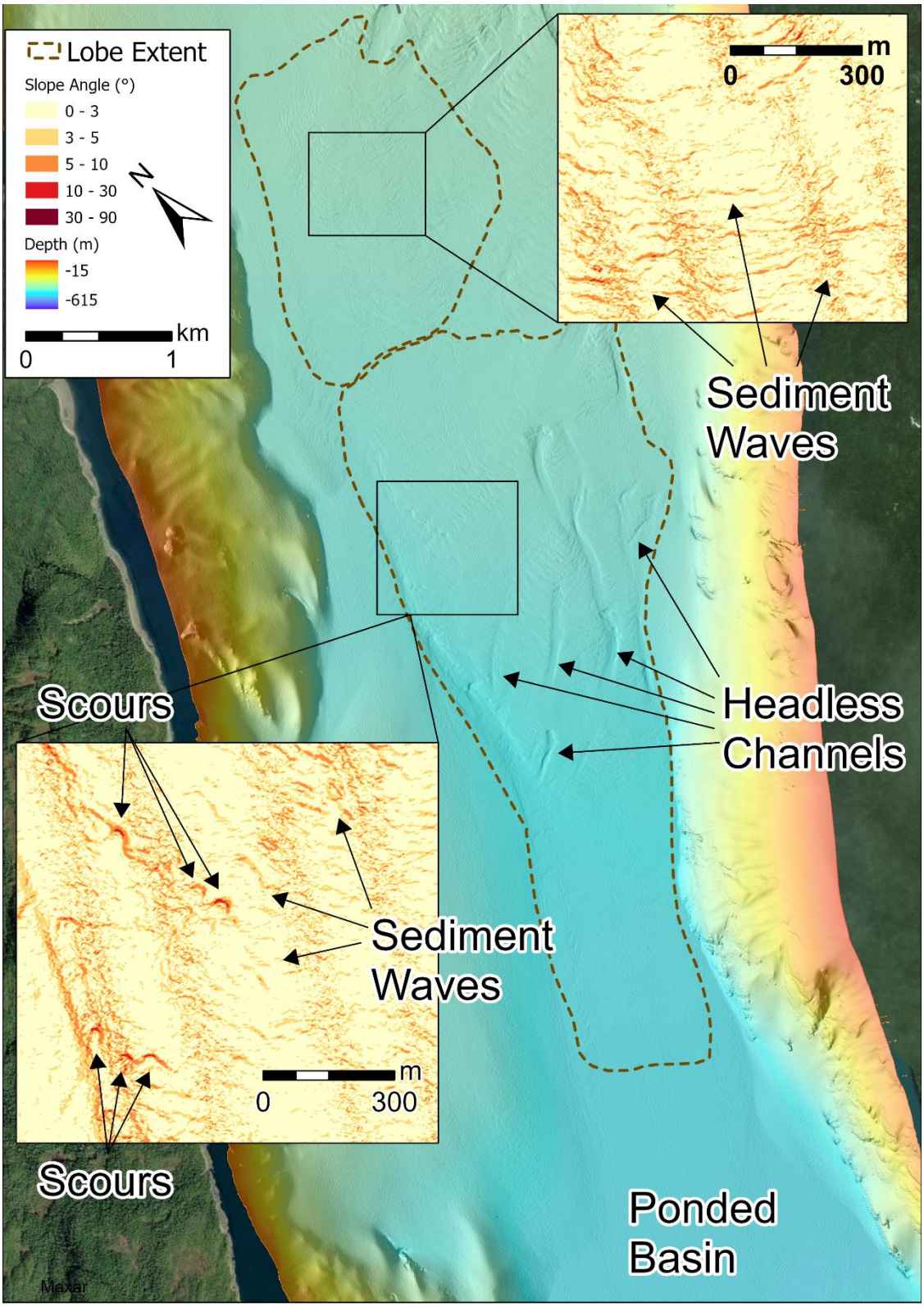

Figure 7: Morphology of the lobes shown in MBES bathymetry. Inset maps show slope maps where sediment wave bedforms are present on both lobe complexes and that crescentic scours were observed on the southern lobe.

Difference Mapping and Volumetric Change

Bathymetric difference maps were created for between the 2020-2021 survey interval and the 2021-2023 survey interval (Figure 3). Positive bathymetric change was assumed to represent the deposition of sediment and negative bathymetric change was assumed to represent areas experiencing of erosion. Volumetric changes were calculated at the scale of the channel system to quantify change within the submarine channel and outside of the submarine channel, which was divided into the lobe complexes, the channel terraces, and the channel adjacent bedform fields. Bathymetric differencing of the channel was further segmented to quantify the change in the canyons, knickpoint zones, channel bends, and generalized change in the channel thalweg for channel deposition and erosion unrelated to specific channel morphology (Ruffell et al. 2024). The volumetric change results are presented in Table 3 and Figure 11. The distal ponded basin was not resurveyed after 2020 and is excluded from this analysis. Volumes of surficial change were converted to mass using a mean turbidite density of 2180 kg m^3 (Table 3; Appendix C).

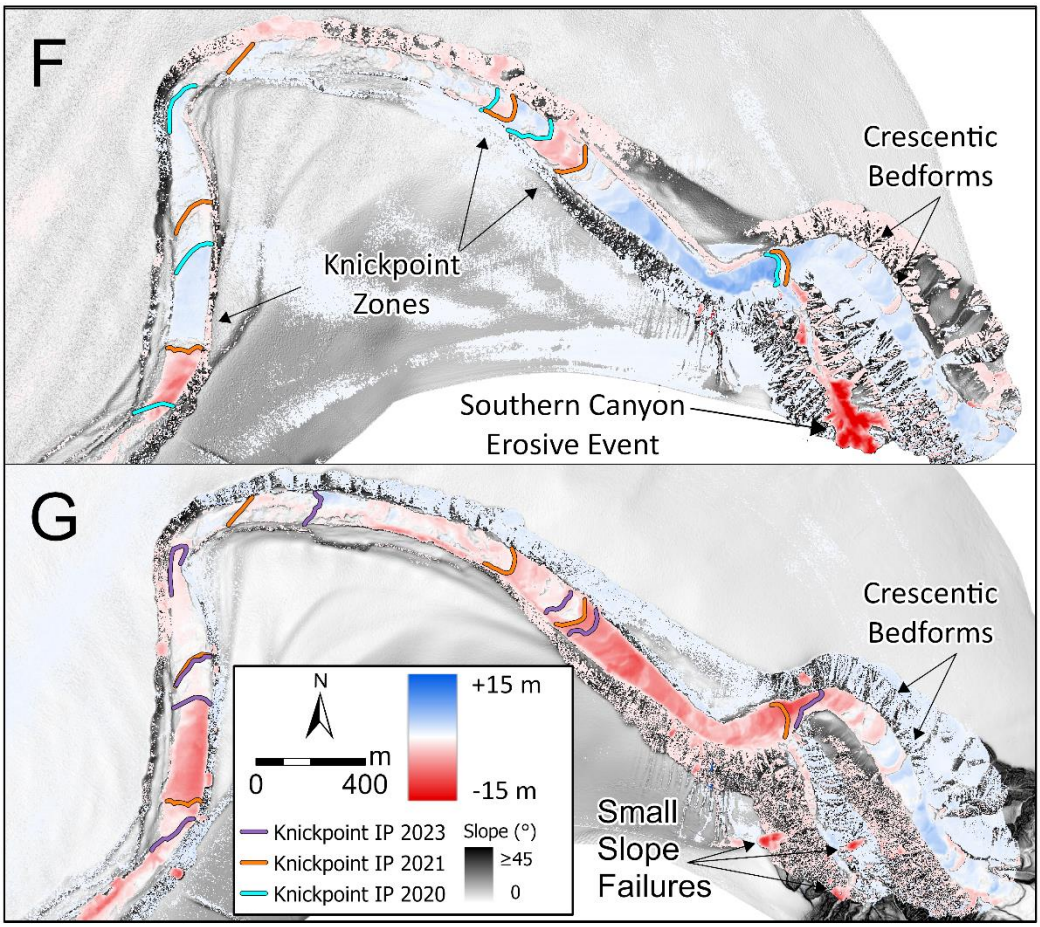

Figure 8: Bathymetric difference maps (Figure 3) of the canyons and upper reaches of the channel between 2020 and 2021 (f) and 2021 and 2023 (g) where deposition is shown in (blue) and erosion in (red), and the position of knickpoint inflection points (IP) which are observed to migrate up-channel between bathymetric survey intervals. The regions showing bathymetric change have similar extents but where between 2020 and 2021 there was erosion and deposition visible whereas between 2021 and 2023 there was predominantly erosion beyond the canyons.

Channel-System Scale

The 2020-2021 difference map shows surficial change along most of the length of the channel, with visible deposition in the bedform fields and the northern lobe (Figure 3, Figure 9, Figure 10). Volumetrically, the channel experienced the most amount of localized volumetric change but was in an approximate overall balance between deposition and erosion (Figure 11). Both the northern lobe and bedform fields were dominated by deposition, contributing 13% and 20% of the total deposition in the channel system (Figure 11, Table 3). Deposition at the northern lobe was spread out in a fan shape, whereas the deposition in the bedform fields was primarily infill in the bedform

troughs. Resolvable deposition was limited to the channel proximal regions of the lobe and bedform field compared to the full extent of these features (Figure 3, Figure 9, Figure 10). Volumetric change on the channel terraces was negligible and within the threshold of error. The overall net volumetric change is within the threshold of error and can therefore be considered approximately in equilibrium.

Table 3: Volumes of surficial change calculated for the submarine channel system converted to yearly change. Volumes were converted to mass using a mean turbidite density of 2150 kg m^3.

Location	2020-2021			2020-2021		
	Net Volume Change (m^3/year)	Error (m^3/year)	Mass of Sediment Change (kg/year)	Net Volume Change (m^3/year)	Error (m^3/year)	Mass of Sediment Change (kg/year)
Channel	9.3×10^4	7.0×10^5	2.0×10^8	-1.7×10^6	6.1×10^5	-3.7×10^9
Lobe	2.6×10^5	1.8×10^5	5.6×10^8	3.7×10^6	2.1×10^6	8.0×10^9
Terraces	4.4×10^4	3.3×10^4	9.4×10^7	1.4×10^4	1.1×10^4	3.0×10^7
Bedform Fields	2.8×10^5	3.6×10^5	6.1×10^8	1.3×10^6	1.1×10^6	2.8×10^9

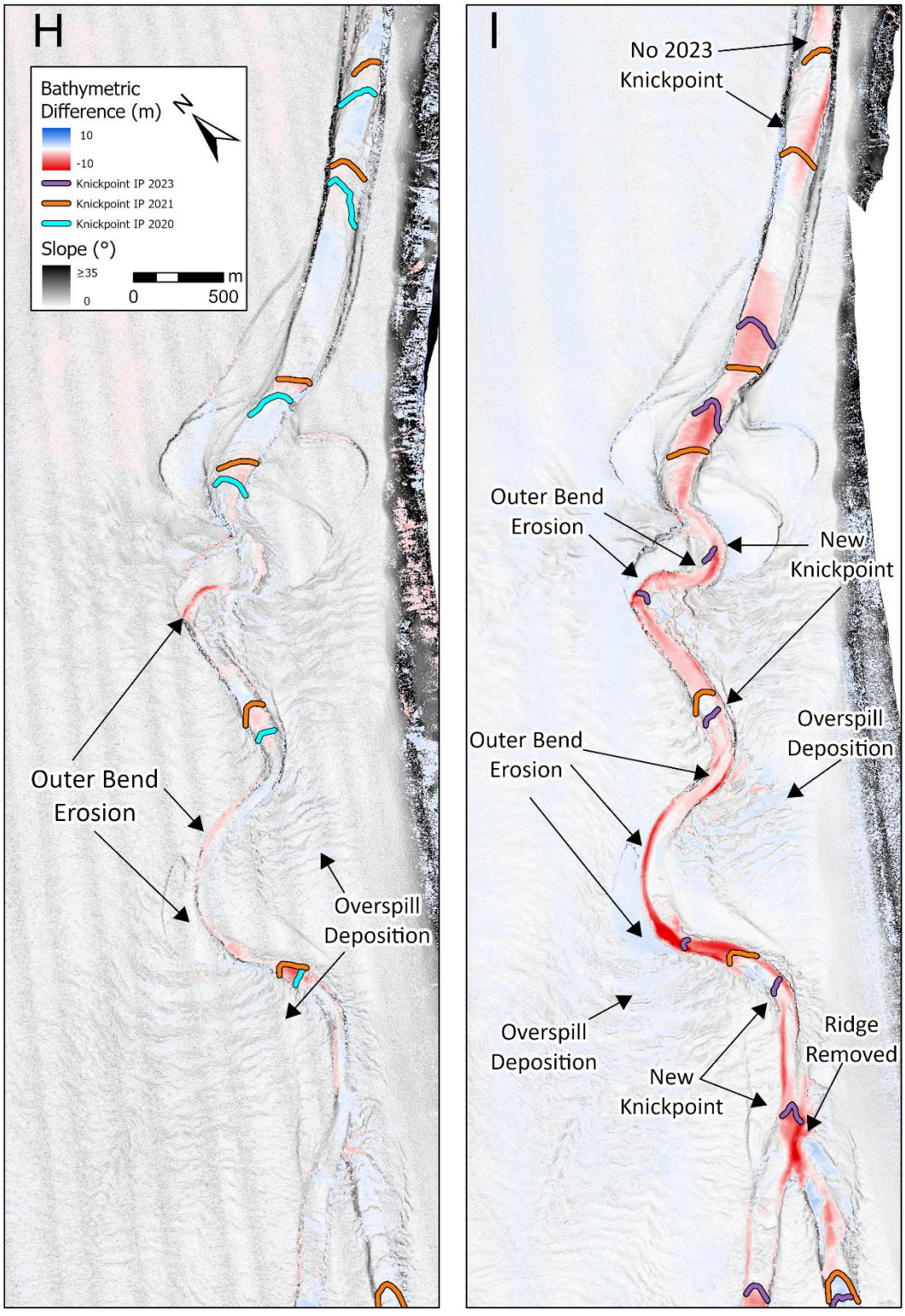

Figure 9: Bathymetric difference map of the mid-channel reaches and channel fork between 2020 and 2021 (j) and 2021 and 2023 (k) where deposition is shown in (blue) and erosion in (red), and the position of knickpoints. Between 2021 and 2023 the magnitude of erosion is overall much higher within the channel and more overspill deposition is visible in the bedform fields.

The 2021-2023 survey shows the channel was dominated by erosion in this time interval (Figure 3, Figure 8, Figure 9, Figure 11). Moreover, the ridge that separated the southern distributary channel disappeared, and deposition and erosion was observed in this reach (Figure 3, Figure 9). The lobe complex was the predominant region of deposition comprising of 58% of the total deposition, followed by the bedform fields which comprised 27% of the total deposition (Table 3). Deposition in the bedform fields was predominantly infill between the sediment wave crests that was observed up to 2 km from the channel (Figure 9). The northern distributary lobe showed a larger spatial extent of deposition compared to the 2020-2021 survey interval, with a set of rills that extend radially from the channel-lobe transition (Figure 10). The southern distributary channel lobe complexes showed extensive depositional change where none had been observed during the 2020-2021 survey interval (Figure 10). Although deposition was observed over most of the lobe complex, the largest deposits were clustered into three lobe regions and had localized concentrations of deposition within the headless channels and in sand wave troughs (Figure 10). Here the deposition abutted against the lower limit of the survey area indicating that deposition may continue down basin, which is not fully captured in this analysis (Figure 3, Figure 10). Erosion in the lobe was confined to scour features which were observed to deepen by up to 2 m, and, in certain instances inside the headless channels, migrate up-channel which indicates that they may be knickpoints (Figure 10). Volumetric change on the terrace was negligible when compared to all other channel system components (Table 3; Figure 11). Overall, there was net-deposition within the resurveyed components of the channel system.

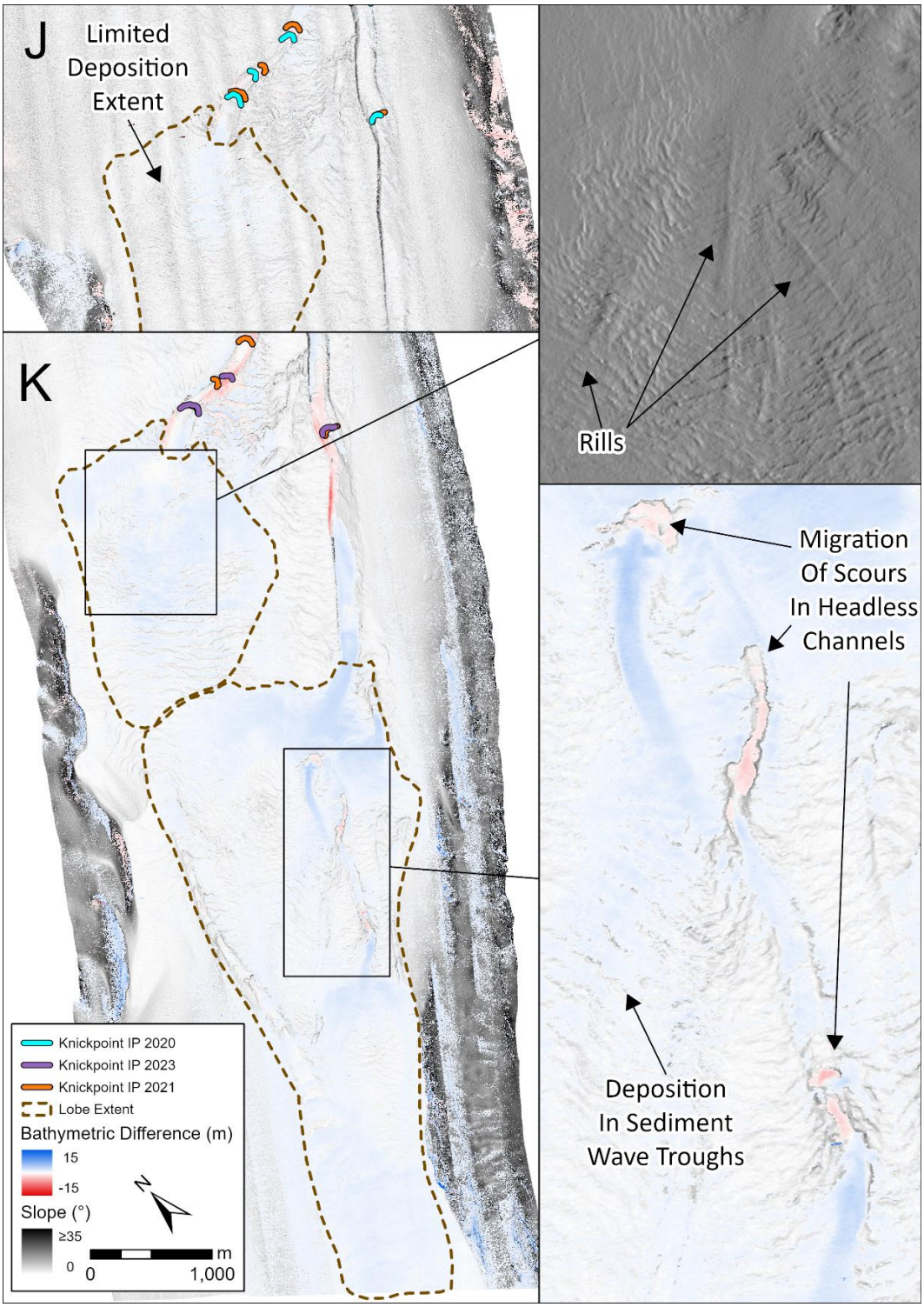

Figure 10: Bathymetric difference map of the lobe between 2020 and 2021 (j) and 2021 and 2023 (k) where deposition is shown in (blue) and erosion in (red), and the position of knickpoints. The upper inset shows the formation of rills in the northern lobe complex in 2023 (overlaying Hillshade at 315 azimuth). The lower inset shows the dominant headless channels in the southern lobe (only active between 2021 and 2023) where certain scours appear to migrate up-channel indicating they may be knickpoints.

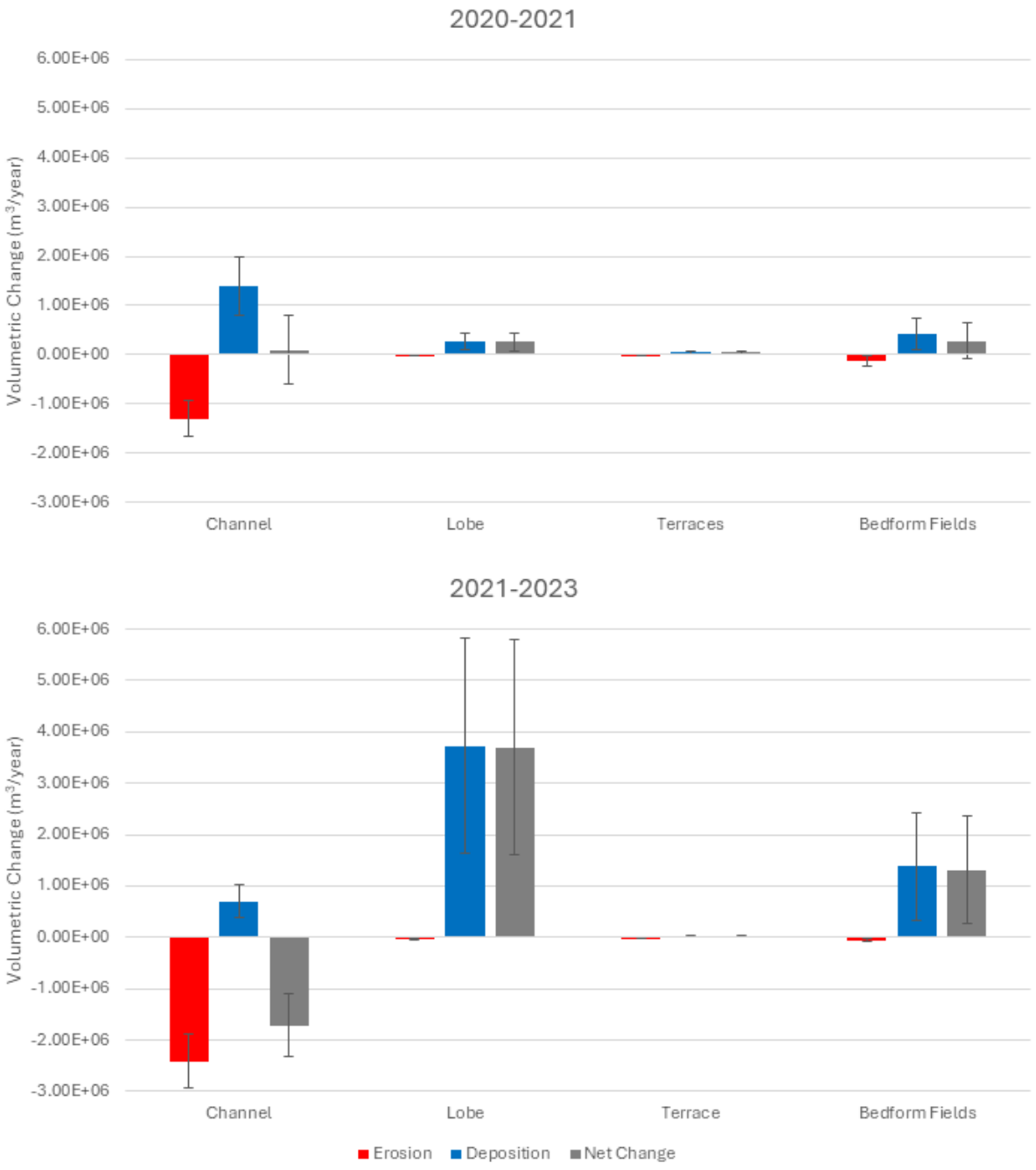

Figure 11: Calculated volumes of bathymetric change for the submarine channel system between 2020 and 2021 (top) and 2021 and 2023 (bottom) scaled to a yearly rate. The bars represent the sum of all pixel cells multiplied by the channel resolution in each sub-region of the submarine channel system, with the red bars representing the negative pixel cells (erosion), the blue bars the positive pixel cells (deposition) and the green bars the net difference.

In-Channel Volumetric and Morphological Change

Change observed within the channel was broken down to four components: change within the distributary canyons, change associated with knickpoints, change in the channel banks (from mass wasting, outer bend erosion, and inner bend deposition), and general thalweg change. The volumetric change estimated for each of these components are presented in Figure 12. The spatial distribution of this volumetric change is further described along different reaches of the submarine channel.

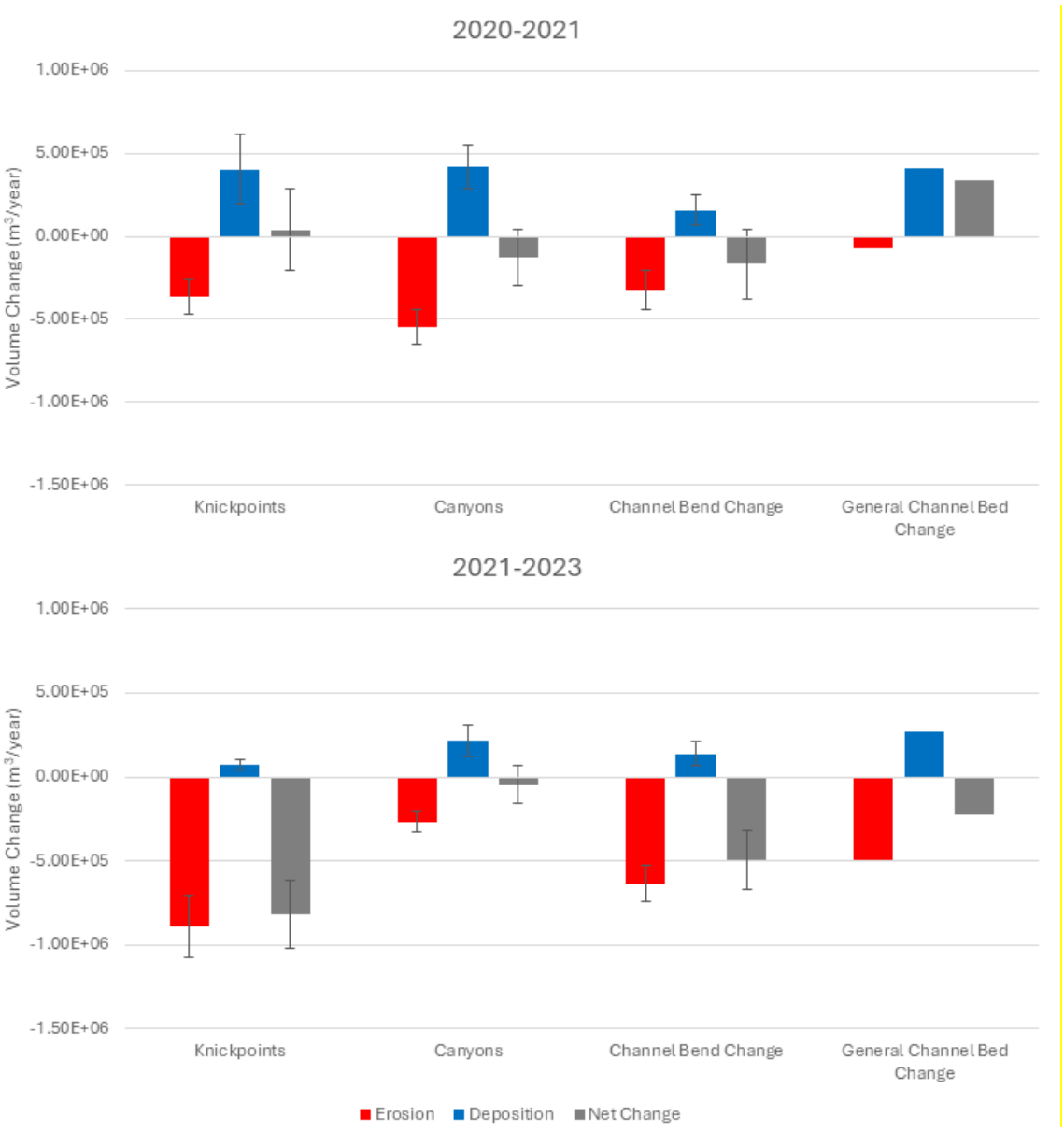

Figure 12: Calculated volumes of bathymetric change from different channel components between 2020 and 2021 (top) and 2021 and 2023 (bottom) scaled to a yearly rate. The bars represent the sum of all pixel cells multiplied by the channel resolution in each sub-region of the submarine channel system, with the red bars representing the negative pixel cells (erosion), the blue bars the positive pixel cells (deposition) and the green bars the net difference.

Change Within the Tributary Canyons

Both the tributary canyons showed extensive volumetric change between 2020 and 2021. The northern tributary canyon shows primarily deposition on the canyon floor with some erosion around crescentic bedforms, with minimal resolvable change on canyon walls that may be induced

from error in the MBES surveys. The bedforms with larger wave heights and wavelengths in 2020 showed up-channel migration in 2021, whereas the less developed bedforms showed aggradation, growing both in wave height and wavelength (Figure 5). The southern canyon experienced a large erosive event which was concentrated at the delta-proximal limit of the bathymetric survey and caused erosion up to 25 m into the canyon floor and walls and increased the average width of the canyon floor from 15 m to 25 m (Figure 8). In total, this erosion comprised 68% of the total erosion shown in the canyons.

In 2021 to 2023 deposition and erosion in the canyon was approximately in balance (Figure 12). In the northern tributary canyon, crescentic bedforms had alternating patterns of erosion from upslope migration and deposition from aggregation (Figure 8). The profile of the bedforms show that the bedform crests became more distinct and the overall shape more uniform with downslope asymmetry (Figure 5). In the southern tributary canyon, two slope failures were observed (Figure 8) which comprised 43 % of the total erosion observed at this location.

Change Related to Knickpoints

Between 2020 and 2021, knickpoints were active centers of volumetric change. In the upper and mid-reaches of the channel, knickpoints showed comparatively large erosion and deposition but with little overall net change (with the exception of KPZ 1 in the northern tributary canyon and in KPZ 4 in the straight reach which were both dominated by deposition) (Figure 8, Figure 9, Figure 13). The relative proportion of change related to knickpoints had an overall decreasing trend with distance along the channel (Figure 13). All knickpoints showed up-channel migration with a range of migration rates from 31 m/year to 234 m /year, apart from KP 10 and KP 11 in the southern distributary channel where no movement was observed (Table 4).

Between 2021 and 2023 knickpoint zones were predominantly erosive. Knickpoint erosion was highest at the proximal reaches of the channel with a decreasing proportion of erosion with distance along the channel (Figure 13). Erosion distribution around knickpoint zones was a combination of up-channel migration and channel bed erosion down-channel from the knickpoints where deposition was previously observed between 2020 and 2021. Twelve knickpoints showed up-channel migration with a range of migration rates from 10 m/year to 371 m/year (Table 4). One knickpoint in the northern distributary channel was observed to show no movement, (Table 4). Three of the knickpoints identified in the 2021 survey were not observed in the 2023 survey (KP 7, KP 8, and KP 16; Table 4). Moreover, seven further knickpoints were identified that did not correspond to any previously identified knickpoints down-channel indicating that they may be newly formed knickpoints (KP i to KP vii; Table 4).

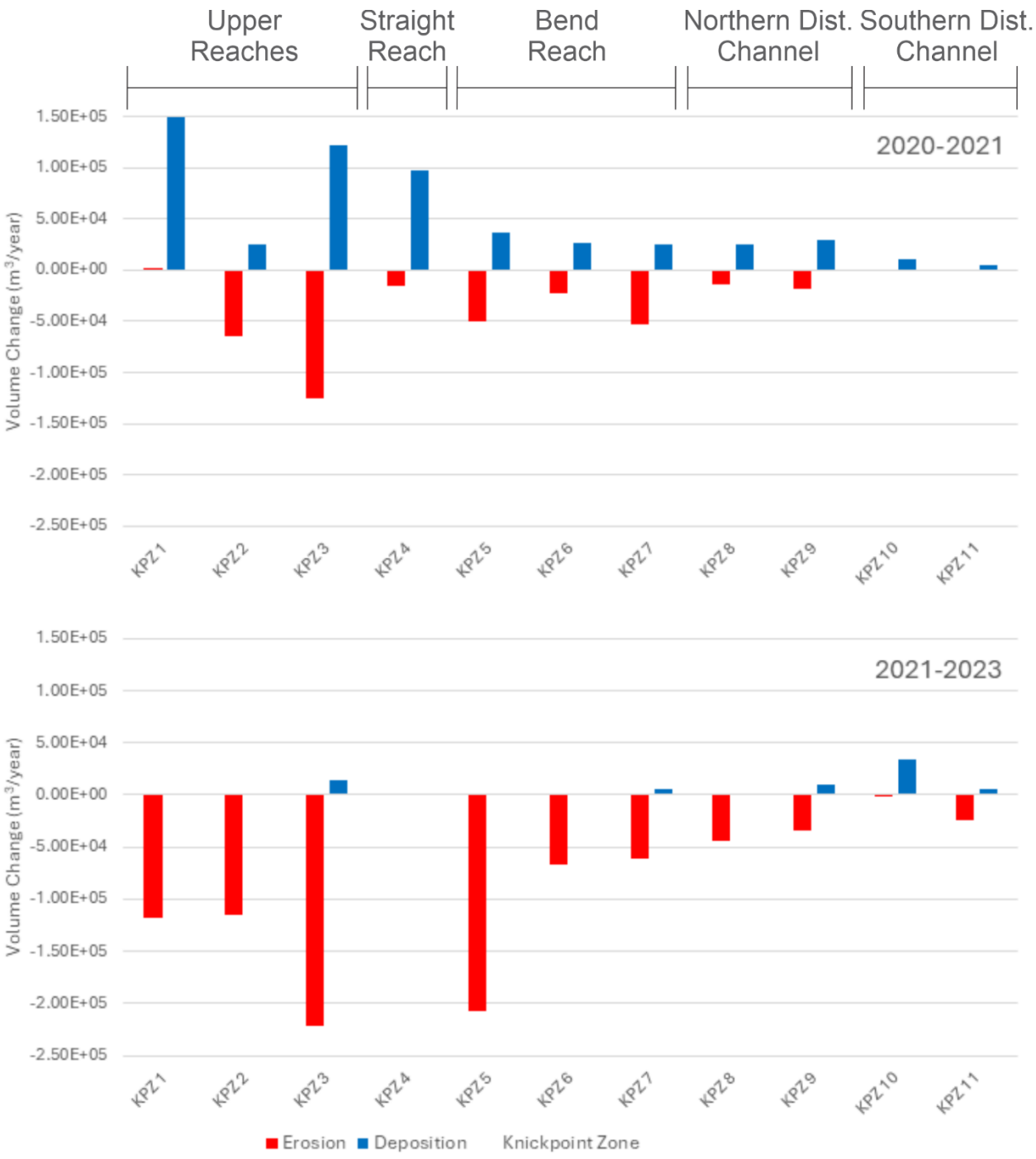

Figure 13: Volumetric change in each knickpoint zone (KPZ) between 2020 and 2021 (top) and 2021 and 2023 (bottom) scaled to a yearly rate. The bars represent the sum of all pixel cells multiplied by the channel resolution in each sub-region of the submarine channel system with the red bars representing the negative pixel cells (erosion) and the blue bars the positive pixel cells (deposition). KPZ 4 shows no volumetric change between 2021 and 2023 as the knickpoints here had disappeared and the resulting change could not be attributed to knickpoint movement.

Notably, all the newly identified knickpoints appeared at channel bends, often at or just after a constriction point (Figure 14). Moreover, several knickpoint inflection points identified in the 2023 survey appeared in approximately the same position as previous knickpoint inflection points identified in either the 2020 or 2021 surveys. The KP 5 and KP 6 knickpoint inflection points migrated to the positions of the KP 4 and KP 5 knickpoint inflection points in the 2020 survey (Table 4; Figure 10). KP i, a newly formed knickpoint appeared at the position of the KP 5 knickpoint inflection point in 2021 (Table 4; Figure 14). KP v appeared down-channel from the position of KP 16, the first knickpoint at the southern distributary channel, which appeared to be infilled by deposition and was the only knickpoint zone which experienced net deposition (Figure 13).

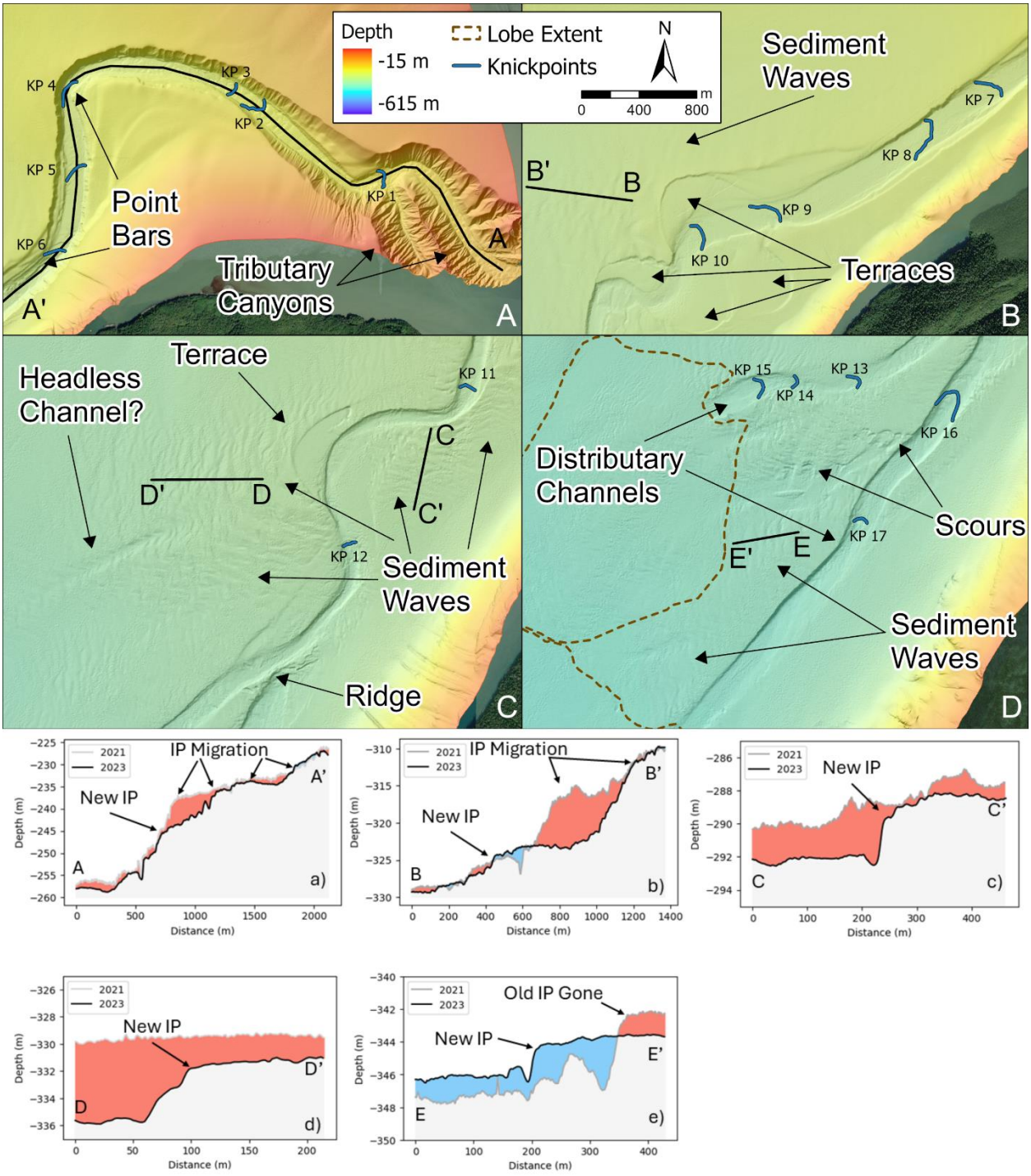

Figure 14: Newly created knickpoints a) to e) between 2021 and 2023 with their mapped knickpoint inflection point (IP) in planview (top) and two-dimensional profiles (bottom) where red represents erosion and blue deposition. In a) to c) the new knickpoints were created in channel bends, whereas d) and c) occurred up- and down-channel (respectively) from where the ridge at the channel fork was located. In a) knickpoint inflection points in the 2023 bathymetric survey were observed to either appear or migrate to the position of previously mapped knickpoint inflection points in 2020 or 2021. In b) to e) the new knickpoints had a low relief of between 2 m to 4 m.

Table 4: Knickpoint migration rates between the 2020-2021 bathymetric surveys and the 2021-2023 bathymetric surveys. Knickpoints denoted with an Arabic numeral were observed in 2020 and 2021, and those denoted with a Roman numeral were only observed in 2023.

Knickpoint ID	2020-2021		2021-2023	
	Migration between survey intervals (m)	Average Velocity per Year (m/yr)	Migration between survey intervals (m)	Average Velocity per Year (m/yr)
KP 1	32	31	114	65
KP 2	168	163	50	29
KP 3	81	78	226	128
KP 4	238	231	264	150
KP 5	142	138	379	215
KP i	-	-	-	-
KP 6	241	234	376	214
KP 7	160	155	-	-
KP 8	120	116	-	-
KP 9	120	116	247	140
KP 10	113	110	253	144
KP 11	166	161	653	371
KP ii	-	-	-	-
KP 12	101	98	268	152
KP iii	-	-	-	-
KP iv	-	-	-	-
KP 13	98	95	258	147
KP 14	97	94	101	58
KP 15	52	50	0	0
KP 16	0	0	-	-
KP v	-	-	-	-
KP 17	0	0	17	10

Channel Bank Change

Channel bank change was mostly concentrated in bend dominated reaches of the channel with deposition on the inner bend and erosion on the outer bend (Figure 9). Between both 2020 to 2021 and 2021 to 2023, erosion dominated over deposition at channel bends (Figure 12). However, the magnitude of erosion was higher between 2021 and 2023, where it was most active in the bend dominated reach (Figure 9). The highest volume of outer bend erosion was observed at the last

bend before the channel fork which experienced incision depths of up to 13 m into the channel floor along with widening the channel by up to 80 m were observed.

General Channel Change

Change in the channel between 2020 and 2021 that was not accounted for by any of the other processes was predominantly net depositional. This deposition was spatially constrained to the upper reaches of the channel with 88% of this deposition occurring within the first 2 km of the canyon confluence (Figure 8). This was contrasted by change observed between 2021 and 2023 that was predominantly erosional (Figure 8). This was consistent throughout the whole length of the channel apart from the southern distributary channel (Figure 3), which accounted for 90% of the general channel deposition.

Change at the Channel Fork

Between the 2021-2023 bathymetric survey interval, the ridge that formed at the head of the southern distributary channel was removed (Figure 9). The volumetric change associated with the ridge removal was 1.62×10^5 m^3 of material with an additional 6.71×10^4 m^3 of channel erosion at the channel fork which in total constituted 5.4% of the total volume of erosion in the submarine channel during the 2021-2023 survey interval. The erosion above the ridge incised the thalweg in the direction of the southern tributary channel resulting in a 5 m lower channel depth than in the northern tributary channel. Moreover, it created a new knickpoint up-channel from the fork (Figure 14). Below the ridge, the crescentic bedforms were removed by channel erosion, and one of knickpoints (KP 16) was infilled with deposition, then a new knickpoint was created down-channel.

Sedimentary Lithofacies

Three sedimentary deposit types were identified in the sediment cores. These are described in terms of lithology and structure in Table 5and are described in how they change and evolve within

the basin. These lithofacies were interpreted as background hemi-pelagic sedimentation and two magnitudes of turbidite flow types. This facies model was used to interpret the sediment cores which are plotted as graphical logs in Figure 15 to show facies changes over core depth.

Table 5: Sedimentary lithofacies determined from core logging and interpretation

Lithofacies	Lithofacies Name	Lithological Description	Structure	Depositional Process Interpretation	Evolution Through System (Proximal, Midchannel and Distal Cores)
1	Sand Bed	Sand beds were generally between 1 - 30 cm thick, composed of very fine to coarse sand. The beds were either clean sand or muddy sand and sometimes have a mud cap at the top of the deposit. Wood fragments or other organics may be dispersed throughout deposit or layered in laminations.	Either well-sorted, showing a fining upward structure that may contain parallel laminations that are visible in x-ray images and occasionally upon visual inspection, or poorly sorted to massive. Frequently showed a sharp basal contact that is either planar or irregular. The structure at the top of the sand component was often well preserved, whereas the mud cap was often affected by bioturbation.	High density turbidite flow deposit. Ta, Tb, Tc, and Te Bouma divisions (not all may be present).	This facies was most prominently present in channel adjacent settings. In the proximal core, positioned at the first channel bend where the channel is incised to ~45 m depth, there were no instances of this facies observed. The midchannel core, where the channel incision depth was ~15 m, showed frequent clean sand beds up to 30 cm thick with grainsizes up to medium sand. In the distal core beyond the channel lobes, a 6 cm fine sand bed shows decomposing organic matter interlaminated in the Tb interval.

2	Sand Laminations	Laminations < 1 cm of very fine to medium sand and silt. Grainsize affects the characteristics of the laminations in a deposit. Thinner silt laminations often appear in groupings of up to 10, whereas, larger grainsize laminations appear either as a single lamination or in groupings of 2 - 4. A mud cap is often present above the laminations. Wood pieces or other organics may be present.	Laminations were primarily horizontal to sub-horizontal and may be lenticular or wavy. Laminations may be discontinuous across the core or appear mottled due to bioturbation with only trace structure preserved. The spacing between laminations is often a few millimeters but can be up to a few centimeters.	Low density turbidite flow deposits. Or the upper flow regime of a turbidity current that spilled over the levy. Td, Te Bouma divisions.	At the proximal core, laminations were primarily silt and often did not have primary structure preserved. Structures were discontinuous or mottled due to bioturbation. At midchannel cores, fine sand laminations were observed and frequently were associated with a Te mud bed of clayey silt. In the distal core at higher core depths the laminations were present as up to very fine sand with associated clayey silt beds. At lower core depths this transitioned to finer silt laminations that were often bioturbated and mottled.

3	Hemi-Pelagic Mud	Fine grained dark grey mud. Grain size was courser proximal to the river with a higher relative fraction of silt and frequently contains very fine sand that was either disseminated or present as small mottles, whereas the distal core was dominated by clay sized particles with a lower relative silt fraction. Organic matter was disseminated throughout, ranging from microscopic fibers to wood and plant fragments. Shell fragments were common. Bioturbation is frequently present and often extensive.	The unit showed trace to no primary structure. In intervals with heavy bioturbation, burrows may be visible in x-ray images and sections of core with mud and clay mottling.	River sourced sediment and biogenic material. Steady background accumulation rate, that may be augmented by a seasonal river plume during freshet (Fissel *et al.* 2017).	In the proximal core near the delta-front silt and clay were both present in similar proportions. In the midchannel core adjacent to the channel meanders silt was present but at a much lower fraction compared to the proximal core. In Core 13 in the distal ponded basin beyond the channel lobes the dominant grainsize was almost completely clay sized particles.

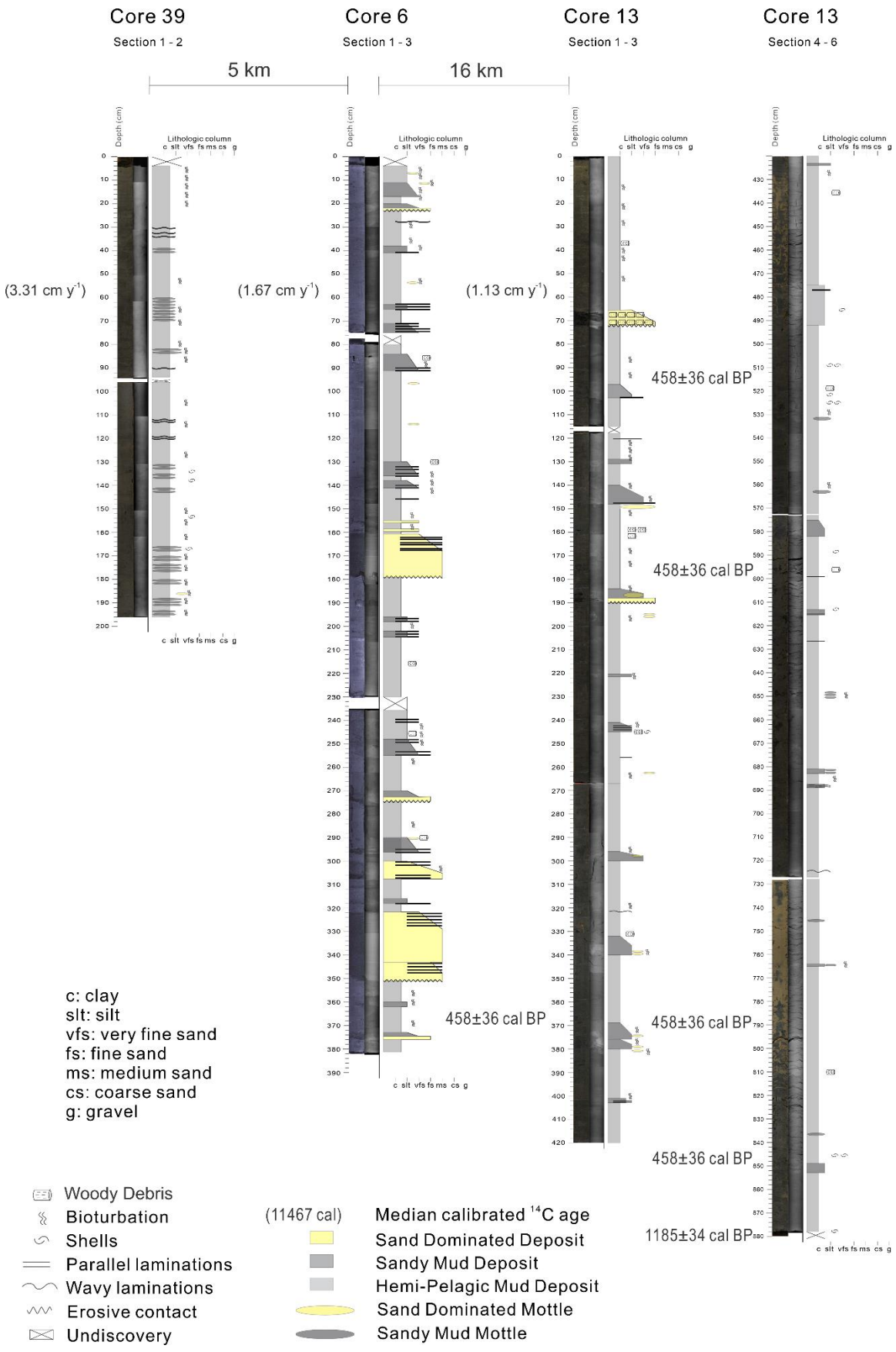

Figure 15: Graphic logs for the sediment cores showing dominant unit types.

Dating and Age Control

Age control for the sediment cores were calculated using an excess ^{210}Pb sedimentation rate. The resulting sedimentation rates were presented as average sedimentation velocities in Table 6. This rate was used to calculate the core depth corresponding to 1964 AD which was inferred to correspond with the measured ^{137}Cs peak in each core, all of which showed good agreement to ± 9 cm of core depth (Table 6) (Ritchie and McHenry 1990). Further age control was provided by the MCMC ^{14}C model for Core 13.

Table 6: Sedimentation rates calculated from excess ^{210}Pb models. The sedimentation rate was used to calculate what core depth corresponds to 1964 AD (the expected peak of ^{137}Cs) which was presented with the core depth of the measured ^{137}Cs peak.

Core ID	Sedimentation Rate (cm year^{-1})	Error (cm year^{-1})	Location	Modelled Core Depth of 1964 AD (cm)	
				^{210}Pb	^{137}Cs
Core 39	3.31	0.31	Proximal	188	193
Core 6	1.40	0.04	Mid-Reach	81	72
Core 13	1.13	0.02	Distal	65	61

^{210}Pb Dating

Thirty-two samples from Core 39 were analysed for excess ^{210}Pb from 0 cm to 196 cm core depth. The boundaries of turbidite beds could not be clearly distinguished in this core and therefore an event-free depth was not established. The samples in the top 10 cm of the core showed signs of bioturbation and were removed from the analysis to calculate the exclusive sedimentation rate (Table 6; Appendix B: Table 16). The background ^{210}Pb activity was not reached and therefore the average ^{226}Ra activity was interpreted as the background value. Twenty samples were analysed in Core 6 from 18 cm to 356 cm core depth (9 cm to 90 cm corrected event-free core depth (Appendix

B; Table 13)). Background ^{210}Pb was reached between 124 cm and 184 cm, so the sample at 184 cm and all samples at lower core depths were excluded from the linear regression model and averaged to calculate the background ^{210}Pb sedimentation rate (Appendix B; Table 13; Figure 26). In core 13, twenty-six samples were analysed from 0 cm to 102 cm core depth (0 cm to 83.5 cm event-free core depth (Appendix B; Table 10)). Samples in the top 10 cm showed signs of bioturbation and were removed from the linear regression model when calculating the exclusive sedimentation rate (Table 6; Appendix B: Table 10). The bottom sample was determined to be in a turbidite event bed, meaning it represented instantaneous deposition outside of the background sediment accumulation rate and was removed from the linear regression for both the inclusive and exclusive sedimentation models (Table 6; Appendix B: Table 10). Background ^{210}Pb activity was not reached in Core 13, so the average ^{226}Ra activity was used for the background rate.

^{14}C Dating

At lower core depths in Core 13, nine samples of organic mater (conifer needles, wood pieces, and decomposed undifferentiated organic matter) and carbonate shells were analysed for 14C dating. The modelled 14C dates are shown in Table 7, with values ranging from 769 AD (1181 years BP) ± 57 years to 1670 AD (280 years BP) ± 15 years. The two shallowest samples (taken at the same core depth) were outlier results. These samples were low in mass and material had to be combined and not fully pre-treated to reach the threshold for analysis. As a result, there was a lower confidence in the quality of these samples, and they were therefore excluded from the MCMC age-depth model (Figure 15). When incorporating the ^{210}Pb and ^{137}Cs data, the MCMC age-depth model was broadly compatible with the ^{210}Pb sedimentation rate but showed a slight decrease in the rate of change of age over core depth at shallower core depths near the ^{137}Cs peak (Figure 15).

Table 7: Event-free-depths and modelled ^{14}C ages in Core 13 along with sampled material type.

Core Depth (cm)	Material	Median Age (Year BP)	Standard Deviation (Year)
211.5†	Conifer needle and wood fragment combined	280	15
211.5†	Wood piece	339	9
319.5	Wood piece	458	36
319.5	Shell fragment	458	36
446.5	Shell fragment	650	28
525.5	Plant fragments	766	22
706	Shell fragment	1050	30
763.5	Wood piece	1140	31
792	Shell (whole bivalve)	1185	34

†Sample rejected.

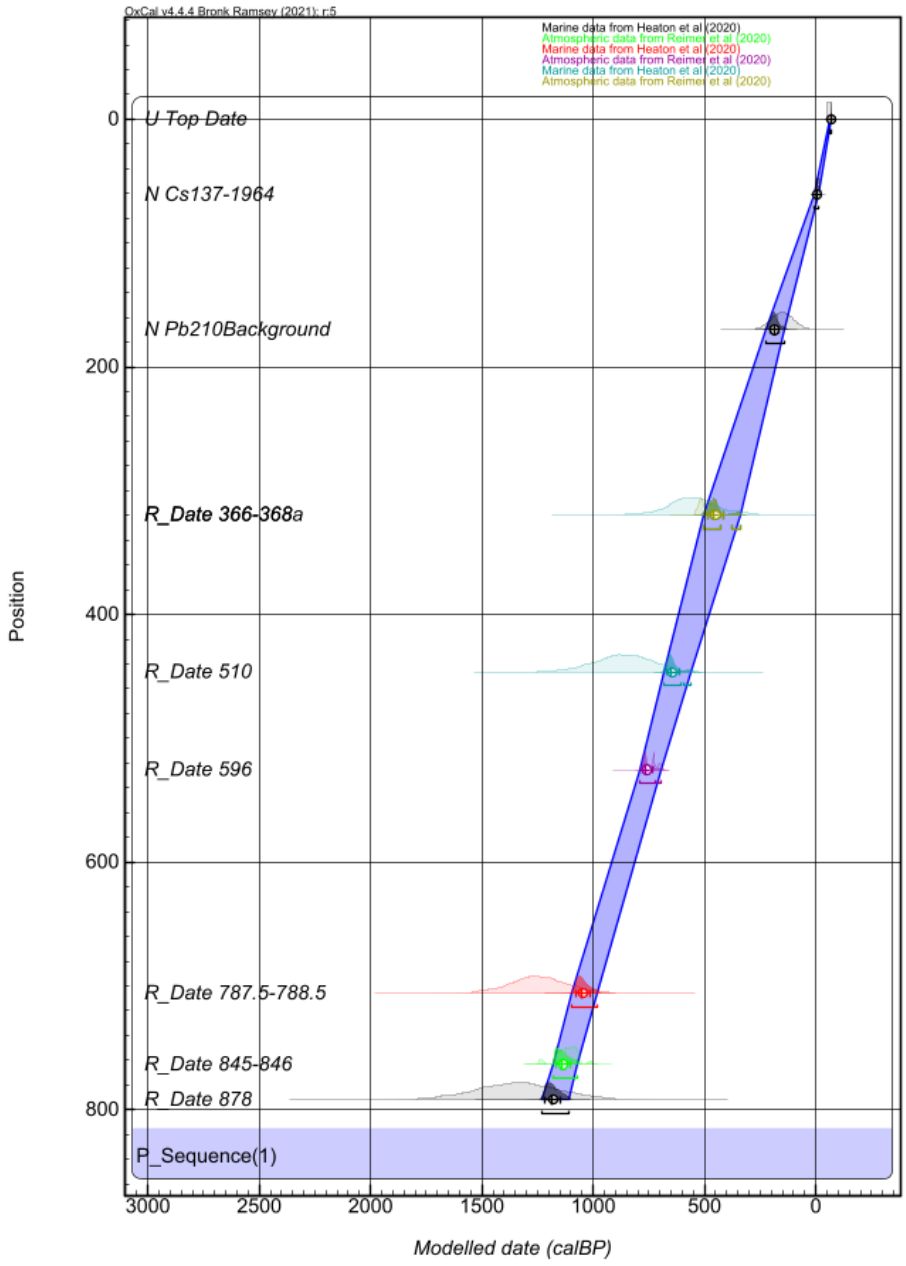

Figure 16: MCMC age-depth model of modelled calibrated ^{14}C dates (plotted as R_date) in Core 13 with predicted 74-year BP ^{210}Pb depth and the 1964 AD ^{137}Cs depth.

Turbidite Bed Return Intervals

The return intervals of the Facies 1 and Facies 2 turbidite deposits in Core 6 and Core 13 were estimated using the age-depth models and are shown in Table 8. Turbidite deposits in Core 39 were generally either heavily bioturbated and/or of similar grainsize to the background hemipelagic

facies meaning that the turbidite deposit boundaries were not distinct enough to date and develop reoccurrence rates. The turbidite deposits in Core 6 were estimated using the excess ^{210}Pb sediment accumulation rate model. In Core 13 the ages of turbidite beds were estimated using the excess ^{210}Pb model for beds dated up to 150 years prior to collection, and then the OXCAL MCMC ^{14}C model for older turbidite beds. Within this range there were overlapping beds that showed that the OXCAL MCMC ^{14}C model provides older estimates for the ages of beds, which is consistent with the rate of change increase observed in the age depth model below the ^{137}Cs peak. Therefore, these reoccurrence rates were presented separately depending on the model used to calculate the age of the bed.

Table 8: Turbidite deposit return intervals based on radiometric dating and broken down by facies type.

	Facies 1			Facies 2		
Core	Total Observed	Average Return Interval (yrs)	Standard Deviation	Total Observed	Average Return Interval (yrs)	Standard Deviation
Core 6	6	25.5	30.2	16	9.5	7.5
Core 13	2	85	N/A	28	15† / 38.3‡	11.6† / 25.9‡

† ^{210}Pb accumulation rate
‡ ^{14}C MCMC age-depth model

Sediment Rating Curve

Mean daily discharge from the Nass River between June 1929 to December 2023 was calculated as 807 $m^3 s^{-1}$ (Water Office: Government of Canada 2023a). Basin height in the Nass River watershed was measured to be 2688 m. Mean annual temperature between 1981 and 2020 was 5.6 °C. From these values, a sediment concentration of $C_s = 6.22 \times 10^{-2}$ kg m^{-3} and suspended load of $Q_s = 50.2$ kg s^{-1} were calculated. The suspended load was used to calculate a yearly sediment discharge of 1.58×10^9 kg $year^{-1}$.

Discussion

Magnitudes of channel mobility

Volumetric change analysis of the three bathymetric surfaces revealed that distinct differences were captured in the submarine channel mobility between 2020-2021 and 2021-2023. Volumetric changes between 2020 and 2021corresponded well to the ‘shuffle’ phase of the ‘shuffle-and-flush’ model (Heijnen *et al.* 2022). Volumetric change was observed in all components of the channel with deposition and erosion approximately in balance, with most activity occurring in the canyons and at knickpoint zones (Figure 3). Overall, there was a net deposition indicating that sediment was being added to the system, but this change is small when compared to changes in depositional and erosional volume from the reworking of sediment already present in the channel system. This is contrasted by the change observed between 2021 and 2023, which could be described as a ‘flushing event’ in the ‘shuffle-and-flush’ model (Heijnen *et al.* 2022). Apart from an approximate balance between deposition and erosion in the canyons, the channel was dominated by erosion. Here knickpoints experienced the largest erosion, followed by channel banks. In total, the proportion of erosion in the channel during the ‘flushing’ more than doubled when compared to the amount erosion from a year of ‘shuffling’ (Figure 11).

If the period between the 2020 and 2021 bathymetric surveys is taken to represent a typical year of ‘shuffling’, then this indicates that the ‘flushing’ event mobilizes more sediment than is deposited by a year of turbidity current activity in the channel. This could be due to a removal of the slowly built-up sediment from multiple years of 'shuffling’ flows and net deposition. However, it could also be from the ‘flushing’ flow incising into the seafloor hemipelagic sediments and further deepening the channel. There is likely a combination of both contributing to this channel erosion during a ‘flushing’ event.

The different magnitudes of volumetric change further imply multiple mechanisms of flow state that drive the runout distance of the turbidity currents. Between 2020 and 2021, the 'shuffling' phase has characteristics of two types of flow state. In the upper reaches of the channel that were dominated by deposition between 2020 and 2021, flows are likely in a dissipation state (Heerema *et al.* 2020), ultimately limiting their runout distance to the canyons and upper reaches. For the rest of the channel length, the balance between erosion and deposition may indicate a flow in autosuspension (Parker *et al.* 1986) where the turbidity current is in a state of equilibrium and erodes and deposits at approximately the same rate as it travels (Heerema *et al.* 2020). This may be exhibiting the behaviour of the traveling wave model where the turbidity current erodes initially with its dense frontal-cell and then deposits approximately an equal amount with through the more dilute tail (Heerema *et al.* 2020, Baker, Talling, *et al.* 2024). The dominance of erosion over most of the length of the channel implies an ignition flow state during the 'flushing' phase (Parker 1982, Heerema *et al.* 2020).

In Channel Mobility

The largest volumes of surficial change were observed to occur at bedforms. There are differences in how these bedforms change between the two different bathymetric survey intervals indicating that this is controlled by the magnitude of the turbidity current flows. Here the in-channel morphology are discussed regarding how they change in response to the interpreted flow magnitudes.

Canyon and Upper Channel Dynamics

The canyon and upper channel were the dominant parts of the channel to experience deposition between 2020 and 2021 (Figure 8). Here crescentic bedforms were the dominant bedform type and were interpreted as cyclic steps (Slootman and Cartigny 2020) as certain bedforms were observed

to migrate upslope and have been observed in other submarine channel systems (Hughes Clarke 2016, Hage *et al.* 2018, Chen *et al.* 2021) which suggests that turbidity current flows are supercritical in this reach. Deposition and the size and wavelength of the cyclic steps decrease to 4 km from the delta-lip suggesting that these bedforms are related to dissipative flows, that as part of the 'shuffle-and-flush' model are from frequent smaller canyon and upper channel filling flows (Heijnen *et al.* 2022). Between 2021 and 2023 showed a reversal where the channel floor was primarily eroded out to 4 km, suggesting that most of the previous 'shuffling' deposition was remobilized by a flow in an ignition state during the 'flush' phase (Parker 1982). However, after where the cyclic steps disappeared and the deposition between 2020 and 2021 stopped, the magnitude of erosion was reduced suggesting that it is easier for an ignitive flow to erode recently deposit material that may be in a less consolidated state than other parts of the channel floor (Figure 8). In the upper reaches of the canyon, deposition was observed indicating that since the 'flushing' event small flow(s) have recommenced the refill process of the 'shuffle' phase.

Knickpoint Dynamics in 'shuffling' and 'flushing' flows

Knickpoints were active during both the surveyed intervals. The lower magnitude flows between 2020 and 2021 caused up-channel knickpoint migrations between 30-230 m/year (Table 4), which are on average slower but of similar magnitude to the migration rates in Bute Inlet (Heijnen *et al.* 2020). The movement of these knickpoints was the largest driver of volumetric change in the channel during this period as the up-channel migration eroded the channel thalweg and appeared to deposit similar volumes down-channel of the knickpoint (Figure 13). This suggests that knickpoints may be part of the maintenance of autosuspension as opposed to sediment bypass (Heijnen *et al.* 2022), where a dense frontal layer of a flow may erode at a knickpoint causing it to migrate up-channel, but sheds an approximately equal volume of sediment at the rear of the flow (Heerema *et al.* 2020). This describes the travelling wave autosuspension model, which if this wave

had a dominant wavelength phase, could explain why certain adjacent knickpoints had similar migration rates in this time interval (KP 7 and KP 8, KP 9 and KP 10, and KP 13 and KP 14; Table 4).

Between 2021 and 2023 the knickpoints had a similar range of migration rates of between 10-215 m/year (Table 4). Here the knickpoint zones had similar up-channel erosive patterns as between 2020 and 2021 and knickpoint inflection points appeared to correspond between surveys so it is assumed that these knickpoints migrated up-channel through similar mechanisms to during the 'shuffle' phase (Figure 8, Figure 9). As no major increase in knickpoint migration rate is observed, it is inferred that the higher magnitude of erosion observed in knickpoint zones during the 'flushing' flow was not solely due to the up-channel migration of knickpoints. Instead, erosion was also observed down-channel from the knickpoint where deposition was previously observed between 2020 and 2021 (Figure 8, Figure 9). Therefore, it is likely that in addition to the up-channel migration, it remobilized sediment that was previously deposited down-channel of knickpoints by 'shuffling' flows. This erosive pattern was present in almost all reaches of the channel which may suggest that the flow was in an ignition state and being continuously fed sediment by the erosion, but the magnitude of erosion at knickpoints decreased with distance along the channel and therefore would not be increasing in flow power, which is different from the proposed ignition model (Parker 1982, Heerema *et al.* 2020).

Although there was significant movement of knickpoints between 2020 and 2021, it was only during the 2021 to 2023 interval that knickpoints appeared or disappeared. In the Nass channel, five new knickpoints were observed (Table 4). Three of the five appeared in channel bends that had constriction points from point-bars in the inner-bend and a slope-break coming out of the bend (Figure 14). This is consistent with the knickpoint initiation observed in Capbreton Canyon where (Guiastrennec-Faugas *et al.* 2021) suggested that the lateral confining effect of the bar could induce supercritical conditions and create a hydraulic jump. Two of these knickpoints appeared to

result from a larger knickpoint breaking up during its up-channel migration (Figure 14), which is consistent with what was observed in Bute Inlet (Heijnen *et al.* 2020). The other knickpoint that appeared at a bend also experienced a large volume of outer bend erosion which may have contributed to its creation although the mechanism for that is unknown. This suggests that the constriction of flows at bends may be able to generate knickpoints, but it is unclear if it requires either a knickpoint (Heijnen *et al.* 2020), blockage (Guiastrennec-Faugas *et al.* 2021, Pope, Heijnen, *et al.* 2022) or some other variation in the channel floor already present to induce this change, or a secondary erosive presence to induce this change. (Heijnen *et al.* 2020) suggested that knickpoints in Bute Inlet were generated around the channel-to-lobe transition zone, and features that resemble knickpoints have been observed to erode and migrate up-channel from the channel lobe transition zone at the Squamish Delta (Vendettuoli *et al.* 2019). This could also be a source in the Nass channel, as the closest knickpoint is within 400 m of the lobe without a bend or other morphological feature to induce the creation of the knickpoint in the channel.

One knickpoint was created up-channel of the fork after the channel reactivation. This likely represents a special case for knickpoint creation as there was a large volume of thalweg erosion also associated with this event. Furthermore, down the southern distributary channel from the fork, a knickpoint inflection point was removed in what appeared to be infill deposition on the down-channel side, and then a reactivation of a knickpoint inflection point in that deposited material. In this reach, more deposition was observed during this period indicating that the flow may have switched to a dissipation state. Two other knickpoints were observed to disappear. Both were poorly developed with minor relief (<5 m). They were removed from a straight section of the channel where the channel was lowered by general thalweg erosion (Figure 9).

Outer Bend Erosion

During the ‘flushing’ flow both outer bend erosion and general thalweg erosion were pervasive throughout the channel (Figure 3; Figure 12). The erosion rates from outer bend erosion approximately doubled during the ‘flushing’ phase between 2021 and 2023 from what was observed between 2020 and 2021 (Figure 12), but in both phases contributed a similar relative proportion of approximately 25% of the total measured erosion. This proportion is higher than what was observed in Congo Canyon where outer bend erosion was measured to contribute 10% of the total erosion during a ‘flushing’ event (Ruffell *et al.* 2024), but similar to the proportions of 21% in Bute Inlet (Heijnen *et al.* 2020) and 23% in Knight Inlet (Zulkifli *et al.* 2024) where the flow magnitudes were not discerned. When knickpoints were observed in meandering reaches of the channel that also had outer bend erosion, it was difficult to determine which process was dominating. If both the outer bend erosion and knickpoint migration occurred in the same flow, then this suggests that the internal state of the flow allows for both types of erosion to occur. The cooccurrence of knickpoint migration and outer bend erosion was also observed in Bute Inlet where Heijnen *et al.* (2020) suggested that knickpoint migration enhances outer bend erosion, resulting in bend migration rates up to 10 m/year. In the Nass channel there is cooccurrence of knickpoint and outer bend erosion (Figure 9), but it is less clear if this enhanced the rate of outer bend erosion as the highest magnitudes of outer bend erosion (with lateral bend migration rates up to 10 m/year during the ‘shuffling’ phase and 45 m/year during the ‘flushing’ phase) were observed up-channel from where knickpoint migration occurred.

Bedform Fields

The bedform fields influenced by channel spillover flows showed change during both survey intervals but were more active in the ‘flushing’ phase between 2021 and 2023. The most common

volumetric change observed was deposition on the stoss side of sand waves, with occasional erosion visible on 'flushing' flow phase there was also erosion visible on the lee side of bedforms indicating that these bedforms may be upslope migrating and against the spillover direction, which is also indicated by their upslope asymmetry in cross section profile (Figure 6, Figure 9). In both survey intervals, the bedform fields near the distal channel were more active, with the most change observed on the southern side of the last channel meander bend (Figure 3, Figure 9). This indicates that flow spillover occurs more frequently and/or to a larger extent at more distal reaches of the channel, and turbidity currents are more likely to remain channelized through the mid reaches of the channel which is independent of flow magnitude. These results show some similarity to Bute Inlet where only specific reaches show spill over bedforms (Prior *et al.* 1987), but the bedform fields in the Nass Delta system occupy a larger spatial extent over more reaches of the channel.

Lobe building flows

Sediment deposition on the lobe was observed between 2020 and 2021 and 2021 and 2023, indicating that in both time periods there were turbidity current flows that traveled the length of the channel. In the Bute Inlet channel system, it is estimated that on average one turbidity current delivers sediment to the lobe each year, but that these deposits were not resolvable using MBES bathymetry change detection (Heijnen *et al.* 2022). As the lobe deposits at the Nass Channel are well defined with extensive fields of sediment waves this could indicate that this system either carries more sediment to the lobe in one turbidity current flow, or experiences flows that reach the lobe more often. Given that the Bute Inlet submarine channel is twice as long as the Nass Channel, it is plausible that even with similar rates and magnitudes of turbidity current occurrence, the Nass Channel could receive a higher frequency of lobe building flows.

The implication of these results has shown that contrary to the 'shuffle-and-flush' model presented in Bute Inlet (Heijnen *et al.* 2022), lobe deposition occurred in the Nass Delta submarine channel system during the 'shuffling' phase between 2020-2021. This shows that 'shuffling' flows can contribute to lobe building as they are able to transport sediment the full length of the channel without a more significant 'flushing' flow needing to occur. However, these volumes of lobe building sediment are small compared to the 'flushing' phase which resulted in over an order of magnitude more deposition on the lobe, with a much larger spatial extent of several lobes (Figure 11).

Channel Reactivation

A notable change in morphology within the channel was the reactivation of the southern distributary channel between 2021 and 2023. Between 2020 and 2021, this channel had been separated from the active channel by a ridge and no significant sediment movement was identified within the channel or associated depositional lobe (Figure 3). As the southern distributary channel was incised to a lower depth than the northern tributary channel it is inferred that the ridge was maintained by levee building in the northern tributary channel. Between 2021 and 2023, the 'flushing' period, the ridge was eroded, knickpoint migration and volumetric change were identifiable within the channel, and deposition occurred on the associated lobe, indicating that the channel had been reactivated. Some activity still took place in the northern distributary channel, but it is unknown if that occurred before or after the channel reactivation.

Both the northern and southern distributary channels have well defined lobe complexes at their terminus, which indicates that both the distributary channels had experienced prolonged active periods as conduits of turbidity current flows to the lobe. It is possible that the southern distributary channel was the original channel, and then a large turbidity current caused a channel

avulsion to create the northern distributary channel that became the dominant channel until the 'flushing' event between 2021 and 2023. It is also possible that since the original avulsion, the northern and southern channels may alternate as the dominant transport pathway for turbidity currents with large turbidity current 'flushing' flows causing the channel to switch back and forth.

The initial avulsion event may have also occurred at the channel-lobe transition zone. Channel avulsions have been observed in deep sea fans (Kolla 2007) where changing flow conditions can initiate a hydraulic jump that migrates against the direction of flow (similar to knickpoints) and allows the channel to split off it a new direction (Hamilton *et al.* 2015). A younger version of the channel may have had the lobe positioned at the channel fork, where the initial avulsion occurred building the two distributary channels, and then through subsequent channel reactivations have built out lobe complexes at the terminus of both distributary channels. Evidence for this is shown in the morphology observed between the distributary channels. Here the sediment waves have similar wavelengths and wave heights to those found in the lobe complex and had crescentic shaped scours that were otherwise only observed at the lobe complex. Similar scours have been observed in channel-lobe transition zones that were interpreted to result from flow relaxation (Pohl *et al.* 2019). Moreover, these scours have been interpreted to allow a channel to propagate (such as at the Squamish Delta) (Pohl *et al.* 2019), which could explain the growth of the distributary channels through the previous position of the lobe.

Flushing Flows as Thresholding Events

In the Nass channel, it appears that 'shuffling' flows can induce changes in channel morphology, especially in knickpoints and by outer bend erosion. However, none of these changes caused the channel morphology to be permanently altered out of its equilibrium state (i.e., the dominant channel banks). Whereas a 'flushing' flow was able to change the equilibrium of the channel by

removing the ridge at the channel fork to reactivate the southern distributary channel and change the dominant region of sediment delivery to the lobe. Moreover, it was able to induce the creation and destruction of knickpoints which were not otherwise observed during the 'shuffling' phase. Such an event can be referred to as a geomorphic thresholding event where there is a large enough change in a system that alters its morphology and forces it to shift to a new equilibrium (Schumm 1979). In contrast, 'flushing' flows in other turbidity current systems caused higher magnitudes of erosion, but did not significantly alter channel morphology (Heijnen *et al.* 2022, Ruffell *et al.* 2024). Therefore, here the term 'thresholding flow' is proposed to distinguish 'flushing' flows that permanently alter channel morphology.

Sources of sediment and turbidity current triggers

Using the sediment rating curve, the Nass River was shown to deliver 1.58×10^9 kg year^{-1} of sediment based on average discharge conditions. This value is several orders of magnitude above the net deposition on the lobe between 2020 and 2021 of 2.6×10^9 kg year^{-1} (Table 3). However, this value accounted for only 20% of the sediment on the lobe as measured between 2021 and 2023 (Table 4). This suggests that 'flushing' flows can mobilize up to five years of sediment deposition on the delta.

As there are no precise measurements of turbidity currents in the Nass Channel system, the exact source and triggers for these flows are unknown. However, based on previous research of turbidity current initiation on delta-channel systems (Clare *et al.* 2016, Lintern *et al.* 2016, Hage *et al.* 2019, Bailey *et al.* 2021), potential sources and triggers include elevated seasonal sediment plumes from the Nass River, an increase in sediment load in the Nass River due to landslides or debris flows within the watershed, or slope failures on the Nass Delta lip. Each of these potential initiation mechanisms are discussed in this section based on available data.

Source 1: Seasonal Sediment Plumes

Previous work in similar river-fed submarine channel settings have shown that turbidity currents can form in hyperpycnal conditions with a high turbidity river input (Mulder and Syvitski 1995) and homopycnal conditions from dilute river plumes (Clare *et al.* 2016, Hage *et al.* 2019). The sediment rating curve did not predict hyperpycnal conditions for the Nass River with a sediment concentration of 0.062 kg m^{-3}, far below the 30 kg m^{-3} threshold for hyperpycnal conditions (Mulder *et al.* 2003), and are therefore unlikely unless generated by a large flooding event (Mulder and Syvitski 1995). Discharge data for the Nass River does not show an exceptional flooding event during the study period where discharge data was available (Figure 17) (Water Office: Government of Canada 2023a). Hydrometric data for 2021 is missing from the record, but discharge data from Ansedagan Creek, a Nass River tributary that generally has a similar hydrographic profile (Figure 17) showed a flooding peak in spring and one in the fall of 2021, each with the duration of ~3 days (Water Office: Government of Canada 2023b). There may have been a similar peak in the Nass River discharge, however, it is unknown if this would translate to hyperpycnal conditions. Other events such as a landslide or debris flow that reached the Nass River could also induce hyperpycnal conditions, but there were none of these events observed between 2020 and 2023 in the Nass River watershed (Marten Geertsema – Personal Communication 2024).

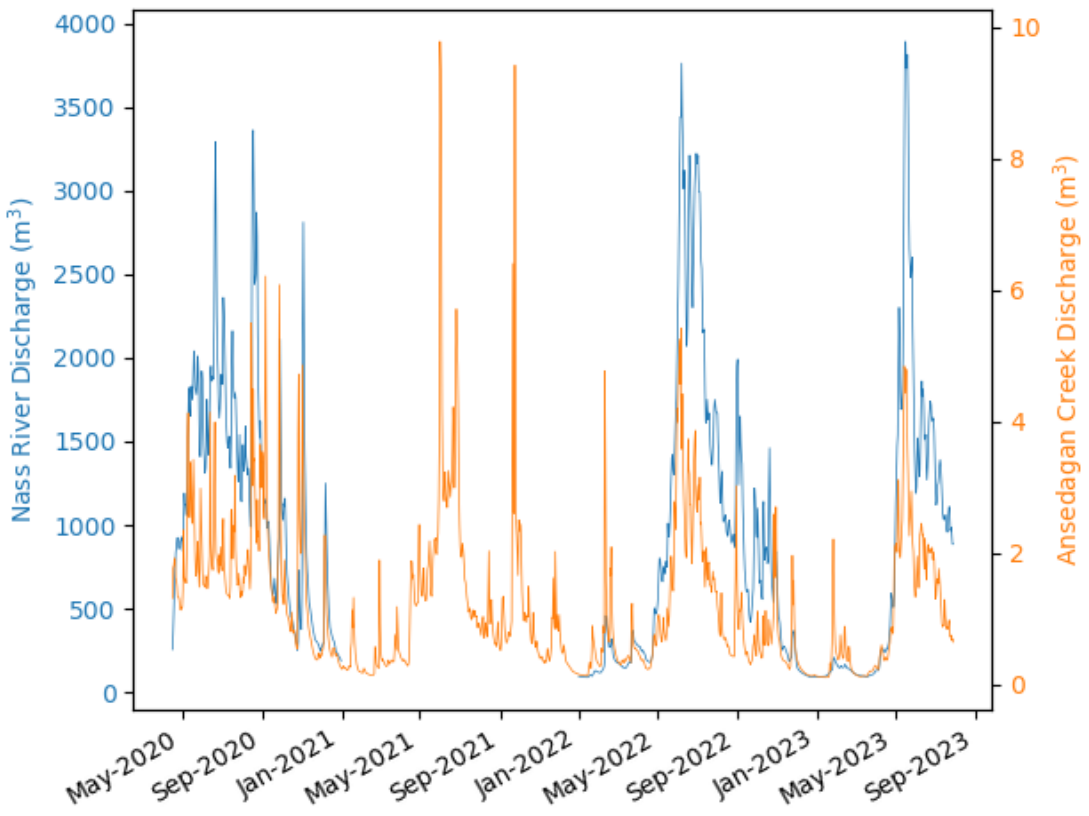

Figure 17: Daily discharge for the Nass River (left Y-axis) and the tributary Ansedagan Creek (right Y-axis) throughout the during of the study period. Both discharge curves show similar timing in their discharge peaks, although not necessarily the same magnitude of change. Notably, Ansedagan Creek shows two discharge peaks higher than observed during the rest of the study period in 2021 where no discharge data is available for the Nass River.

Homopycnal conditions at deltas have been shown to generate turbidity currents through convective settling of sediment (Parsons *et al.* 2001) when affected by certain tidal conditions such as spring-neap tidal cycles (Lintern *et al.* 2016, Hage *et al.* 2019, Hill and Lintern 2021). The conditions for a homopycnal initiated turbidity current exist at the Nass Delta. The most likely timing for generating one or more turbidity currents would be during the 2022 freshet where there was an elevated discharge of ~3200 m^3 s^{-1} for approximately a month (Figure 17, Figure 18). During this period, a spring-neap tidal cycle was observed with a tidal range that increased from 2 m to 5 m to 0.1 m to 7 m (Figure 18). A second set of tidal variations occurred during the rest of the freshet, showing another increase in tidal cycle ranges that peak at a range of 1 m to 6 m (Figure 18). (Fissel *et al.* 2017) conducted a study of ten years of satellite imagery which showed that the Nass River

has an increase in sediment discharge during spring freshet and high rainfall events in the fall. Suspended sediment load can be further enhanced by strong tidal currents on the spring tide as they increase bottom shear stress and remobilize sediment in Nass Bay (Fissel *et al.* 2017). Moreover, bottom shear stress is locally affected by changes in stratification due to freshwater discharge from the Nass River (Fissel *et al.* 2017), creating further conditions to remobilize sediment. The combination of these tidal factors and the sustained freshets in the Nass River (Figure 17) suggests this may be common mechanism for inducing turbidity currents.

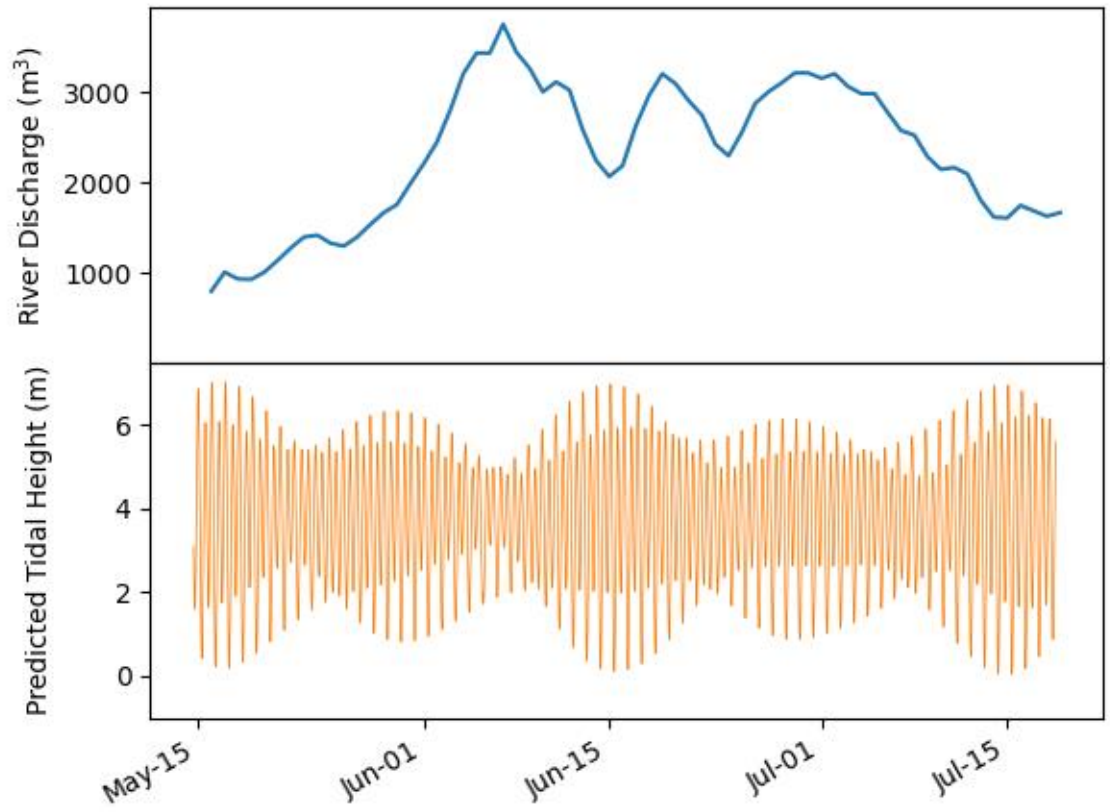

Figure 18: Daily discharge measurements of the Nass River during the 2022 freshet (Water Office: Government of Canada 2023a), and a spring-neap tidal cycle during this period (Department of Fisheries and Oceans Canada tidal prediction station 09422 Gingolx, BC (https://tides.gc.ca/en/stations/09422)). Discharge peaks on June 8, 2022, during neap tide, which is then followed by a spring tide.

Source 2: Slope Failure

Another potential source of the turbidity currents in the channel system are slope failures on the delta lip or within the submarine canyon heads. Slope failures have been identified as the source of turbidity currents in other delta-front submarine channel systems (Clare *et al.* 2016). Known delta slides have occurred on the Fraser Delta with one documented event of > 1 x 10^6 m^3 (McKenna *et al.* 1992) and at Squamish and other deltas (Obelcz *et al.* 2017, Stacey *et al.* 2019). The large erosive area shown in the southern tributary canyon between the 2020 and 2021 may have been related to a slope failure and is a likely source of one or more turbidity currents between this interval as it would have mobilized 3.5 x 10^5 m^3 of sediment over an area of 6.1 x 10^4 m^2 with erosion incision depths up to 20 m. Although no large erosive events were visible in the 2021 – 2023 survey interval, a slope failure on the delta-lip is a possible source for the excess sediment shown in the volumetric differencing results. The full extent of the northern tributary canyon has not been mapped with high-resolution MBES bathymetry data, but the delta-lip position was mapped using available low-resolution bathymetry data, which shows that the canyon extends for an additional 8.52 x 10^5 m^2 of area (Figure 3). To generate the volume of sediment needed for 4.44 x 10^6 m^3 of net deposition, an area between 1.78 x 10^5 m^2 and 4.44 x 10^5 m^2 would need to be eroded with dominant incision depths of between 10 m to 25 m, which based on the observed 2020 – 2021 erosional event, is possible.

Frequency of Turbidity Current Magnitudes

Although there is no data on the frequency of turbidity currents that occur within the channel, the sediment cores past the channel levees and in the distal ponded basin show the frequency of turbidity current flows that were able to spill out of the channel and deposit sand beds, thus representing larger flows as shown in other fjord-delta submarine channel systems (Stacey *et al.*

2019, Hage *et al.* 2022). The proximal Core 39 shows evidence of frequent small flows (Facies 2) occurring within a 50-year interval with no sand beds. Possible sources for these deposits are either frequent dilute turbidity currents that do not travel far down the length of the channel (Simmons *et al.* 2020, Heijnen *et al.* 2022) or only the dilute top component of larger turbidity current flows (Azpiroz-Zabala, Cartigny, Talling, *et al.* 2017, Paull *et al.* 2018, Heerema *et al.* 2020, Pope, Cartigny, *et al.* 2022) that spill over the channel bank and levee via flow-stripping (Piper and Normark 1983). Channel relief is high in this reach (~45 m), and it is therefore unlikely that the high-density components of turbidity currents would overspill here.

The mid-reach Core 6 showed the highest proportion of both Facies 1 and Facies 2 turbidite deposits per length of core. Notably, the Facies 1 deposits here were the largest sand beds observed with deposit thickness of up to 30 cm (Figure 15), which likely represent the spillover of larger turbidity currents, similar to the depositional change observed in the bathymetric difference maps. Six of these deposits were observed with a return interval of 25.5 ± 30.2 years, showing large variability in the frequency of deposition (Table 8). None of these deposits would be resolvable in a differencing map, and both the bathymetry survey intervals were shown to leave larger deposits in the bedform fields, so these deposits could result from either ‘shuffling’ or ‘flushing’ flows.

Facies 1 turbidites deposits in the distal Core 13 are likely deposits from ‘flushing’ flows as it is 3.75 km from the end of the lobe meaning that only the most energetic flows could travel this length. Core 13 contained two Facies 1 turbidite deposits that were dated to approximately within ~80 years of each other, with the most recent one being deposited ~60 years ago meaning that the observed ‘flush’ between 2021 and 2023 would be on a similar frequency return interval. The dated record in the distal ponded basin core extends to 1177 ± 57 years BP. However, the oldest Facies 1 deposit was only observed at 85 ± 3 years BP, meaning that Facies 1 was only observed in the last ~12% of the record. Facies 2 deposits were more common and found throughout Core 13 and may

represent ‘flushing’ flows where only a less dense component of the turbidity current travelled this distance. This facies had a return interval of 15 ± 11 years or 38 ± 26 years (depending on the dating method used) (Table 8) meaning that ‘flushing’ flows may be more common, but not all of them have the competence to transport of sand this distance. Moreover, this may be related to avulsions at the channel fork, as flows travelling through the northern distributary channel would have to travel 9 km from the corresponding lobe to reach the position of Core 13.

Geohazard Implications

Seafloor channels and associated fields of bedforms represent seafloor processes that are hazards to seabed infrastructure (Hsu *et al.* 2008, Mosher *et al.* 2010, Talling *et al.* 2023, Bricheno *et al.* 2024). Detailed analysis is required to determine the extent of activity of submarine channel systems when planning infrastructure such as submarine transmission cables, pipelines and fiber optic networks. Repeat bathymetric surveying of the Nass channel system has shown active erosion and deposition throughout the full length of the submarine channel, with localized change > 10 m indicating that any infrastructure placed through the channel would be in danger of being damaged by a turbidity current flow. Local slopes can be subjected to rapid changes, particularly in knickpoint zones where cables could be left spanning long gaps. Sediment cores from the channel levees show that turbidity currents have been active in this system with a frequency of 9.5 years for small deposits and 25.2 years for larger deposits (Table 8), well within the expected lifespan of most major infrastructure projects.

The region around mid-reach channel meanders also present a large hazard as here there are bedform fields of sediment waves that extend up to ~2 km from the channel (Figure 4). These features indicate past overspill of turbidity currents that run out well beyond the boundary of the channel. Their presence indicates the possibility for high velocity and sediment dense flows that

can damage seabed infrastructure including transmission cables, telecommunication cables and pipelines (Hsu *et al.* 2008, Gavey *et al.* 2017, Bricheno *et al.* 2024). When active, sediment waves can migrate in response to turbidity current flows, resulting in possible burial or exposure of seabed infrastructure. It is unclear from this study how active the full range of the bedform field is at present. The difference maps indicated some amount of activity with resolvable erosion and deposition that was most prominent in the most distal meander bend up to 1.5 km from the channel between 2021 and 2023, but less change was resolvable in the more proximal bedform fields (Figure 9). Core 6 from the bedform field at first meander bend shows frequent Facies 1 and 2 turbidite deposits indicating that historically this region has frequent flows that spillover the channel levee (Figure 2, Figure 15). Moreover, all the deposits recorded in this core have deposit thicknesses below the resolvable threshold for bathymetric change indicating that activity in the bedform field may be underestimated by the difference mapping analysis.

The risk of destructive unchannelized turbidity currents on the lobes can be considered similar to that on the overbank fields of sediment waves at the mid-channel bends. The geohazard potential of the channel lobe region depends on the magnitude of the turbidity current flows. During the observed 'shuffling' phase of the flow, there is limited resolvable activity on the lobe which is contained to within 1 km of the end of the northern distributary channel. This may not capture the full extent of the burial potential as deposition in likely underestimated in the difference map. Likewise, now that the southern distributary channel has been reactivated it is unknown how this will change the dynamics of lobe deposition. During the 'flushing' phase the spatial extent of deposition was extensive indicating that most of the width of the Portland Inlet fjord would be subject to burial hazard. This hazard is highest on the southern side of Portland Inlet which is dominated by the southern distributary channel lobe complexes, which show the largest lateral spread and depth of deposition (Figure 3, Figure 10). However, there was also extensive deposition

at the northern distributary channel lobe, which, combined with deposition from the southern distributary channel lobe and a fan deposit on the northern fjord wall that constricts the fjord floor to 3 km in width, resulted in deposition across almost the entire width of the fjord floor. Therefore, any seafloor infrastructure in the region of the Nass submarine channel system may be at risk of damage from high velocity, sediment laden flows and/or burial during a 'flushing' event.

The geohazard potential to underwater infrastructure is likely reduced beyond the terminus of the lobe complex. However, as indicated in Core 13, large turbidity current flows can travel beyond where the outer limits of the lobe morphology are resolvable and into the distal basin (Figure 3, Figure 15). Here the hazards are less frequent as the only two large Facies 1 deposits were dated to within 85 years of each other and may only be related to the largest 'flushing' flows (Table 8). Further investigation is needed to establish if these deposits are related to 'flushing' flows, such as taking a repeat core at this location to see if there are any deposits since the core was collected in 2021.

Conclusion

This study combined change detection using high-resolution bathymetry and sediment coring to show that the Nass Delta submarine channel system has high turbidity current activity on both short (~1 year) and longer time scales. The bathymetric change detection showed that the channel system experiences at least three magnitudes of flow which corresponds well to the previously advanced 'shuffle-and-flush' model. The 'shuffle' phase appeared to show dissipating flows in the proximal channel reaches with net deposition, and an autosuspension flow state with balanced erosion and deposition, often centered around knickpoints in the remainder of the channel. The 'flushing' phase was primarily erosive through out the whole length of the channel which suggests an ignition flow state. Bedform fields outside of the channel levee had active deposition during

both the ‘shuffling’ and ‘flushing’ intervals, which was spatially variable and most concentrated in the more distal reaches. A sediment core in one of the bedform fields showed that small turbidites are deposited with a return interval of 9 years and 21 years for larger turbidites. Both the ‘shuffle’ and ‘flushing’ phases were shown to contribute to lobe building, but with much higher volumes of deposition during the ‘flush’. A sediment core in the distal setting of the system shows that large flows only travelled past the lobe twice in the last ~750 years, which were both dated to within the last 150 years. Smaller deposits were more common here with a return interval of 15 to 40 years. This indicates that the channel system presents a significant geohazard risk to underwater infrastructure in the region.

Both the ‘shuffle’ and ‘flushing’ phases induced changes in morphology. Knickpoints and cyclic steps were observed to migrate up-channel during ‘shuffling’ and ‘flushing’ flows. However, the ‘flush’ magnitude of the flow was also shown to induce the creation and removal of specific morphological features including knickpoints and a ridge separating the southern distributary channel from the upper channel resulting in a channel avulsion. Knickpoints were either created in channel bends with point-bar constriction, or from flow changes related to the removal of the ridge, which also removed a knickpoint by infilling the inflection point with sediment. Other knickpoints that were poorly developed with a shallow relief (>3 m) were observed to disappear due to erosion in the thalweg during the ‘flushing’ phase. The channel avulsion and creation of new knickpoints resulted in a change in channel equilibrium state and therefore the term *thresholding flow* is proposed to classify this type of ‘flushing’ event.

Chapter 3: Conclusion

Objective 1: Determine how geomorphologically active the seabed is between bathymetry survey intervals and analyse specific seabed morphologies and subbottom structure to infer turbidity current characteristics.

In this study, change detection from repeat bathymetric surveys was synthesized with sediment core stratigraphy to assess the frequency and magnitude of turbidity currents in the Nass Delta submarine channel system. The repeat bathymetric surveys demonstrated that the submarine channel system is active on a yearly timescale, with all channel components experiencing some measurable amount of deposition and erosion within a year. Between the 2020 and 2021 bathymetric surveys, most of the surficial change was within the submarine channel where deposition and erosion were approximately in balance, with only minimal deposition on the channel lobe complex or from overspill flows in the bedform fields over the channel levee. This was contrasted with the surficial change between 2021 and 2023 where there was primarily erosion in the submarine channel, a higher magnitude of deposition from flow overspill in the bedform fields and significantly more deposition on the lobe complex. In accordance with objective 2, these bathymetric changes were inferred to represent three flow magnitudes. The first is a dissipative flow (Parker 1982, Sequeiros *et al.* 2009, Heerema *et al.* 2020) that resulted in the deposition observed in the canyons in both surveys and in the upper channel between 2020 and 2021. The second was a 'shuffling' flow (Heijnen *et al.* 2022), which appeared to move sediment in a type of auto-suspension that locally deposits and erodes in the channel but is in balance with no

significant net change (Heerema *et al.* 2020). The third magnitude was predominantly erosive that was interpreted to be an ignitive 'flush' flow (Parker 1982, Parker *et al.* 1986, Heerema *et al.* 2020, Heijnen *et al.* 2022), which removed sediment from within the channel, preferentially that was deposited by the previous dissipative and 'shuffle' flows.

The range of flow magnitudes influenced the morphology of the submarine channel system as different flow types appeared to interact differently with different morphologies. Cyclic steps in the canyons and upper reaches of the channel showed active surficial change in all flow types but were net depositional in the 'shuffling' phase and net erosional in the 'flushing' phase. Knickpoints showed up-channel migration in both bathymetric survey intervals but during the 'shuffling' phase often showed a balance between erosion and deposition whereas the 'flushing' phase showed erosion from up-channel migration and removal of previous deposition from the 'shuffling' phase. Moreover, only during the 'flushing' phase were knickpoints created and/or removed. Knickpoints were most frequently created in channel bends where a point bar creates a constriction in the channel. Knickpoint removal was mostly associated with poorly developed low relief knickpoints that were removed by erosion of the thalweg. A channel avulsion was also observed to both create a knickpoint up-channel of a ridge that was blocking one of the tributary channels that was removed during the 'flushing' event, and down-channel of the ridge where an existing knickpoint was infilled with sediment and re-established down-channel in this new deposition. The erosion of the outer bank of channel bends was observed in both bathymetric survey intervals but was enhanced during the 'flushing' event. Likewise, lobe building deposition was observed between both surveys, but was much more extensive in the 'flushing' event, which affected specific lobe morphology such as bedforms which were aggraded, crescentic scours that showed erosion and migration against the direction of flow (including potential knickpoints in headless channels showing up-channel migration), and the establishment of flow parallel rills on the lobe.

Objective 2: Evaluate potential initiation mechanisms for turbidity currents on the Nass Delta.

As there were no measurements of the timing of the turbidity currents in the Nass Delta, it is unknown what the specific triggering mechanism of these flows are. The most likely causes are slope failure on the delta lip or convective settling from homopycnal conditions (Parsons *et al.* 2001, Hage *et al.* 2019). Small slope failures were observed between 2021 and 2023 in the canyons and a larger erosive mass wasting event of 3.5×10^5 m^3 of sediment with the potential to trigger a larger turbidity current was observed here between 2020 and 2021. The conditions for generating turbidity currents from homopycnal conditions were inferred to be most likely to occur during seasonal freshets where elevated discharge increases the sediment supply to the delta for over a month, during which a neap-spring tide cycle can allow for settling deposition on the delta and subsequent remobilization to increase the density of suspended sediment and potentially ignite a turbidity current (Lintern *et al.* 2016, Hage *et al.* 2019). However, without direct monitoring of turbidity currents, these processes cannot be connected to specific flows.

Objective 3 & 4: Identify and describe turbidity current deposits in the stratigraphic record to establish distinct facies groupings. Develop a sedimentation rate model to develop to date turbidite deposits and determine reoccurrence rates.

Three sediment cores were analysed to determine the frequency and magnitude of turbidity currents that were retained in the stratigraphic record. In the Nass submarine channel system two turbidite facies were observed. Facies 1 was described as sand beds greater than or equal to 1 cm

thickness that exhibited the T_a, T_b, T_c and sometimes T_d components of the Bouma sequence (Bouma 1962, Talling *et al.* 2012), which were inferred to represent larger magnitude flows. This facies had a return interval of 21 years in the mid-channel at Core 6 and 85 years in the distal basin at Core 13. Facies 2 was described as sand and/or silt laminations that may occur with a silt bed, which were interpreted as the T_d and T_e components of the Bouma sequence (Bouma 1962, Talling *et al.* 2012) and interpreted as smaller flows overtopping the levee or the dilute top component of flow being stripped. This facies had a return interval of 9 years in the mid-channel at Core 6 and 15 to 40 years in the distal basin at Core 13. Without direct monitoring of flows it is unknown which flow magnitude, as observed in the bathymetric change, connects to which deposit type although it is likely that the 'flushing' flows produced the Facies 1 deposits observed in the core in the distal ponded basin. However, both bathymetric survey intervals showed deposits in the bedform fields that are thicker than any turbidite deposits identified in the cores in this region, meaning that both time periods experienced flows that could produce this facies. In Bute Inlet flow monitoring by ADCPs linked flows with a thin, fast, dense head and a high sediment concentration to a facies similar to Facies 1, and flows with a thick, slow, dilute head with a low sediment concentration to a facies similar to Facies 2 (Pope, Cartigny, *et al.* 2022), which may suggest similar flow behaviour to the Nass Delta submarine channel system.

Objective 5: Characterize the extent of the seafloor geohazard potential from turbidity currents at the Nass Delta.

The frequency of turbidity current activity in the Nass Delta submarine channel system was shown to pose a geohazard risk to seabed infrastructure. In all bathymetric survey intervals, turbidity currents were observed to modify the seafloor along the full length of the submarine channel. During the 'flushing' event, deposition was observed across the width of the fjord in the lobe

complexes and channel overspill sections. Bedforms such as sediment waves were observed up to 2 km from the channel indicating that turbidity current flows reach this distance from the submarine channel. Moreover, sediment cores show deposits from high magnitude flows escape from the channel at least once a decade and can periodically travel beyond where morphology is visible in the channel system. All these observations are indicative of turbidity current flows that could damage, destroy, or bury underwater infrastructure in the submarine channel system.

What makes the Nass Delta Submarine Channel System Unique

This study of the Nass Delta submarine channel has shown that this system is unique in several aspects when compared to other delta-submarine channel systems in British Columbia. The Nass Delta channel was observed to show consistent surficial change along the whole length of the submarine channel and lobe deposition in all the survey intervals including short time scales of ~1 year which is less common in other systems such as Bute Inlet, Knight Inlet and Toba Inlet (Conway *et al.* 2012, Heijnen *et al.* 2022, Zulkifli *et al.* 2024). The highest outer bend erosion rate in the Nass Delta submarine channel were measured to be 40 m/year which is four times higher than the maximum rate measured in Bute Inlet and nearly ten times the rate measured in Knight Inlet (Heijnen *et al.* 2020, Zulkifli *et al.* 2024). A channel avulsion event has also not been observed in any of these previously studied submarine channel systems, including in response to 'flushing' flows (Conway *et al.* 2012, Heijnen *et al.* 2022, Zulkifli *et al.* 2024). The Nass Delta system has a unique positioning out of channel bedform fields. In Bute Inlet and Knight Inlet, bedform fields are common on the delta clinoform and upper reaches of the channel, but less common in the mid-reaches of the channel (Conway *et al.* 2012), whereas the Nass Delta channel does not have out of channel bedforms in the upper reaches, but has extensive bedform fields in the mid-reaches indicating that flows remain channelized for longer and flow-stripping does not frequently occur

until the mid-reaches of the channel. The Toba Inlet submarine channel does have regular occurring bedforms in the mid-reaches of the channel (Conway *et al.* 2012), but the channel is not as long or well developed as the Nass Delta submarine channel.

Future Studies

A key research gap is linking flow type to deposits. Recent studies have produced more detailed measurements of the flow structure of turbidity currents (Heerema *et al.* 2020, Hill and Lintern 2022, Pope, Cartigny, *et al.* 2022, Baker, Talling, *et al.* 2024), but more study is needed to connect these flow types to specific deposit types and morphological change. Further studies in the Nass Delta submarine channel system could help address these gaps with the use of ADCP monitoring instruments installed above the channel. With care taken to position them out of the flow path of turbidity currents, moored ADCPs could monitor for flow structure of passing turbidity currents in and outside of the channel. For instance, how a flow under the travelling wave model interacts with knickpoints is not well understood (Heerema *et al.* 2020), so placing an ADCP at a knickpoint could help establish how flow structure changes as it passes over the knickpoint. A transect of moored ADCPs that included positions above and below the knickpoint could allow for the study of flow conditions during upwards migration and down-channel deposition. An ADCP placed to monitor flow conditions at an outer bend could reveal insight into the flow conditions that promote outer bend erosion versus flow stripping and overspill past the levee. ADCP placements along the channel would also provide insight into how frequently flows travel to different reaches of the channel. A measure of the exact timing of turbidity currents would also allow for investigating the specific river discharge and tidal conditions that may have triggered the turbidity current. A complete study of the submarine channel would integrate the deployment of ADCPs with an initial

MBES bathymetric survey, followed by a repeat MBES bathymetric survey and targeted coring during the ADCP retrieval to link flow conditions to bathymetric change and stratigraphic deposits.

Another research direction that could be explored is a study of organic carbon in the Nass Delta submarine channel system. Turbidity currents have been shown to play a role in the transport and burial of organic carbon making them an important component of the global carbon flux (Hage *et al.* 2020, 2022, Baker, Hage, *et al.* 2024). Previous studies have quantified the organic carbon flux of the Squamish and Bute Inlet fjords and found that turbidity current deposits contribute a significant component of organic carbon burial in these systems, which was resulting in underestimations of carbon burial in global studies (Hage *et al.* 2020, 2022). Woody debris and partially decomposed organic matter was observed in turbidite deposits in sediment cores in the Nass submarine channel system (Table 5; Figure 15). Therefore, the organic carbon component could be studied in this system to further constrain the burial rates of organic carbon from turbidity currents in fjords.

References

Adams, J., 1990. Paleoseismicity of the Cascadia subduction zone: Evidence from turbidites off the Oregon-Washington margin. *Tectonics*, 9 (4), 569–583.

Allin, J.R., Hunt, J.E., Talling, P.J., Clare, M.A., Pope, E., and Masson, D.G., 2016. Different frequencies and triggers of canyon filling and flushing events in Nazaré Canyon, offshore Portugal. *Marine Geology*, 371, 89–105.

Azpiroz-Zabala, M., Cartigny, M.J.B., Sumner, E.J., Clare, M.A., Talling, P.J., Parsons, D.R., and Cooper, C., 2017. A General Model for the Helical Structure of Geophysical Flows in Channel Bends. *Geophysical Research Letters*, 44 (23), 11,932-11,941.

Azpiroz-Zabala, M., Cartigny, M.J.B., Talling, P.J., Parsons, D.R., Sumner, E.J., Clare, M.A., Simmons, S.M., Cooper, C., and Pope, E.L., 2017. Newly recognized turbidity current structure can explain prolonged flushing of submarine canyons. *Science Advances*, 3 (10), e1700200.

Azpiroz-Zabala, M., Sumner, E., Cartigny, M., Peakall, J., Clare, M.A., Darby, S., Parsons, D., Dorrell, R., Özsoy, E., Tezcan, D., Wynn, R., and Johnson, J., 2024. Benthic biology influences sedimentation in submarine channel bends: Coupling of biology, sedimentation and flow. *The Depositional Record*, 10, 159–175.

Bagnold, R.A., 1962. Auto-Suspension of Transported Sediment; Turbidity Currents. *Proceedings of the Royal Society of London. Series A, Mathematical and physical sciences*, 265 (1322), 315–319.

Bailey, L.P., Clare, M.A., Pope, E.L., Haigh, I.D., Cartigny, M.J.B., Talling, P.J., Lintern, D.G., Hage, S., and Heijnen, M., 2023. Predicting turbidity current activity offshore from meltwater-fed river deltas. *Earth and Planetary Science Letters*, 604, 117977.

Bailey, L.P., Clare, M.A., Rosenberger, K.J., Cartigny, M.J., Talling, P.J., Paull, C.K., Gwiazda, R., Parsons, D.R., Simmons, S.M., and Xu, J., 2021. Preconditioning by sediment accumulation can produce powerful turbidity currents without major external triggers. *Earth and Planetary Science Letters*, 562, 116845.

Bailey, P., Wheaton, J., Reimer, M., and Brasington, J., 2022. Geomorphic Change Detection Software.

Baker, M., Talling, P., Burnett, R., Pope, E., Ruffell, S., Urlaub, M., Clare, M., Jenkins, J., Dietze, M., Neasham, J., Silva Jacinto, R., Hage, S., Hasenhündl, M., Simmons, S., Heerema, K., Heijnen, M., Kunath, P., Cartigny, M., McGhee, C., and Parsons, D., 2024. Seabed Seismographs Reveal Duration and Structure of Longest Runout Sediment Flows on Earth. *Geophysical Research Letters*, 51.

Baker, M.L., Hage, S., Talling, P.J., Acikalin, S., Hilton, R.G., Haghipour, N., Ruffell, S.C., Pope, E.L., Jacinto, R.S., Clare, M.A., and Sahin, S., 2024. Globally significant mass of terrestrial organic carbon efficiently transported by canyon-flushing turbidity currents. *Geology*, 52 (8), 631–636.

Blaise, B., Clague, J.J., and Mathewes, R.W., 1990. Time of maximum Late Wisconsin glaciation, west coast of Canada. *Quaternary Research*, 34 (3), 282–295.

Bornhold, B.D., Ren, P., and Prior, D.B., 1994. High-frequency turbidity currents in British Columbia fjords. *Geo-Marine Letters*, 14 (4), 238–243.

Bouma, A.H., 1962. *Sedimentology of Some Flysch Deposits: A Graphic Approach to Facies Interpretation*. Elsevier Publishing Company.

Bouma, A.H., 1964. Turbidites. *In*: A.H. Bouma and A. Brouwer, eds. *Developments in Sedimentology*. Elsevier, 247–256.

Bowen, A.J., Normark, W.R., and Piper, D.J.W., 1984. Modelling of turbidity currents on Navy Submarine Fan, California Continental Borderland. *Sedimentology*, 31 (2), 169–185.
Brasington, J., Langham, J., and Rumsby, B., 2003. Methodological sensitivity of morphometric estimates of coarse fluvial sediment transport. *Geomorphology*, 53 (3), 299–316.
Bricheno, L., Yeo, I., Clare, M., Hunt, J., Griffiths, A., Carter, L., Talling, P.J., Baker, M., Wilson, S., West, M., Panuve, S., and Fonua, S., 2024. The diversity, frequency and severity of natural hazard impacts on subsea telecommunications networks. *Earth-Science Reviews*, 259, 104972.
Bronk Ramsey, C., 2008. Deposition models for chronological records. *Quaternary Science Reviews*, 27 (1–2), 42–60.
Calder, B.R., 2003. Automatic statistical processing of multibeam echosounder data.
Canals, M., Puig, P., de Madron, X.D., Heussner, S., Palanques, A., and Fabres, J., 2006. Flushing submarine canyons. *Nature*, 444 (7117), 354–357.
Cartigny, M.J.B., Postma, G., van den Berg, J.H., and Mastbergen, D.R., 2011. A comparative study of sediment waves and cyclic steps based on geometries, internal structures and numerical modeling. *Marine Geology*, 280 (1), 40–56.
Cartigny, M.J.B., Ventra, D., Postma, G., and van Den Berg, J.H., 2014. Morphodynamics and sedimentary structures of bedforms under supercritical-flow conditions: New insights from flume experiments. *Sedimentology*, 61 (3), 712–748.
Chen, Y., Parsons, D.R., Simmons, S.M., Williams, R., Cartigny, M.J.B., Hughes Clarke, J.E., Stacey, C.D., Hage, S., Talling, P.J., Azpiroz-Zabala, M., Clare, M.A., Hizzett, J.L., Heijnen, M.S., Hunt, J.E., Lintern, D.G., Sumner, E.J., Vellinga, A.J., and Vendettuoli, D., 2021. Knickpoints and crescentic bedform interactions in submarine channels. *Sedimentology*, 68 (4), 1358–1377.
Clare, M.A., Clarke, J.H., Talling, P.J., Cartigny, M.J., and Pratomo, D., 2016. Preconditioning and triggering of offshore slope failures and turbidity currents revealed by most detailed monitoring yet at a fjord-head delta. *Earth and Planetary Science Letters*, 450, 208–220.
Conway, K.W., Barrie, J.V., Picard, K., and Bornhold, B.D., 2012. Submarine channel evolution: active channels in fjords, British Columbia, Canada. *Geo-Marine Letters*, 32 (4), 301–312.
Covault, J.A., Kostic, S., Paull, C.K., Sylvester, Z., and Fildani, A., 2017. Cyclic steps and related supercritical bedforms: Building blocks of deep-water depositional systems, western North America. *Marine Geology*, 393, 4–20.
Curray, J.R., Emmel, F.J., and Moore, D.G., 2002. The Bengal Fan: morphology, geometry, stratigraphy, history and processes. *Marine and Petroleum Geology*, 19 (10), 1191–1223.
De Leeuw, J., Eggenhuisen, J.T., and Cartigny, M.J.B., 2016. Morphodynamics of submarine channel inception revealed by new experimental approach. *Nature Communications*, 7 (1), 10886.
De Leeuw, J., Eggenhuisen, J.T., Spychala, Y.T., Heijnen, M.S., Pohl, F., and Cartigny, M.J.B., 2018. Sediment Volume and Grain-Size Partitioning Between Submarine Channel–Levee Systems and Lobes: An Experimental Study. *Journal of Sedimentary Research*, 88 (7), 777–794.
Dorrell, R.M., Darby, S.E., Peakall, J., Sumner, E.J., Parsons, D.R., and Wynn, R.B., 2013. Superelevation and overspill control secondary flow dynamics in submarine channels. *Journal of Geophysical Research: Oceans*, 118 (8), 3895–3915.
Dorrell, R.M., Peakall, J., Burns, C., and Keevil, G.M., 2018. A novel mixing mechanism in sinuous seafloor channels: Implications for submarine channel evolution. *Geomorphology*, 303, 1–12.
Fine, I.V., Rabinovich, A.B., Bornhold, B.D., Thomson, R.E., and Kulikov, E.A., 2005. The Grand Banks landslide-generated tsunami of November 18, 1929: preliminary analysis and numerical modeling. *Marine Geology*, 215 (1–2), 45–57.

Fissel, D.B., Lin, Y., Scoon, A., Lim, J., Brown, L., and Clouston, R., 2017. The variability of the sediment plume and ocean circulation features of the Nass River Estuary, British Columbia. *Satellite Oceanography and Meteorology*, 2 (2).

Gales, J.A., Talling, P.J., Cartigny, M.J.B., Hughes Clarke, J., Lintern, G., Stacey, C., and Clare, M.A., 2019. What controls submarine channel development and the morphology of deltas entering deep-water fjords? *Earth Surface Processes and Landforms*, 44 (2), 535–551.

Garcia, M. and Parker, G., 1989. Experiments on Hydraulic Jumps in Turbidity Currents Near a Canyon-Fan Transition. *Science*, 245 (4916), 393–396.

Gavey, R., Carter, L., Liu, J.T., Talling, P.J., Hsu, R., Pope, E., and Evans, G., 2017. Frequent sediment density flows during 2006 to 2015, triggered by competing seismic and weather events: Observations from subsea cable breaks off southern Taiwan. *Subaquatic paleoseismology: records of large Holocene earthquakes in marine and lacustrine sediments*, 384, 147–158.

Goldfinger, C., Nelson, C.H., Johnson, J.E., and Party, S.S., 2003. Holocene earthquake records from the Cascadia subduction zone and northern San Andreas fault based on precise dating of offshore turbidites. *Annual Review of Earth and Planetary Sciences*, 31 (1), 555–577.

Goldfinger, C., Nelson, C.H., Morey, A.E., Johnson, J.E., Patton, J.R., Karabanov, E.B., Gutierrez-Pastor, J., Eriksson, A.T., Gracia, E., Dunhill, G., Enkin, R.J., Dallimore, A., and Vallier, T., 2012. *Turbidite event history—Methods and implications for Holocene paleoseismicity of the Cascadia subduction zone*. US Geological Survey, No. 2330–7102.

Guiastrennec-Faugas, L., Gillet, H., Jacinto, R.S., Dennielou, B., Hanquiez, V., Schmidt, S., Simplet, L., and Rousset, A., 2020. Upstream migrating knickpoints and related sedimentary processes in a submarine canyon from a rare 20-year morphobathymetric time-lapse (Capbreton submarine canyon, Bay of Biscay, France). *Marine Geology*, 423, 106143.

Guiastrennec-Faugas, L., Gillet, H., Peakall, J., Dennielou, B., Gaillot, A., and Jacinto, R.S., 2021. Initiation and evolution of knickpoints and their role in cut-and-fill processes in active submarine channels. *Geology*, 49 (3), 314–319.

Hage, S., Cartigny, M.J.B., Clare, M.A., Sumner, E.J., Vendettuoli, D., Hughes Clarke, J.E., Hubbard, S.M., Talling, P.J., Lintern, D.G., Stacey, C.D., Englert, R.G., Vardy, M.E., Hunt, J.E., Yokokawa, M., Parsons, D.R., Hizzett, J.L., Azpiroz-Zabala, M., and Vellinga, A.J., 2018. How to recognize crescentic bedforms formed by supercritical turbidity currents in the geologic record: Insights from active submarine channels. *Geology*, 46 (6), 563–566.

Hage, S., Cartigny, M.J.B., Sumner, E.J., Clare, M.A., Hughes Clarke, J.E., Talling, P.J., Lintern, D.G., Simmons, S.M., Silva Jacinto, R., Vellinga, A.J., Allin, J.R., Azpiroz-Zabala, M., Gales, J.A., Hizzett, J.L., Hunt, J.E., Mozzato, A., Parsons, D.R., Pope, E.L., Stacey, C.D., Symons, W.O., Vardy, M.E., and Watts, C., 2019. Direct Monitoring Reveals Initiation of Turbidity Currents From Extremely Dilute River Plumes. *Geophysical Research Letters*, 46 (20), 11310–11320.

Hage, S., Galy, V.V., Cartigny, M.J.B., Acikalin, S., Clare, M.A., Gröcke, D.R., Hilton, R.G., Hunt, J.E., Lintern, D.G., McGhee, C.A., Parsons, D.R., Stacey, C.D., Sumner, E.J., and Talling, P.J., 2020. Efficient preservation of young terrestrial organic carbon in sandy turbidity-current deposits. *Geology*, 48 (9), 882–887.

Hage, S., Galy, V.V., Cartigny, M.J.B., Heerema, C., Heijnen, M.S., Acikalin, S., Clare, M.A., Giesbrecht, I., Gröcke, D.R., Hendry, A., Hilton, R.G., Hubbard, S.M., Hunt, J.E., Lintern, D.G., McGhee, C., Parsons, D.R., Pope, E.L., Stacey, C.D., Sumner, E.J., Tank, S., and Talling, P.J., 2022. Turbidity Currents Can Dictate Organic Carbon Fluxes Across River-Fed Fjords: An Example From Bute Inlet (BC, Canada). *Journal of Geophysical Research: Biogeosciences*, 127 (6), e2022JG006824.

Hamilton, P.B., Strom, K.B., and Hoyal, D.C.J.D., 2015. Hydraulic and sediment transport properties of autogenic avulsion cycles on submarine fans with supercritical distributaries. *Journal of Geophysical Research: Earth Surface*, 120 (7), 1369–1389.

Heerema, C.J., Cartigny, M.J.B., Jacinto, R.S., Simmons, S.M., Apprioual, R., and Talling, P.J., 2022. How distinctive are flood-triggered turbidity currents? *Journal of Sedimentary Research*, 92 (1), 1–11.

Heerema, C.J., Talling, P.J., Cartigny, M.J., Paull, C.K., Bailey, L., Simmons, S.M., Parsons, D.R., Clare, M.A., Gwiazda, R., Lundsten, E., Anderson, K., Maier, K.L., Xu, J.P., Sumner, E.J., Rosenberger, K., Gales, J., McGann, M., Carter, L., and Pope, E., 2020. What determines the downstream evolution of turbidity currents? *Earth and Planetary Science Letters*, 532, 116023.

Heijnen, M.S., Clare, M.A., Cartigny, M.J.B., Talling, P.J., Hage, S., Lintern, D.G., Stacey, C., Parsons, D.R., Simmons, S.M., Chen, Y., Sumner, E.J., Dix, J.K., and Hughes Clarke, J.E., 2020. Rapidly-migrating and internally-generated knickpoints can control submarine channel evolution. *Nature Communications*, 11 (1), 3129.

Heijnen, M.S., Clare, M.A., Cartigny, M.J.B., Talling, P.J., Hage, S., Pope, E.L., Bailey, L., Sumner, E., Lintern, D.G., Stacey, C., Parsons, D.R., Simmons, S.M., Chen, Y., Hubbard, S.M., Eggenhuisen, J.T., Kane, I., and Hughes Clarke, J.E., 2022. Fill, flush or shuffle: How is sediment carried through submarine channels to build lobes? *Earth and Planetary Science Letters*, 584, 117481.

Higgins, M.D., 2009. The Cascadia megathrust earthquake of 1700 may have rejuvenated an isolated basalt volcano in western Canada: Age and petrographic evidence. *Journal of Volcanology and Geothermal Research*, 179 (1–2), 149–156.

Hill, P.R. and Lintern, D.G., 2021. Sedimentary processes at the mouth of a tidally-influenced delta: New insights from submarine observatory measurements, Fraser Delta, Canada. *Sedimentology*, 68 (6), 2649–2670.

Hill, P.R. and Lintern, D.G., 2022. Turbidity currents on the open slope of the Fraser Delta. *Marine Geology*, 445, 106738.

Hizzett, J.L., Hughes Clarke, J.E., Sumner, E.J., Cartigny, M., Talling, P., and Clare, M., 2018. Which triggers produce the most erosive, frequent, and longest runout turbidity currents on deltas? *Geophysical Research Letters*, 45 (2), 855–863.

Hodgson, D.M., Peakall, J., and Maier, K.L., 2022. Submarine Channel Mouth Settings: Processes, Geomorphology, and Deposits. *Frontiers in Earth Science*, 10, 790320.

Hofstra, M., Hodgson, D., Peakall, J., and Flint, S., 2015. Giant scour-fills in ancient channel-lobe transition zones: formative processes and depositional architecture. *Sedimentary Geology*, 329, 98–114.

Hsu, S.-K., Kuo, J., Lo, C.-L., Tsai, C.-H., Doo, W.-B., Ku, C.-Y., and Sibuet, J.-C., 2008. Turbidity Currents, Submarine Landslides and the 2006 Pingtung Earthquake off SW Taiwan. *Terrestrial, Atmospheric and Oceanic Sciences*, 19 (6), 767.

Huang, H., Imran, J., and Pirmez, C., 2012. The depositional characteristics of turbidity currents in submarine sinuous channels. *Marine Geology*, 329–331, 93–102.

Hughes Clarke, J., 1994. Toward remote seafloor classification using the angular response of acoustic backscattering: a case study from multiple overlapping GLORIA data. *IEEE Journal of Oceanic Engineering*, 19 (1), 112–127.

Hughes Clarke, J.E., 2016. First wide-angle view of channelized turbidity currents links migrating cyclic steps to flow characteristics. *Nature Communications*, 7 (1), 11896.

Khripounoff, A., Crassous, P., Bue, N.L., Dennielou, B., and Jacinto, R.S., 2012. Different types of sediment gravity flows detected in the Var submarine canyon (northwestern Mediterranean Sea). *Progress in Oceanography*, 106, 138–153.

Khripounoff, A., Vangriesheim, A., Crassous, P., and Etoubleau, J., 2009. High frequency of sediment gravity flow events in the Var submarine canyon (Mediterranean Sea). *Marine Geology*, 263 (1), 1–6.

Kneller, B., 1995. Beyond the turbidite paradigm: physical models for deposition of turbidites and their implications for reservoir prediction. *Geological Society, London, Special Publications*, 94 (1), 31–49.

Kneller, B. and Buckee, C., 2000. The structure and fluid mechanics of turbidity currents: a review of some recent studies and their geological implications. *Sedimentology*, 47 (s1), 62–94.

Kolla, V., 2007. A review of sinuous channel avulsion patterns in some major deep-sea fans and factors controlling them. *Marine and Petroleum Geology*, 24 (6), 450–469.

Kostic, S. and Parker, G., 2006. The response of turbidity currents to a canyon–fan transition: internal hydraulic jumps and depositional signatures. *Journal of Hydraulic Research*, 44 (5), 631–653.

Kuenen, P.H. and Migliorini, C., 1950. Turbidity currents as a cause of graded bedding. *The Journal of Geology*, 58 (2), 91–127.

Labaume, P., Mutti, E., and Seguret, M., 1987. Megaturbidites: A depositional model from the eocene of the SW-Pyrenean Foreland basin, Spain. *Geo-Marine Letters*, 7 (2), 91–101.

Le Moigne, Y., Williams-Jones, G., Vigouroux, N., and Russell, J.K., 2022. Chronology and Eruption Dynamics of the Historic~1700 CE Eruption of Tseax Volcano, British Columbia, Canada. *Frontiers in Earth Science*, 10.

Lintern, D.G., Hill, P.R., and Stacey, C., 2016. Powerful unconfined turbidity current captured by cabled observatory on the Fraser River delta slope, British Columbia, Canada. *Sedimentology*, 63 (5), 1041–1064.

Lowe, D.R., 1982. Sediment Gravity Flows: II Depositional Models with Special Reference to the Deposits of High-Density Turbidity Currents. *SEPM Journal of Sedimentary Research*, Vol. 52.

Macdonald, H.A., Wynn, R.B., Huvenne, V.A.I., Peakall, J., Masson, D.G., Weaver, P.P.E., and McPhail, S.D., 2011. New insights into the morphology, fill, and remarkable longevity (>0.2 m.y.) of modern deep-water erosional scours along the northeast Atlantic margin. *Geosphere*, 7 (4), 845–867.

MacIntyre, D.G., Ash, C., and Britton, J., 1994. Skeena Arcview Data (NTS 93E,L,M; 94D, 104A,B, 103G,H,I,J,P).

Maier, K.L., Gales, J.A., Paull, C.K., Rosenberger, K., Talling, P.J., Simmons, S.M., Gwiazda, R., McGann, M., Cartigny, M.J.B., Lundsten, E., Anderson, K., Clare, M.A., Xu, J., Parsons, D., Barry, J.P., Wolfson-Schwehr, M., Nieminski, N.M., and Sumner, E.J., 2019. Linking Direct Measurements of Turbidity Currents to Submarine Canyon-Floor Deposits. *Frontiers in Earth Science*, 7, 144.

Masson, D.G., Huvenne, V.A.I., de Stigter, H.C., Arzola, R.G., and LeBas, T.P., 2011. Sedimentary processes in the middle Nazaré Canyon. *The Geology, Geochemistry, and Biology of Submarine Canyons West of Portugal*, 58 (23), 2369–2387.

Mcgee, D.T., Bilinski, P.W., Gary, P.S., Pfeiffer, D.S., and Sheiman, J.L., 1994. GEOLOGIC MODELS AND RESERVOIR GEOMETRIES OF AUGER FIELD, DEEPWATER GULF OF MEXICO. *In*: P. Weimer, A.H. Bouma, and B.F. Perkins, eds. *Submarine Fans and Turbidite Systems—Sequence Stratigraphy, Reservoir Architecture and Production Characteristics Gulf of Mexico and International*. SEPM Society for Sedimentary Geology, 0.

McKenna, G., Luternauer, J., and Kostaschuk, R., 1992. Large-scale mass-wasting events on the Fraser River delta front near Sand Heads, British Columbia. *Canadian Geotechnical Journal*, 29 (1), 151–156.
Middleton, G.V., 1966. Small-scale models of turbidity currents and the criterion for auto-suspension. *Journal of Sedimentary Research*, 36 (1), 202–208.
Milliman, J.D. and Syvitski, J.P.M., 1992. Geomorphic/Tectonic Control of Sediment Discharge to the Ocean: The Importance of Small Mountainous Rivers. *The Journal of geology*, 100 (5), 525–544.
Mosher, D.C., Moscardelli, L., Shipp, R.C., Chaytor, J.D., Baxter, C.D.P., Lee, H.J., and Urgeles, R., 2010. Submarine Mass Movements and Their Consequences. *In*: *Submarine Mass Movements and Their Consequences*. Springer Netherlands.
Mulder, T., Savoye, B., and Syvitski, J.P.M., 1997. Numerical modelling of a mid-sized gravity flow: the 1979 Nice turbidity current (dynamics, processes, sediment budget and seafloor impact). *Sedimentology*, 44 (2), 305–326.
Mulder, T., Syvitski, J.P., Migeon, S., Faugères, J.-C., and Savoye, B., 2003. Marine hyperpycnal flows: initiation, behavior and related deposits. A review. *Marine and Petroleum Geology*, 20 (6–8), 861–882.
Mulder, T. and Syvitski, J.P.M., 1995. Turbidity Currents Generated at River Mouths during Exceptional Discharges to the World Oceans. *The Journal of geology*, 103 (3), 285–299.
Mulder, T., Syvitski, J.P.M., and Skene, K.I., 1998. Modeling of erosion and deposition by turbidity currents generated at river mouths. *Journal of Sedimentary Research*, 68 (1), 124–137.
Nelson, J.L., 2008. Terrace Regional Mapping Project, Year 4: Extension of Paleozoic Volcanic Belt and Indicators of Volcanogenic Massive Sulphide–style Mineralization near Kitimat, British Columbia.
Normark, W.R., Piper, D., and Hess, G.R., 1979. Distributary channels, sand lobes, and mesotopography of Navy Submarine Fan, California Borderland, with applications to ancient fan sediments. *Sedimentology*, 26 (6), 749–774.
Obelcz, J., Xu, K., Georgiou, I.Y., Maloney, J., Bentley, S.J., and Miner, M.D., 2017. Sub-decadal submarine landslides are important drivers of deltaic sediment flux: Insights from the Mississippi River Delta Front. *Geology*, 45 (8), 703–706.
Pantin, H.M., 1979. Interaction between velocity and effective density in turbidity flow: Phase-plane analysis, with criteria for autosuspension. *Marine Geology*, 31 (1), 59–99.
Parker, G., 1982. Conditions for the ignition of catastrophically erosive turbidity currents. *Marine Geology*, 46 (3), 307–327.
Parker, G., Fukushima, Y., and Pantin, H.M., 1986. Self-accelerating turbidity currents. *Journal of Fluid Mechanics*, 171, 145–181.
Parsons, D.R., Peakall, J., Aksu, A.E., Flood, R.D., Hiscott, R.N., Beşiktepe, Ş., and Mouland, D., 2010. Gravity-driven flow in a submarine channel bend: Direct field evidence of helical flow reversal. *Geology*, 38 (12), 1063–1066.
Parsons, J.D., Bush, J.W.M., and Syvitski, J.P.M., 2001. Hyperpycnal plume formation from riverine outflows with small sediment concentrations. *Sedimentology*, 48 (2), 465–478.
Paull, C.K., Caress, D.W., Ussler, W., III, Lundsten, E., and Meiner-Johnson, M., 2011. High-resolution bathymetry of the axial channels within Monterey and Soquel submarine canyons, offshore central California. *Geosphere*, 7 (5), 1077–1101.
Paull, C.K., Mitts, P., Ussler, W., III, Keaten, R., and Greene, H.G., 2005. Trail of sand in upper Monterey Canyon: Offshore California. *GSA Bulletin*, 117 (9–10), 1134–1145.
Paull, C.K., Talling, P.J., Maier, K.L., Parsons, D., Xu, J., Caress, D.W., Gwiazda, R., Lundsten, E.M., Anderson, K., Barry, J.P., Chaffey, M., O'Reilly, T., Rosenberger, K.J., Gales, J.A., Kieft, B.,

McGann, M., Simmons, S.M., McCann, M., Sumner, E.J., Clare, M.A., and Cartigny, M.J., 2018. Powerful turbidity currents driven by dense basal layers. *Nature Communications*, 9 (1), 4114.

Paull, C.K., Ussler, W., Greene, H.G., Keaten, R., Mitts, P., and Barry, J., 2002. Caught in the act: the 20 December 2001 gravity flow event in Monterey Canyon. *Geo-Marine Letters*, 22 (4), 227–232.

Peakall, J., McCaffrey, B., and Kneller, B., 2000. A process model for the evolution, morphology, and architecture of sinuous submarine channels. *Journal of Sedimentary Research*, 70 (3), 434–448.

Peakall, J. and Sumner, E.J., 2015. Submarine channel flow processes and deposits: A process-product perspective. *Geomorphology*, 244, 95–120.

Pickard, G., 1961. Oceanographic features of inlets in the British Columbia mainland coast. *Journal of the Fisheries Board of Canada*, 18 (6), 907–999.

Picot, M., Droz, L., Marsset, T., Dennielou, B., and Bez, M., 2016. Controls on turbidite sedimentation: Insights from a quantitative approach of submarine channel and lobe architecture (Late Quaternary Congo Fan). *Marine and Petroleum Geology*, 72, 423–446.

Piper, D. and Normark, W.R., 1983. Turbidite depositional patterns and flow characteristics, Navy Submarine Fan, California Borderland. *Sedimentology*, 30 (5), 681–694.

Piper, D.J. and Savoye, B., 1993. Processes of late Quaternary turbidity current flow and deposition on the Var deep-sea fan, north-west Mediterranean Sea. *Sedimentology*, 40 (3), 557–582.

Piper, D.J.W. and Normark, W.R., 2001. Sandy Fans-From Amazon to Hueneme and Beyond. *AAPG Bulletin*, 85 (8), 1407–1438.

Piper, D.J.W. and Normark, W.R., 2009. Processes That Initiate Turbidity Currents and Their Influence on Turbidites: A Marine Geology Perspective. *Journal of Sedimentary Research*, 79 (6), 347–362.

Pohl, F., Eggenhuisen, J.T., Kane, I.A., and Clare, M.A., 2020. Transport and Burial of Microplastics in Deep-Marine Sediments by Turbidity Currents. *Environmental Science & Technology*, 54 (7), 4180–4189.

Pohl, F., Eggenhuisen, J.T., Tilston, M., and Cartigny, M.J.B., 2019. New flow relaxation mechanism explains scour fields at the end of submarine channels. *Nature Communications*, 10 (1), 4425.

Pope, E.L., Cartigny, M.J.B., Clare, M.A., Talling, P.J., Lintern, D.G., Vellinga, A., Hage, S., Açikalin, S., Bailey, L., Chapplow, N., Chen, Y., Eggenhuisen, J.T., Hendry, A., Heerema, C.J., Heijnen, M.S., Hubbard, S.M., Hunt, J.E., McGhee, C., Parsons, D.R., Simmons, S.M., Stacey, C.D., and Vendettuoli, D., 2022. First source-to-sink monitoring shows dense head controls sediment flux and runout in turbidity currents. *Science Advances*, 8 (20), eabj3220.

Pope, E.L., Heijnen, M.S., Talling, P.J., Jacinto, R.S., Gaillot, A., Baker, M.L., Hage, S., Hasenhündl, M., Heerema, C.J., McGhee, C., Ruffell, S.C., Simmons, S.M., Cartigny, M.J.B., Clare, M.A., Dennielou, B., Parsons, D.R., Peirce, C., and Urlaub, M., 2022. Carbon and sediment fluxes inhibited in the submarine Congo Canyon by landslide-damming. *Nature Geoscience*, 15 (10), 845–853.

Postma, G. and Cartigny, M.J.B., 2014. Supercritical and subcritical turbidity currents and their deposits--A synthesis. *Geology*, 42 (11), 987–990.

Prior, D.B., Bornhold, B.D., Wiseman, W.J., and Lowe, D.R., 1987. Turbidity Current Activity in a British Columbia Fjord. *Science*, 237 (4820), 1330–1333.

Ritchie, J.C. and McHenry, J.R., 1990. Application of radioactive fallout cesium-137 for measuring soil erosion and sediment accumulation rates and patterns: A review. *Journal of environmental quality*, 19 (2), 215–233.

Robbins, J.A., 1978. Geochemical and geophysical applications of radioactive lead. *In*: *Biogeochemistry of Lead in the Environment*. 285–393.

Ruffell, S.C., Talling, P.J., Baker, M.L., Pope, E.L., Heijnen, M.S., Jacinto, R.S., Cartigny, M.J.B., Simmons, S.M., Clare, M.A., Heerema, C.J., McGhee, C., Hage, S., Hasenhündl, M., and Parsons, D.R., 2024. Time-lapse surveys reveal patterns and processes of erosion by exceptionally powerful turbidity currents that flush submarine canyons: A case study of the Congo Canyon. *Geomorphology*, 463, 109350.

Schimel, A.C.G., Ierodiaconou, D., Hulands, L., and Kennedy, D.M., 2015. Accounting for uncertainty in volumes of seabed change measured with repeat multibeam sonar surveys. *Continental Shelf Research*, 111, 52–68.

Schmuck, N., Reuther, J., Baichtal, J.F., and Carlson, R.J., 2021. Quantifying marine reservoir effect variability along the Northwest Coast of North America. *Quaternary Research*, 103, 160–181.

Schumm, S.A., 1979. Geomorphic thresholds: the concept and its applications. *Transactions of the Institute of British Geographers*, 485–515.

Sequeiros, O.E., Naruse, H., Endo, N., Garcia, M.H., and Parker, G., 2009. Experimental study on self-accelerating turbidity currents. *Journal of Geophysical Research*, 114 (C5), n/a.

Shanmugam, G., 1997. The Bouma Sequence and the turbidite mind set. *Earth-Science Reviews*, 42 (4), 201–229.

Simmons, S.M., Azpiroz-Zabala, M., Cartigny, M.J.. B., Clare, M.A., Cooper, C., Parsons, D.R., Pope, E.L., Sumner, E.J., and Talling, P.J., 2020. Novel Acoustic Method Provides First Detailed Measurements of Sediment Concentration Structure Within Submarine Turbidity Currents. *Journal of Geophysical Research: Oceans*, 125 (5), e2019JC015904.

Slootman, A. and Cartigny, M.J.B., 2020. Cyclic steps: Review and aggradation-based classification. *Earth-Science Reviews*, 201, 102949.

Stacey, C.D., 2014. Frequency and initiation mechanisms of submarine slides on the Fraser Delta front. MSc Thesis. University of Victoria, Canada.

Stacey, C.D., Hill, P.R., Talling, P.J., Enkin, R.J., Hughes Clarke, J.E., and Lintern, D.G., 2019. How turbidity current frequency and character varies down a fjord-delta system: Combining direct monitoring, deposits and seismic data. *Sedimentology*, 66 (1), 1–31.

Stauffer, P.H., 1967. Grain-flow deposits and their implications, Santa Ynez Mountains, California. *Journal of Sedimentary Research*, 37 (2), 487–508.

Stevenson, C.J., Jackson, C.A.-L., Hodgson, D.M., Hubbard, S.M., and Eggenhuisen, J.T., 2015. Deep-Water Sediment Bypass. *Journal of Sedimentary Research*, 85 (9), 1058–1081.

de Stigter, H.C., Boer, W., de Jesus Mendes, P.A., Jesus, C.C., Thomsen, L., van den Bergh, G.D., and van Weering, T.C.E., 2007. Recent sediment transport and deposition in the Nazaré Canyon, Portuguese continental margin. *EUROSTRATAFORM: Role and functioning of Canyons*, 246 (2), 144–164.

Stow, D.A.V., Mayall, M., Stov, D.A.V., Mayall, M., Mayall, M., and Stov, D.A.V., 2000. Deep-water sedimentary systems; new models for the 21st century. *Marine and petroleum geology*, 17 (2), 125–342.

Symons, W.O., Sumner, E.J., Paull, C.K., Cartigny, M.J.B., Xu, J.P., Maier, K.L., Lorenson, T.D., and Talling, P.J., 2017. A new model for turbidity current behavior based on integration of flow monitoring and precision coring in a submarine canyon. *Geology*, 45 (4), 367–370.

Symons, W.O., Sumner, E.J., Talling, P.J., Cartigny, M.J.B., and Clare, M.A., 2016. Large-scale sediment waves and scours on the modern seafloor and their implications for the prevalence of supercritical flows. *Marine Geology*, 371, 130–148.

Syvitski, J.P., Morehead, M.D., Bahr, D.B., and Mulder, T., 2000. Estimating fluvial sediment transport: the rating parameters. *Water resources research*, 36 (9), 2747–2760.

Talling, Peter.J., Paull, C.K., and Piper, D.J.W., 2013. How are subaqueous sediment density flows triggered, what is their internal structure and how does it evolve? Direct observations from monitoring of active flows. *Earth-Science Reviews*, 125, 244–287.

Talling, P.J., 2001. On the frequency distribution of turbidite thickness. *Sedimentology*, 48 (6), 1297–1329.

Talling, P.J., 2014. On the triggers, resulting flow types and frequencies of subaqueous sediment density flows in different settings. *Marine Geology*, 352, 155–182.

Talling, P.J., Allin, J., Armitage, D.A., Arnott, R.W.C., Cartigny, M.J.B., Clare, M.A., Felletti, F., Covault, J.A., Girardclos, S., Hansen, E., Hill, P.R., Hiscott, R.N., Hogg, A.J., Clarke, J.H., Jobe, Z.R., Malgesini, G., Mozzato, A., Naruse, H., Parkinson, S., Peel, F.J., Piper, D.J.W., Pope, E., Postma, G., Rowley, P., Sguazzini, A., Stevenson, C.J., Sumner, E.J., Sylvester, Z., Watts, C., and Xu, J., 2015. Key Future Directions For Research On Turbidity Currents and Their Deposits. *Journal of Sedimentary Research*, 85 (2), 153–169.

Talling, P.J., Baker, M.L., Pope, E.L., Ruffell, S.C., Jacinto, R.S., Heijnen, M.S., Hage, S., Simmons, S.M., Hasenhündl, M., Heerema, C.J., McGhee, C., Apprioual, R., Ferrant, A., Cartigny, M.J.B., Parsons, D.R., Clare, M.A., Tshimanga, R.M., Trigg, M.A., Cula, C.A., Faria, R., Gaillot, A., Bola, G., Wallance, D., Griffiths, A., Nunny, R., Urlaub, M., Peirce, C., Burnett, R., Neasham, J., and Hilton, R.J., 2022. Longest sediment flows yet measured show how major rivers connect efficiently to deep sea. *Nature Communications*, 13 (1), 4193.

Talling, P.J., Cartigny, M.J.B., Pope, E., Baker, M., Clare, M.A., Heijnen, M., Hage, S., Parsons, D.R., Simmons, S.M., Paull, C.K., Gwiazda, R., Lintern, G., Hughes Clarke, J.E., Xu, J., Silva Jacinto, R., and Maier, K.L., 2023. Detailed monitoring reveals the nature of submarine turbidity currents. *Nature Reviews Earth & Environment*, 4 (9), 642–658.

Talling, P.J., Masson, D.G., Sumner, E.J., and Malgesini, G., 2012. Subaqueous sediment density flows: Depositional processes and deposit types. *Sedimentology*, 59 (7), 1937–2003.

Talling, P.J., Wynn, R.B., Masson, D.G., Frenz, M., Cronin, B.T., Schiebel, R., Akhmetzhanov, A.M., Dallmeier-Tiessen, S., Benetti, S., Weaver, P.P.E., Georgiopoulou, A., Zühlsdorff, C., and Amy, L.A., 2007. Onset of submarine debris flow deposition far from original giant landslide. *Nature*, 450 (7169), 541–544.

Toniolo, H. and Cantelli, A., 2007. Experiments on Upstream-Migrating Submarine Knickpoints. *Journal of Sedimentary Research*, 77 (9), 772–783.

Vendettuoli, D., Clare, M.A., Hughes Clarke, J.E., Vellinga, A., Hizzet, J., Hage, S., Cartigny, M.J.B., Talling, P.J., Waltham, D., Hubbard, S.M., Stacey, C., and Lintern, D.G., 2019. Daily bathymetric surveys document how stratigraphy is built and its extreme incompleteness in submarine channels. *Earth and Planetary Science Letters*, 515, 231–247.

Walker, R.G., 1976. Facies Models 2. Turbidites and associated coarse clastic deposits. *Geoscience Canada*, 3 (1), 25–36.

Wang, Z., Xu, J., Talling, P.J., Cartigny, M.J.B., Simmons, S.M., Gwiazda, R., Paull, C.K., Maier, K.L., and Parsons, D.R., 2020. Direct evidence of a high-concentration basal layer in a submarine turbidity current. *Deep Sea Research Part I: Oceanographic Research Papers*, 161, 103300.

Water Office: Government of Canada, 2023a. Daily Discharge for Nass River Above Shumal Creek (08DB001).

Water Office: Government of Canada, 2023b. Daily Discharge for Ansedagan Creek Near New Aiyansh (08DB013).

Weimer, P. and Link, M.H., 1991. Global Petroleum Occurrences in Submarine Fans and Turbidite Systems. *In*: P. Weimer and M.H. Link, eds. *Seismic Facies and Sedimentary Processes of Submarine Fans and Turbidite Systems*. New York, NY: Springer, 9–67.

Wells, M.G. and Dorrell, R.M., 2021. Turbulence Processes Within Turbidity Currents. *Annual Review of Fluid Mechanics*, 53 (1), 59–83.

Wheaton, J.M., Brasington, J., Darby, S.E., and Sear, D.A., 2010. Accounting for uncertainty in DEMs from repeat topographic surveys: improved sediment budgets. *Earth Surface Processes and Landforms*, 35 (2), 136–156.

Wilkin, J., Cuthbertson, A., Dawson, S., Stow, D., Stephen, K., Nicholson, U., and Penna, N., 2023. The response of high density turbidity currents and their deposits to an abrupt channel termination at a slope break: Implications for channel–lobe transition zones. *Sedimentology*, 70 (4), 1164–1194.

Xu, J.P., Barry, J.P., and Paull, C.K., 2013. Small-scale turbidity currents in a big submarine canyon. *Geology*, 41 (2), 143–146.

Xu, J.P., Sequeiros, O.E., and Noble, M.A., 2014. Sediment concentrations, flow conditions, and downstream evolution of two turbidity currents, Monterey Canyon, USA. *Deep Sea Research Part I: Oceanographic Research Papers*, 89, 11–34.

Zeng, J., Lowe, D.R., Prior, D.B., Wiseman, W.J., and Bornhold, B.D., 1991. Flow properties of turbidity currents in Bute Inlet, British Columbia. *Sedimentology*, 38 (6), 975–996.

Zulkifli, Z., Clare, M.A., Heijnen, M., Lintern, D., Stacey, C., Talling, P.J., Cartigny, M.J.B., Minshull, T.A., Moreno, H.M., Peakall, J., and Darby, S., 2024. A threshold in submarine channel curvature explains erosion rate and type. *Earth and Planetary Science Letters*, 646, 118953.

Appendices

Appendix A

Bathymetric Change Thresholding

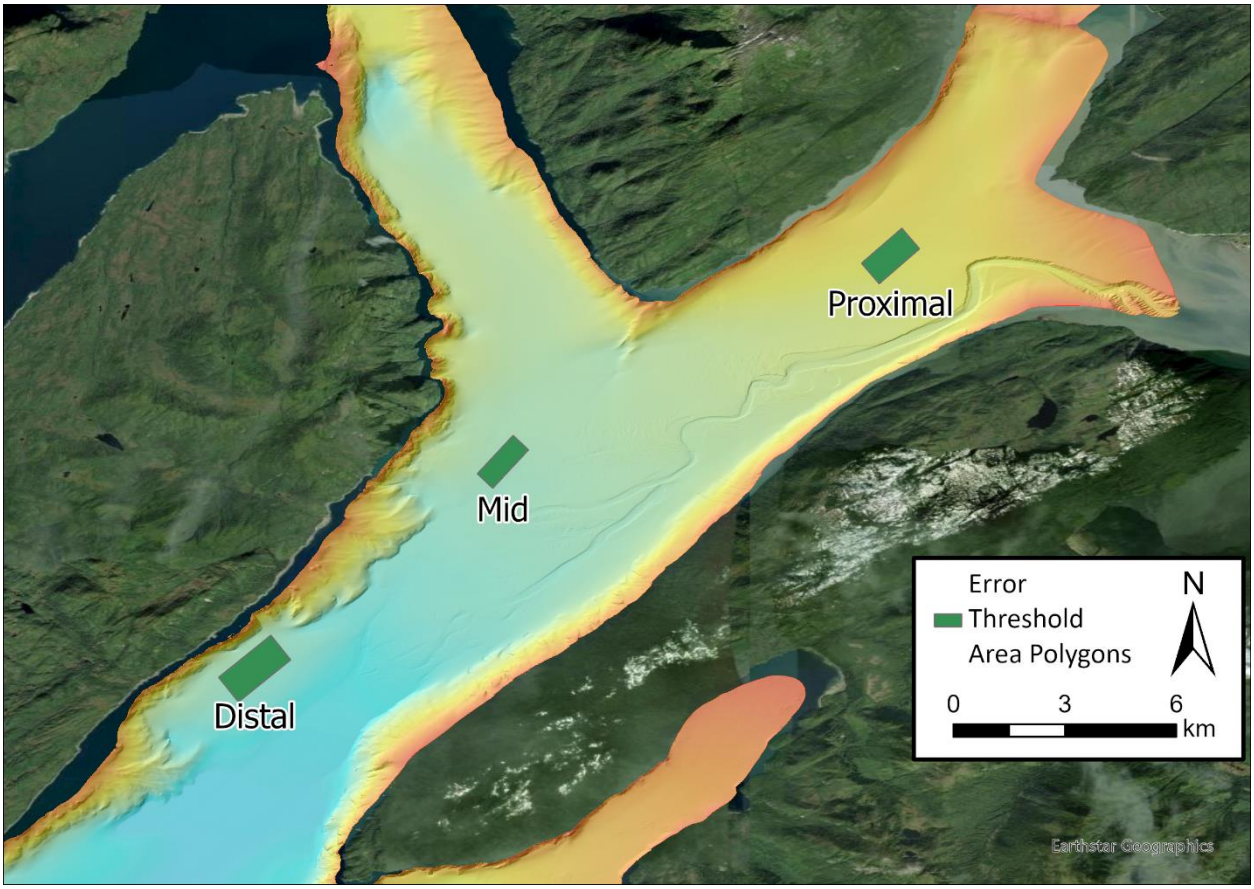

Figure 19: Location of the polygons where no change was expected beyond the background sedimentation. Bathymetric change was performed here, and the mean, median and standard deviation of the results were calculated (Table 9).

Table 9: Mean, median and Standard Deviation of the vertical bathymetric change within the test polygons where no bathymetric change would be expected beyond the background hemi-pelagic sedimentation. The highest value for each survey interval (median of distal polygon for 2020-2021 and median of proximal for 2021-2023) was chosen as the error threshold for bathymetric differencing. All these values were higher than the expected sedimentation rates of 3.31 cm/year, 1.67 cm/year and 1.13 cm/year in the proximal, mid and distal parts of the channel (Table 6).

Survey Interval	Location	Mean (m)	Median (m)	Standard Deviation (m)
2020-2021	Proximal	-0.29	-0.29	0.20
	Mid	0.21	0.22	0.26
	Distal	0.49	0.49	0.27
2021-2023	Proximal	0.55	0.55	0.20
	Mid	0.17	0.16	0.22
	Distal	0.24	0.24	0.25

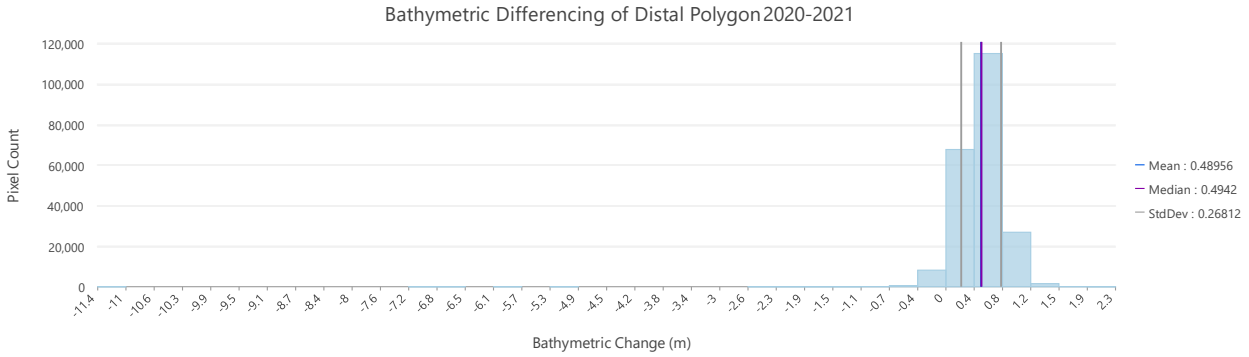

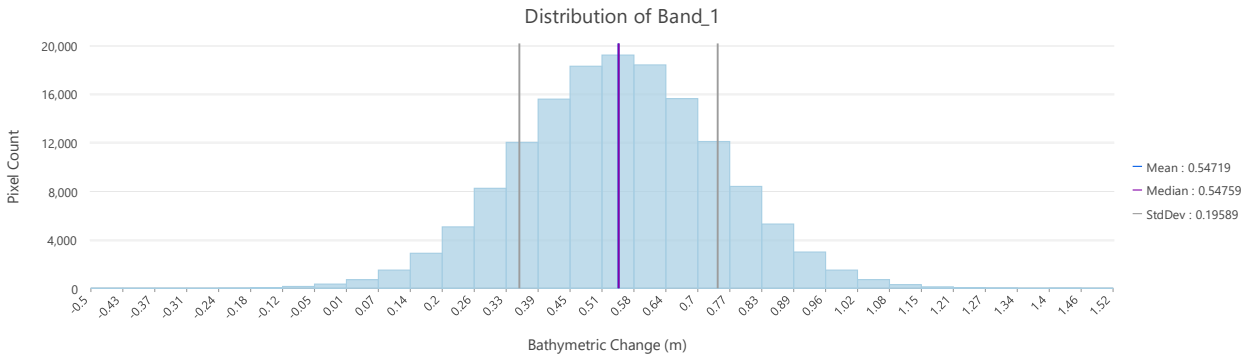

Figure 20: Example histograms of bathymetric change differencing results from the polygons where there was no expected change. These errors are approximately normally distributed and are clustered near zero (although they both skew positive). Each of the shown histograms had the highest median calculated change which was assumed to represent most of the error in the bathymetry and were thus used as the LOD threshold value.

Alternate Method for Thresholding

The second method uses the CUBE error surface, an uncertainty surface generated by the Combined Uncertainty and Bathymetry Estimator (CUBE) algorithm during the MBES processing for each of the surveys by CHS. This algorithm provides an estimate for both the lateral and vertical uncertainty within the MBES point cloud that is combined into one value for each raster cell (Calder 2003). Because of this combined approach, values range up to 3 m. The 2021 multibeam bathymetry survey showed the highest combined error of each of the surveys in the study region with a mean uncertainty of 0.93 m. Given that this survey is used in both differencing calculations, this value was chosen as the second minimum level of detection threshold. These two methods provide the range of estimations for real change with the latter representing a more conservative estimate and the former a less conservative estimate.

Bathymetric Change Volumetric Budget segregation

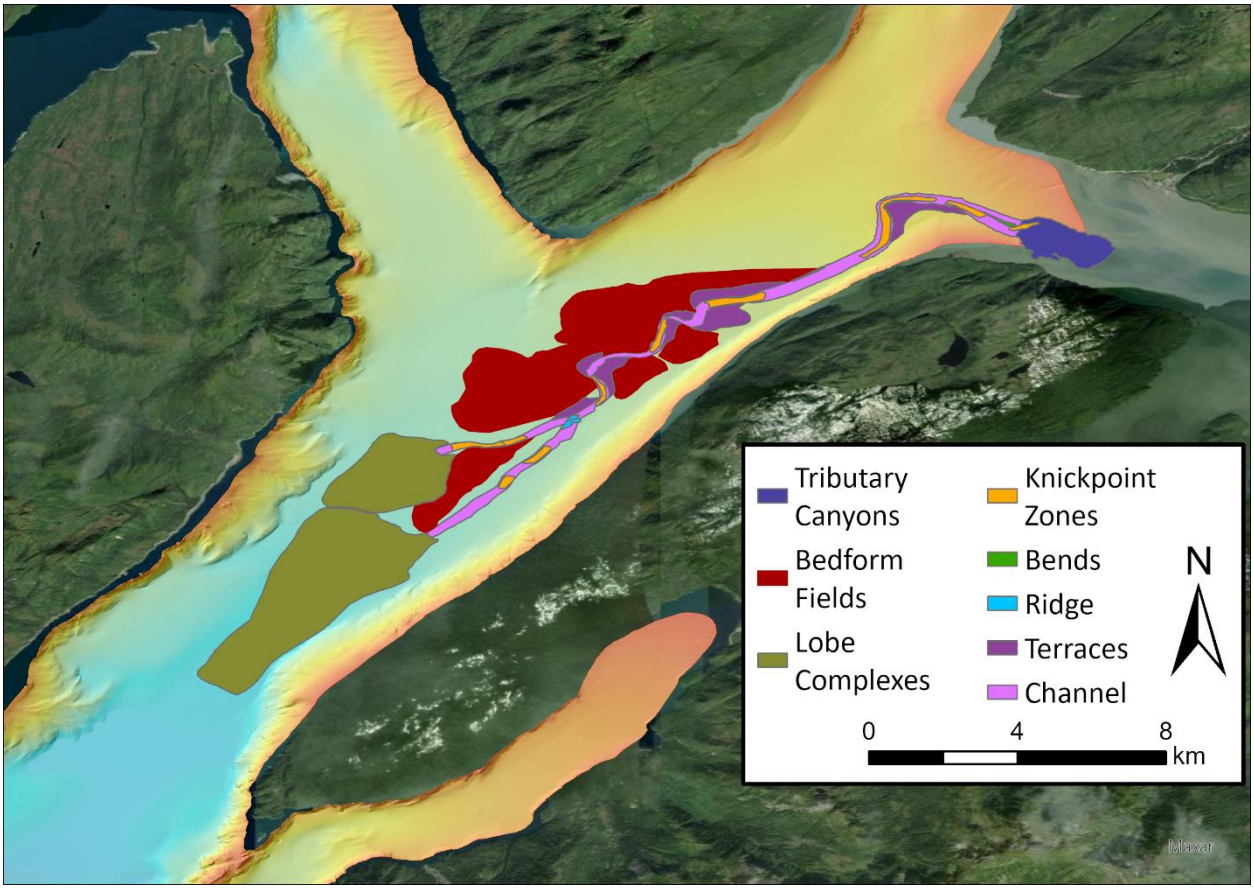

Figure 21: Polygons of the mapped submarine channel system features used for volumetric budget segregation in the GCD change detection software (Bailey et al. *2022).*

Appendix B

^{210}Pb, ^{226}Ra and ^{137}Cs Results

^{210}Pb results are presented in Table 10, Table 13, and Table 16 showing measured total ^{210}Pb activity and the excess ^{210}Pb activity. Plots of ^{210}Pb activities with core depth are included for both the inclusive and exclusive sedimentation rates. The inclusive rates include data points from all samples, whereas the exclusive rates have data points rejected from the top of the core where bioturbation and mixing result in excess noise (Stacey *et al.* 2019). Samples analysed for ^{226}Ra activities are included in Table 11, Table 14, and Table 17 which were used to estimate the background ^{210}Pb rate when background activity was not visible in the core samples. Samples analysed for ^{137}Cs activities are included in

Table 12, Table 15, Table 18 and plotted with core depth to identify the peak activity which was interpreted as the 1964 fallout peak from nuclear testing and used for comparison with the ^{210}Pb age-depth model (Ritchie and McHenry 1990).

Table 10: Measured ^{210}Pb activities, the excess ^{210}Pb, and the natural logarithm of the excess ^{210}Pb calculations for Core 13 shown against core depths and event-free depths.

Mid-depth (cm)	Event-Free Depth	Total ^{210}Pb (DPM/g)	Excess ^{210}Pb (DPM/g)	ln(excess ^{210}Pb)
0.00	0.00	13.82	13.021699	2.5666171
1.00	1.00	13.79	12.991342	2.5642832
2.00	2.00	14.05	13.250298	2.58402
3.00	3.00	13.49	12.686345	2.5405262
4.00	4.00	13.39	12.587457	2.5327008
5.00	5.00	12.79	11.994144	2.4844186
6.00	6.00	13.07	12.273925	2.5074771
7.00	7.00	14.10	13.302885	2.5879809
8.00	8.00	14.22	13.41884	2.5966597
9.00	9.00	12.41	11.614003	2.4522115
10.00	10.00	11.57	10.773515	2.3770908
12.00	12.00	10.89	10.086065	2.3111548
14.00	14.00	11.81	11.008266	2.3986465
16.00	16.00	12.91	12.106744	2.4937627
18.00	18.00	13.02	12.219606	2.5030417
25.00	25.00	9.83	9.0313609	2.2007031

30.00	30.00	10.00	9.1956611	2.2187318
35.00	35.00	9.31	8.5143455	2.1417524
40.00	40.00	5.94	5.1375986	1.6365858
45.00	45.00	5.72	4.9223058	1.5937771
50.00	50.00	4.64	3.836666	1.3446038
60.00	60.00	3.71	2.9125738	1.0690371
74.00	67.50	3.93	3.1281467	1.1404407
80.00	73.50	3.11	2.3068736	0.8358932
90.00	83.50	2.36	1.5599364	0.4446451

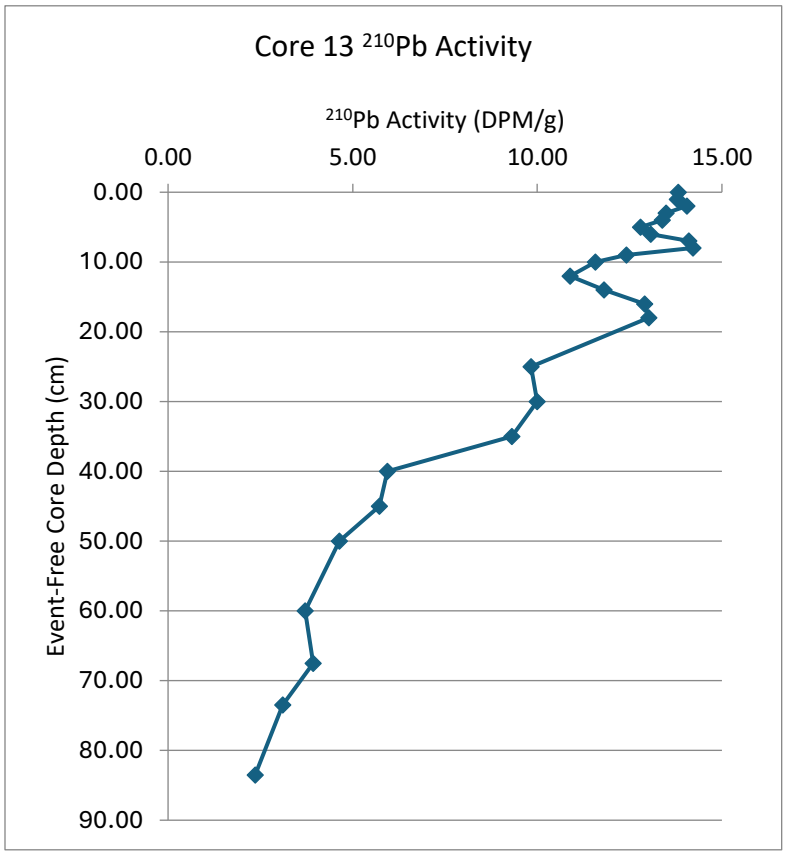

Figure 22: Plot of the measured ^{210}Pb activities in Core 13 with event-free core depth. Background ^{210}Pb activity was not reached.

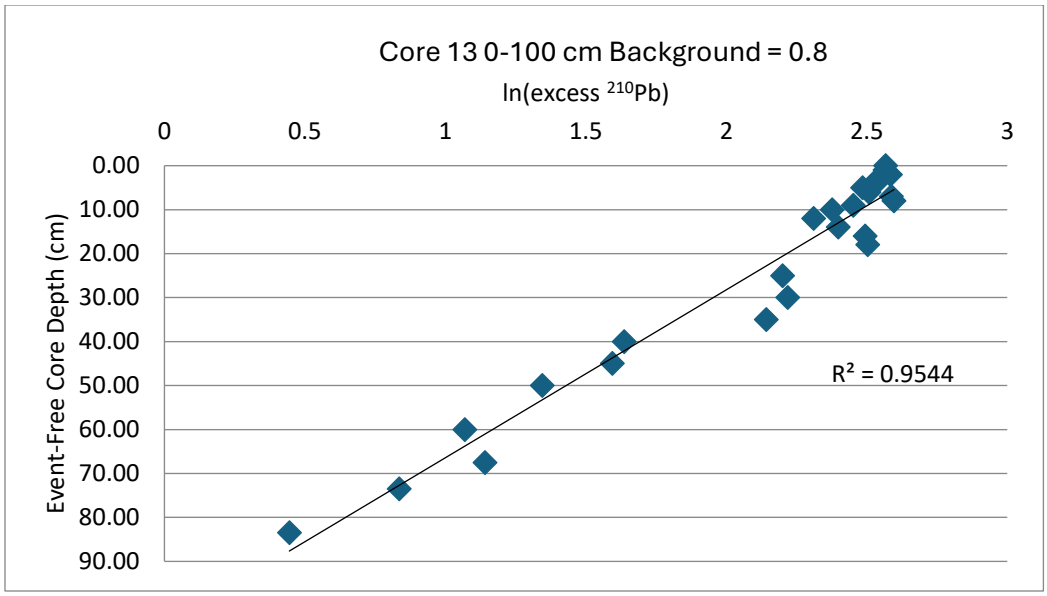

Figure 23: Plot of the natural logarithm of the excess ^{210}Pb with the event-free core depth of Core 13 for the inclusive model. Background activity of 0.80 DPM/g was estimated using the average of the measured ^{226}Ra activities (Table 11).

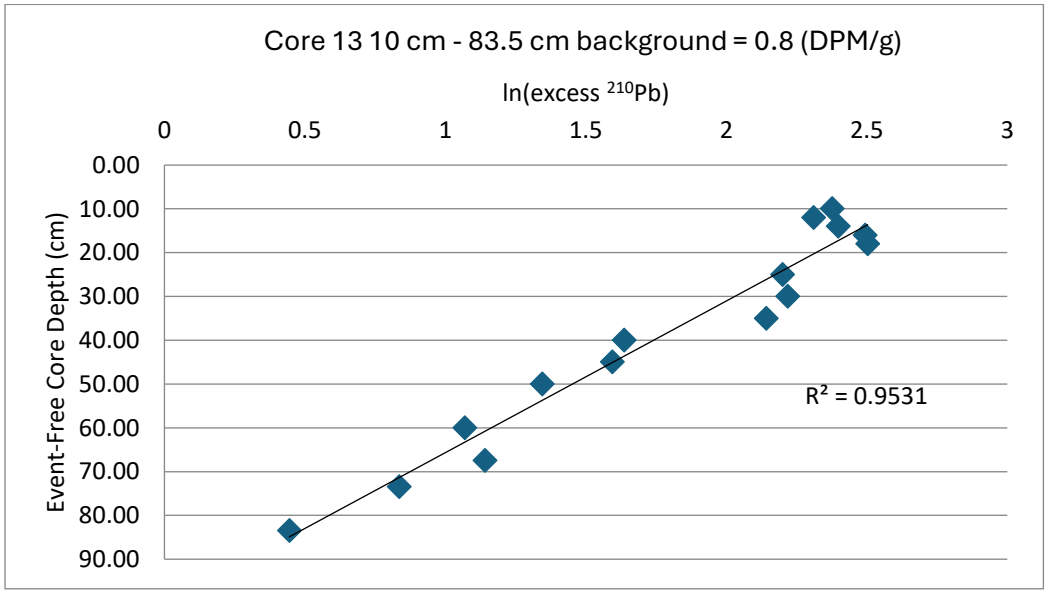

Figure 24: Plot of the natural logarithm of the excess ^{210}Pb with the event-free core depth of Core 13 for the exclusive model where samples from the top 10 cm of the core are excluded. Background activity of 0.80 DPM/g was estimated using the average of the measured ^{226}Ra activities (Table 11).

Table 11: Measured ^{226}Ra activities with core depth in Core 13. The average ^{226}Ra = 0.80 DPM/g.

Mid-Depth (cm)	Weight of Sample Counted (g) (less salt)	Count Time (sec)	^{226}Ra Activity (DPM/g Dry Wt.) (Salt Corrected)	Combined Error: 1 SD (DPM/g Dry Wt.)
11	1.508	60000	0.73	0.03
36	1.789	60000	0.84	0.02
91	1.506	60000	0.82	0.03

Table 12: Measured ^{137}Cs activities and error at the sampled core depth in Core 13.

Sample ID	Upper Depth (cm)	Lower Depth (cm)	Mid Depth (cm)	Event-Free Depth (cm)	^{137}Cs Activity on Counting Date (DPM/g dry wt.)	1 SD Counting Error (DPM/g dry wt.)
STN013 10-12 cm	10	12	11	11	0.28	0.11
STN013 35-37 cm	35	37	36	36	0.45	0.18
STN013 50-52 cm	50	52	51	51	0.54	0.09
STN013 52-54 cm	52	54	53	53	0.44	0.16
STN013 54-56 cm	54	56	55	55	0.60	0.10
STN013 56-58 cm	56	58	57	57	0.35	0.13
STN013 58-60 cm	58	60	59	59	0.74	0.16
STN013 60-62 cm	60	62	61	61	0.76	0.12
STN013 62-64 cm	62	64	63	63	0.61	0.11
STN013 64-66 cm	64	66	65	65	0.46	0.12
STN013 73-74 cm	73	74	73.5	67	0.07	0.41
STN013 74-76 cm	74	76	75	68.5	0.21	0.17
STN013 80-82 cm	80	82	81	74.5	0.15	0.09

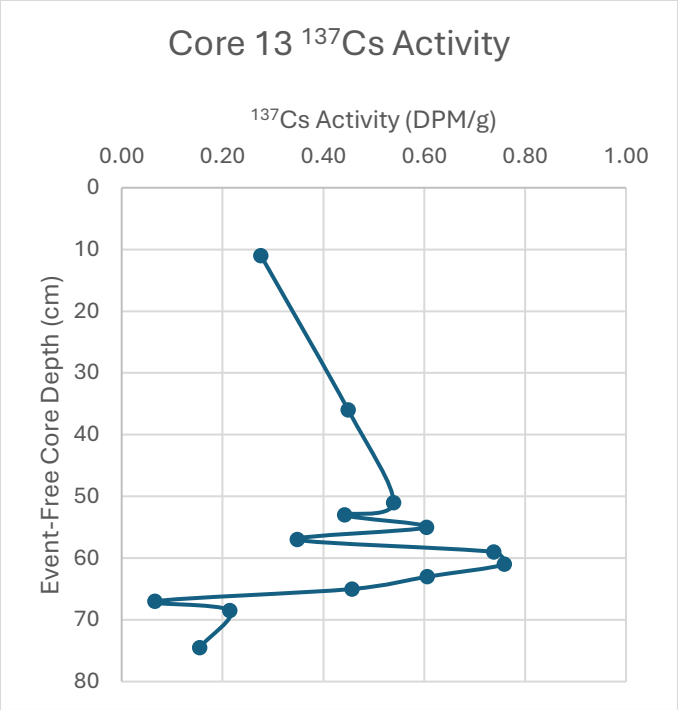

Figure 25: Measured ^{137}Cs activity plotted with corrected event-free core depth in Core 13. ^{137}Cs peak identified at 61 cm.

Core 6

Table 13: Measured ^{210}Pb activities, the excess ^{210}Pb, and the natural logarithm of the excess ^{210}Pb calculations for Core 6 shown against core depths and event-free depths. NA denotes where the natural logarithm of the excess ^{210}Pb has no real number solution.

Mid-depth (cm)	Event-Free Depth	Total ^{210}Pb (DPM/g)	Excess ^{210}Pb (DPM/g) Background = 0.81 (DPM/g)	ln(excess ^{210}Pb)	Excess ^{210}Pb (DPM/g) Background = 0.98 (DPM/g)	ln(excess ^{210}Pb)
18.00	9.00	3.33	2.521937	0.925027	2.351937062	0.85523927
32.00	18.00	3.34	2.53024	0.928314	2.360239928	0.858763278
45.00	28.00	2.34	1.533564	0.427594	1.363563765	0.310101688
58.00	41.00	1.94	1.128907	0.12125	0.958907436	-0.04196073
69.00	50.00	1.83	1.023265	0.022999	0.85326533	-0.158684725

94.00	60.00	1.34	0.525561	-0.64329	0.355561334	-1.034057514
105.00	71.00	1.67	0.859986	-0.15084	0.689986353	-0.37108346
116.00	82.00	1.46	0.64703	-0.43536	0.477029515	-0.740176915
124.00	90.00	1.43	0.621954	-0.47489	0.451953508	-0.794175962
185.00	121.50	0.95	0.142799	-1.94631	-0.027200537	NA
195.00	131.50	0.93	0.118535	-2.13255	-0.051464873	NA
209.00	141.00	0.90	0.092905	-2.37618	-0.07709498	NA
219.00	151.00	1.03	0.222372	-1.50341	0.052371569	-2.949391405
228.00	160.00	1.10	0.291049	-1.23426	0.121049288	-2.111557474
237.00	168.00	1.01	0.200223	-1.60832	0.030223483	-3.499136057
284.00	202.50	1.01	0.197032	-1.62439	0.027031829	-3.610740269
355.00	230.00	0.88	0.068823	-2.67622	-0.101177422	NA

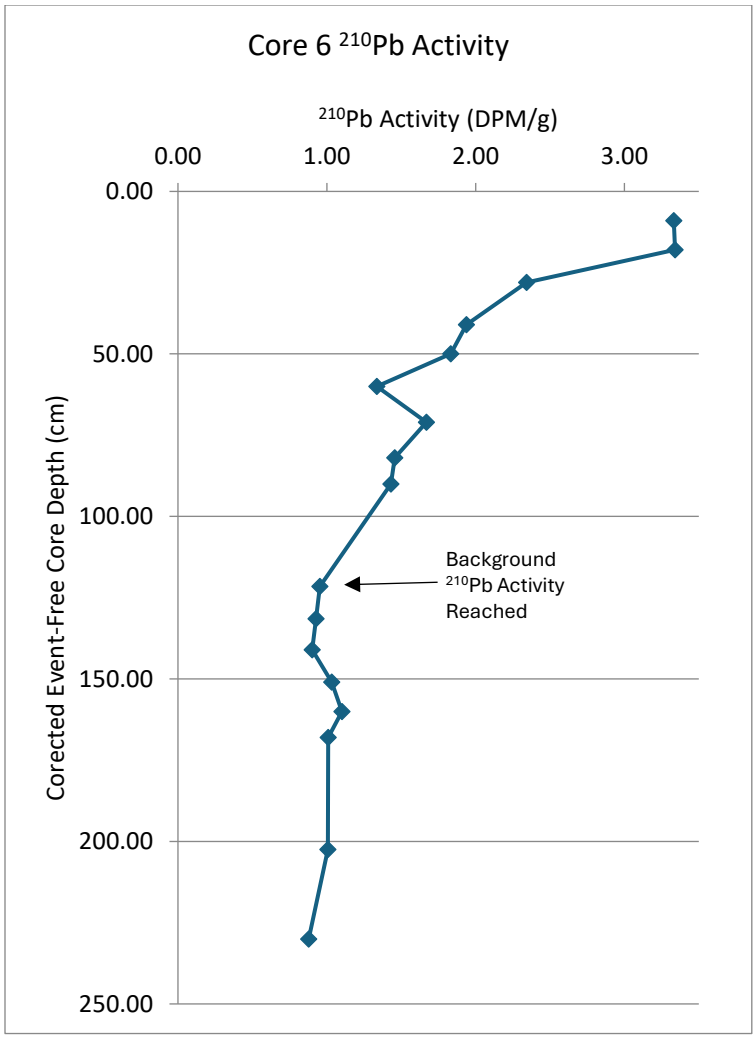

Figure 26: Plot of the measured ^{210}Pb activities in Core 6 with the corrected event-free core depth. Background ^{210}Pb activity was interpreted to be reached between the 90 cm and 121.5 cm measurements.

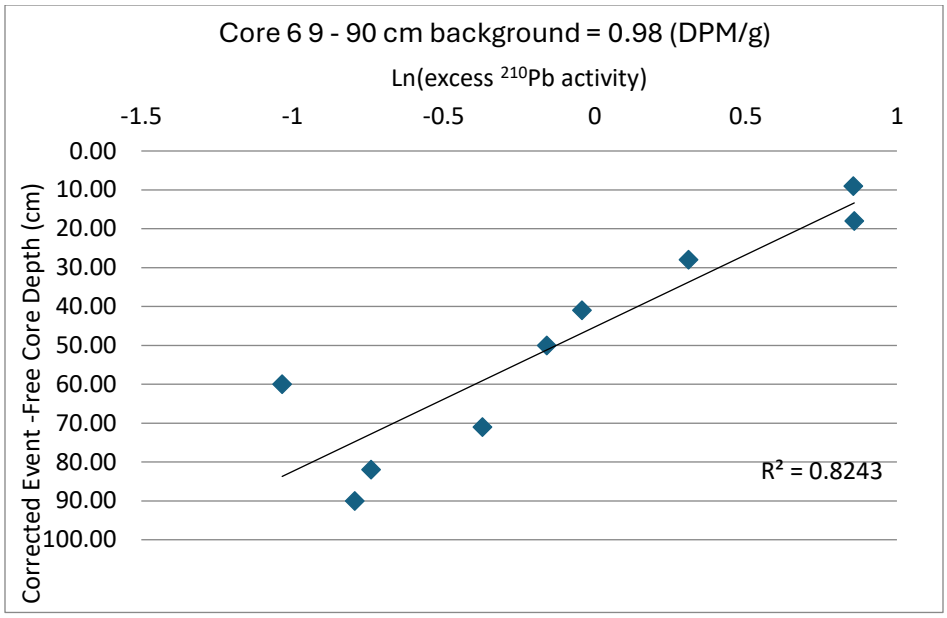

Figure 27: Plot of the natural logarithm of the excess ^{210}Pb with corrected event-free core depth of Core 6. Background of 0.98 DPM/g was calculated from the average of ^{210}Pb activities between 121.5 cm to 230 cm corrected event-free core depth where the curve was shown to flatten (Table 14).

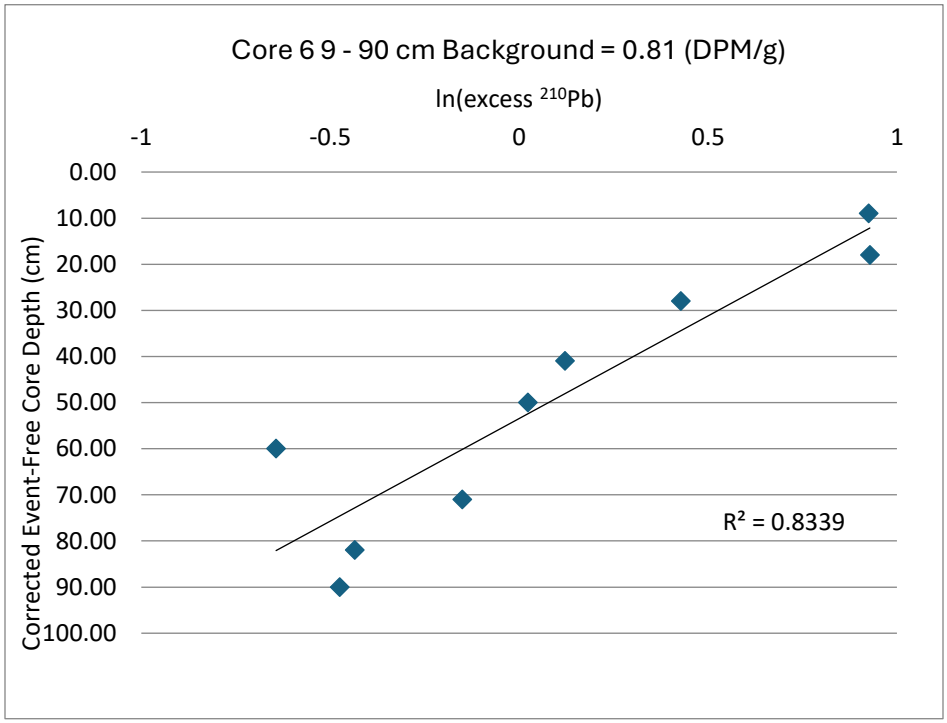

Figure 28: Plot of the natural logarithm of the excess ^{210}Pb with corrected event-free core depth of Core 6. Background of 0.81 DPM/g was calculated from the average of ^{226}Ra activities.

Table 14: Measured ^{226}Ra activities with core depth. The average ^{226}Ra = 0.81 DPM/g in Core 6.

Mid-Depth (cm)	Weight of Sample Counted (g) (less salt)	Count Time (sec)	^{226}Ra Activity (DPM/g Dry Wt.) (Salt Corrected)	Combined Error: 1 SD (DPM/g Dry Wt.)
32	1.515	60000	0.73	0.03
124	1.512	60000	0.83	0.03
355	1.503	60000	0.87	0.03

Table 15: Measured ^{137}Cs activities and error at the sampled core depth in Core 6.

Sample ID	Upper Depth (cm)	Lower Depth (cm)	Mid Depth	Event-Free Depth	137Cs Activity on Counting Date (DPM/g dry wt.)	1 SD Counting Error (DPM/g dry wt.)
006_57	57	59	58	41	0.26	0.06
006_68	68	70	69	50	0.32	0.05
006_93	93	95	94	60	0.45	0.06
006_104	104	106	105	71	0.60	0.07
006_115	115	117	116	82	0.43	0.03
006_123	123	125	124	90	0.17	0.05
006_184	184	186	185	121.5	-0.03	0.06

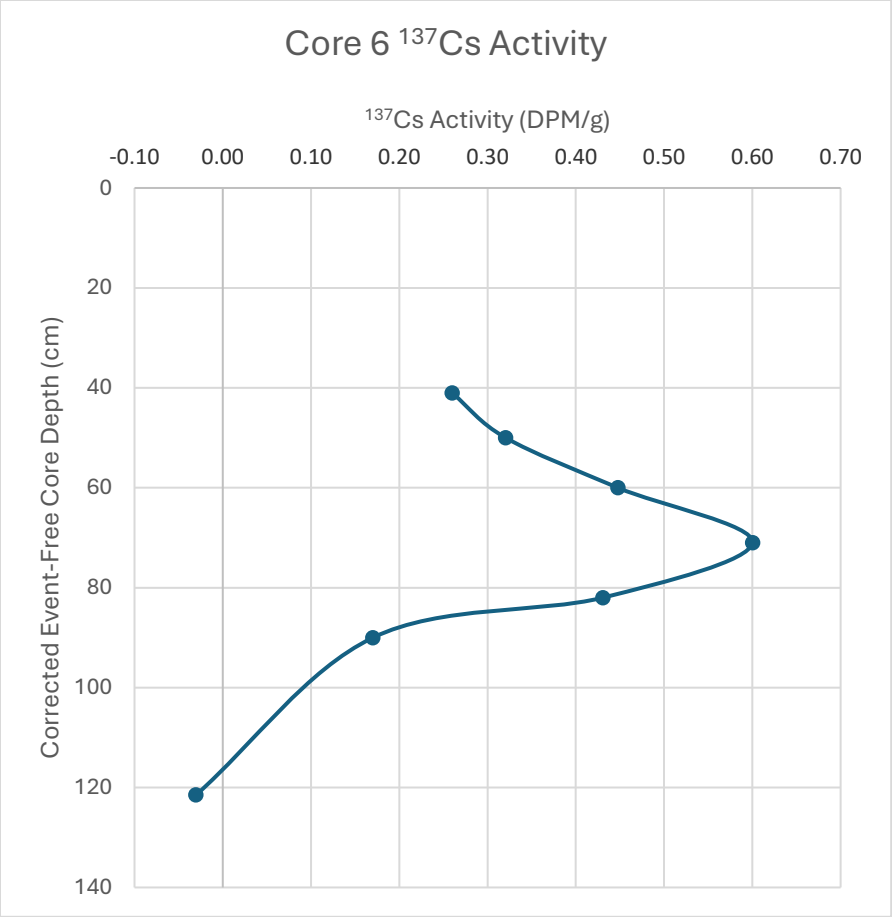

Figure 29: Measured ^{137}Cs activity plotted with corrected event-free core depth in Core 6. ^{137}Cs peak identified at 71 cm.

Core 39

Table 16: Measured ^{210}Pb activities, the excess ^{210}Pb, and the natural logarithm of the excess ^{210}Pb calculations for Core 13 shown against core depths.

Mid-depth (cm)	Total ^{210}Pb (DPM/g)	Excess ^{210}Pb (DPM/g)	ln(excess ^{210}Pb)
2.5	2.46	1.77	0.57098
5.5	2.21	1.52	0.41871
6.5	2.58	1.89	0.636577
7.5	2.58	1.89	0.636577

8.5	2.61	1.92	0.652325
9.5	2.88	2.19	0.783902
11	3.17	2.48	0.908259
13	3.06	2.37	0.86289
15	2.86	2.17	0.774727
17	2.86	2.17	0.774727
19	2.78	2.09	0.737164
26	2.42	1.73	0.548121
31	2.65	1.96	0.672944
36	2.4	1.71	0.536493
41	2.52	1.83	0.604316
46	2.07	1.38	0.322083
51	2.24	1.55	0.438255
61	2.08	1.39	0.329304
71	1.8	1.11	0.10436
81	2.2	1.51	0.41211
91	1.88	1.19	0.173953
101	1.51	0.82	-0.198451
111.00	1.69	1.00	0.000502
121.00	1.36	0.67	-0.404699
131.00	1.47	0.78	-0.243295
141.00	1.36	0.67	-0.403712
151.0	1.09	0.40	-0.913586

161.0	1.33	0.64	-0.438681
171.0	1.18	0.49	-0.704409
181.0	1.16	0.47	-0.748914
191.0	1.04	0.35	-1.062242
195.0	1.20	0.51	-0.66429

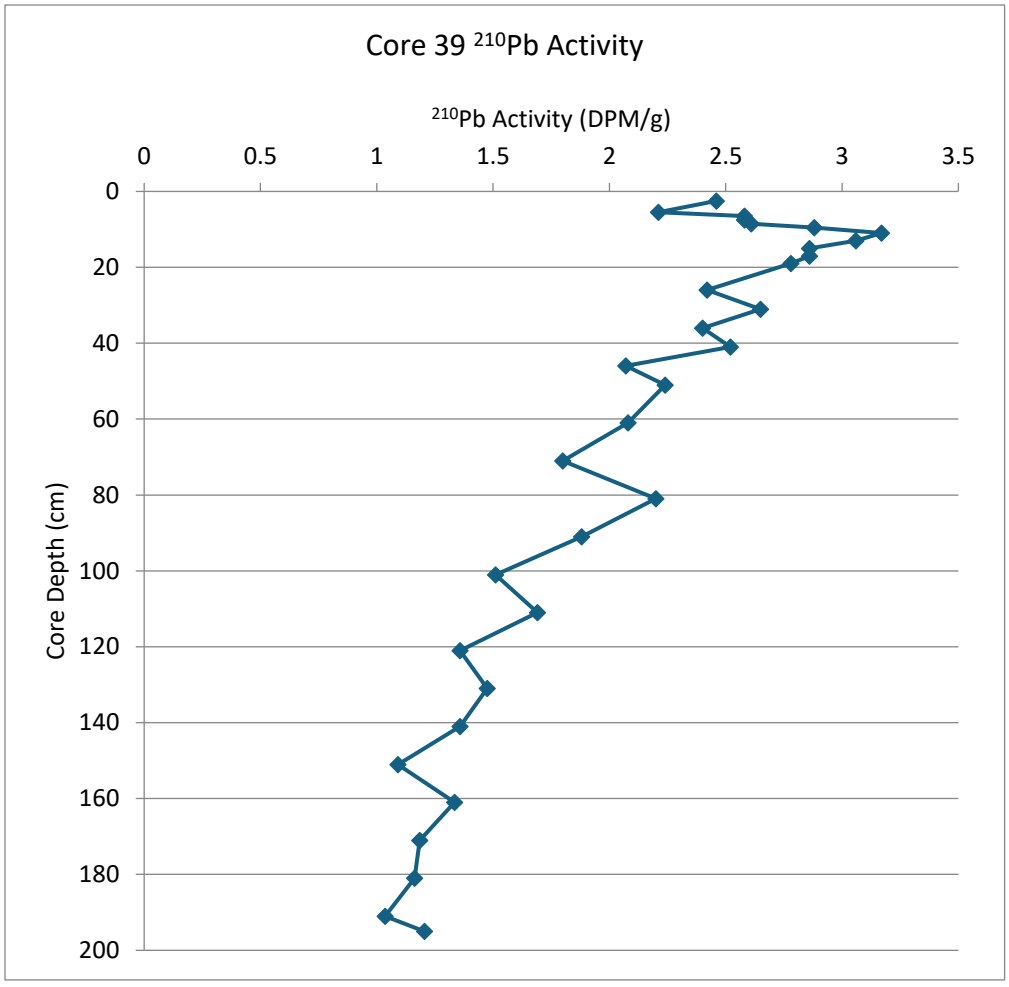

Figure 30: Plot of the measured ^{210}Pb activities in Core 39 with event-free core depth. Background ^{210}Pb activity was not reached.

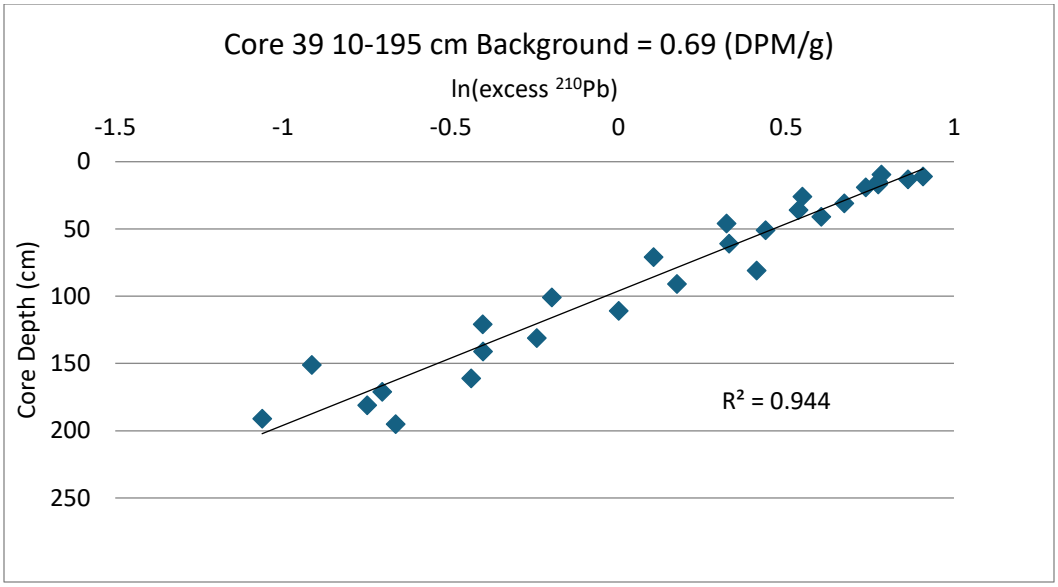

Figure 31: Plot of the natural logarithm of the excess ^{210}Pb with core depth of Core 39. An event-free depth was not able to be established for this core. Background of 0.69 DPM/g was calculated from the average of ^{226}Ra activities (Table 14).

Table 17: Measured ^{226}Ra activities with core depth in Core 39. The average ^{226}Ra = 0.72 DPM/g.

Mid-Depth (cm)	Weight of Sample Counted (g) (less salt)	Count Time (sec)	^{226}Ra Activity (DPM/g Dry Wt.) (Salt Corrected)	Combined Error: 1 SD (DPM/g Dry Wt.)
11	1.508	60000	0.69	0.02
36	1.789	60000	0.76	0.03
91	1.506	60000	0.71	0.02

Table 18: Measured ^{137}Cs activities and error at the sampled core depth in Core 39.

Sample ID	Upper Depth (cm)	Lower Depth (cm)	^{137}Cs Activity on Counting	1 SD Counting Error

			Date (DPM/g dry wt.)	(DPM/g dry wt.)
STN039 10-12 cm	10	12	0.37	0.10
STN039 35-37 cm	35	37	0.16	0.08
STN039 170-172 cm	170	172	0.25	0.08
STN039 180-182 cm	180	182	0.44	0.06
STN039 190-192 cm	190	192	0.58	0.10
STN039 192-194 cm	192	194	0.70	0.08
STN039 194-196 cm	194	196	0.64	0.06

Figure 32: Measured ^{137}Cs activity plotted with core depth in Core 39. ^{137}Cs peak identified at 193 cm.

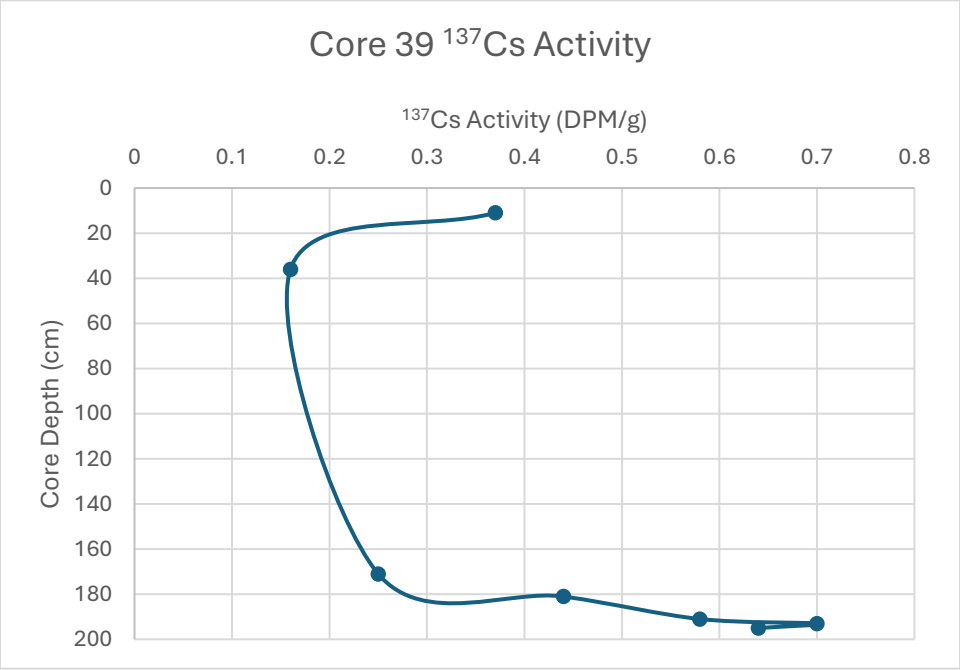

^{14}C Samples and Unmodeled Dates

Table 19: Samples collected for ^{14}C dating in Core 13 with the material type, the pre-treatment, the analysis lab, and the unmodeled ^{14}C date.

Core Depth Centre (cm)	Event Free Depth (cm)	Age (Year BP)	Error (Year)	Lab	MATERIAL / PRETREATMENT	Material Notes
244	211.5	180	±30	Beta	(plant material): acid/alkali/acid	Conifer needle and wood fragment AVERAGE
244	211.5	440	±30	Beta	(wood): acid/alkali/acid	Wood piece
367	319.5	480	±30	Beta	(wood): acid/alkali/acid	Wood piece
367	319.5	1270	±20	Keck		Shell fragment
510	446.5	1620	±15	Keck		Shell Fragment
596	525.5	835	±15	Keck		Plant fragments
788	706	1995	±15	Keck		Shell fragment
845.5	763.5	1200	±30	Beta	(wood): acid/alkali/acid	
878	792	2080	±30	Beta	(shell): sonicated in de-ionized water	Shell

Appendix C

Turbidite Density Estimation

The average density of turbidites was estimated to convert volumes of surficial change to sediment mass. Measurements of gamma density were taken for each interval of wet sediments that contained a turbidite bed in Core 6 to give a combined average density of the sediment and the seawater in the pore spaces, which, assuming there is no significant compaction post deposition, will be analogous to the density of deposition in situ. This resulted in a mean density of 2.15 g cm^3 with a standard deviation of 0.10 g cm^3. Core 6 was chosen as it contained frequent Facies 1 and Facies 2 turbidite beds to give the best representation of the density range of turbidite deposits. A similar analysis was performed on Core 13, giving a lower mean density of 1.82 g cm^3. However, the turbidites in this core are primarily Facie 2, and is in a much more distal setting of the channel system and would therefore be expected to skew to a smaller density value than most deposits from turbidity currents in the channel system.

Appendix D

Limitations of bathymetric change detection

Change detection using MBES bathymetry has challenges for quantifying volumetric change due to uncertainty created by the vertical resolution of the data. The use of Level-of-Detection blanking thresholds can limit the effects of uncertainty on volumetric calculations, but often results in very conservative estimates of volumetric change – especially with error propagation (Wheaton *et al.* 2010). This issue creates further complications when the processes that affect volumetric change

have different spatial trends, such as when an equivalent volume of erosion is concentrated to a small area that is well above the LOD threshold that is then deposited over a greater spatial area that may not vertically reach the LOD threshold creating an artificial in a net negative volumetric budget (Schimel *et al.* 2015). This created challenges in this study as the main depositional environments were where the energy of turbidity currents was no longer confined to the submarine channel which allowed a given volume of sediment to spread out over a larger area such as on the lobe (Heijnen *et al.* 2022), resulting in deposits that would be less likely to reach the threshold for detected volumetric change. Further evidence for this is shown in Core 6, which was taken from one of the meander-bend adjacent bedform fields, shows turbidite deposits with a maximum thickness of up to 30 cm (Figure 15). This is well below the LOD threshold, meaning that the largest deposits observed in sediment cores in this study would not be accounted for in volumetric change budgets. Therefore, the volumetric change estimates of deposition presented in this study should be taken to be underestimates of the true value of deposition.